UNIVERSITY OF CALIFORNIA, SAN DIEGO

Aspects of the three-dimensionality of the Southern Ocean overturning circulation

A dissertation submitted in partial satisfaction of the
requirements for the degree
Doctor of Philosophy

in

Oceanography

by

Veronica Tamsitt

Committee in charge:

Lynne D. Talley, Chair
Teresa K. Chereskin
Ian Eisenman
Sarah T. Gille
Matthew R. Mazloff
Eugene Pawlak

2018

The dissertation of Veronica Tamsitt is approved, and it is acceptable in quality and form for publication on microfilm and electronically:

_____

_____

_____

_____

_____

_____

Chair

University of California, San Diego

2018

TABLE OF CONTENTS

LIST OF FIGURES

LIST OF TABLES

LIST OF SUPPLEMENTAL VIDEOS

ACKNOWLEDGEMENTS

First of all, I would like to thank my advisor, Lynne Talley. Lynne's encyclopedic knowledge of oceanography, openness to new ideas, and willingness to ask questions are a constantly inspiring example of how to be a humble, curious scientist. Additionally, I thank Lynne for her endless support and encouragement in letting me do my PhD my way, whether that was spending a few weeks each summer teaching a high school science policy class, going to sea, traveling to international conferences or moving to San Francisco to complete the last portion of my PhD remotely. I never would have the diversity of experience and confidence as an independent researcher that I have now had it not been for the trust and support that Lynne gave me throughout my time at Scripps.

Second, I would like to thank my committee members. In particular, Matt Mazloff, who was an unofficial second advisor to me, and whom I thank for much of my understanding of ocean modeling and for his endless enthusiasm. Thanks to Sarah Gille for her attention to detail and phenomenal support of students, and I particularly thank her for her involvement in supervising our undergraduate intern, Sarah Ogle, for multiple summers at Scripps and in preparing the resulting publication. I thank Teri Chereskin, Ian Eisenman and Geno Pawlak for their feedback and encouragement.

I would also like to thank many collaborators and coauthors who have been the source of so many useful ideas and feedback. In particular, Ryan Abernathey, Ivana Cerovečki, Henri Drake, Simon Josey, Adele Morrison, and Jinbo Wang, have all been extremely knowledgeable, helpful and encouraging collaborators. To the SOCCOM Project team, including Joellen Russell, Jorge Sarmiento, Ken Johnson, Steve Riser and Roberta Hotinski, it has been wonderful to be a part of the SOCCOM community over the years and to have you all as cheerleaders along the way.

I thank Tomomi Ushii for her help and friendship over the past five years, and for making all my complicated travel plans happen. I would like to acknowledge the

Scripps graduate office staff for all their support and for putting so much effort into improving the student experience at SIO.

Special thanks to my SIO 2012 Climate/PO cohort for making classes and beyond so much fun. To my work mum and dad (and work step-mum and step-dad and step-cats), you are the best work family anyone could wish for and I am going to miss Nierenberg Hall 3rd floor very much. Thanks to my family, who may be far away geographically, but are always a skype call away and support me in all my endeavors. And finally thanks to my husband Dan: I wouldn't be here without you.

Chapter Two, in full, is a reprint of the material as it appears in the Journal of Climate, 2016. Tamsitt, V., L. D. Talley, M. R. Mazloff, and I. Cerovečki, (2016). Zonal variations in the Southern Ocean heat budget. *J. Climate*, 29(18), 6563-6579. ©American Meteorological Society. Used with permission. The dissertation author was the primary investigator and author of this paper.

Chapter Three, in full, is a reprint of the material as it appears in Nature Communications. Tamsitt, V., H. Drake, A. K. Morrison, L. D. Talley, C. O. Dufour, A. R. Gray, S. M. Griffies, M. R. Mazloff, J. L. Sarmiento, J. Wang, and W. Weijer (2017). Spiraling pathways of global deep waters to the surface of the Southern Ocean. *Nature Communications*, 8, 172. The dissertation/thesis author was the primary investigator and author of this paper.

Chapter Four, in full, is a reprint of the material as it appears in the Journal of Geophysical Research: Oceans. Tamsitt, V., R. P. Abernathey, M. R. Mazloff, J. Wang, and L. D. Talley (2018). Transformation of deep water masses along Lagrangian upwelling pathways in the Southern Ocean *J. Geophys. Res. Oceans*, in press. The dissertation/thesis author was the primary investigator and author of this paper.

Chapter Five is currently being prepared for submission for publication of the material by Tamsitt, V., L. D. Talley and M. R. Mazloff (2018), An Indian Deep Water Pathway South of Australia. The dissertation author was the primary investigator and author of this material.

VITA

2012	B. Sc. in Oceanography with Honors and minor in Mathematics, University of Washington
2018	Ph. D. in Oceanography, University of California, San Diego

PUBLICATIONS

Ogle S., V. Tamsitt, S. A. Josey, S. T. Gille , I. Cerovečki, L. D. Talley and R. A. Weller (2018). Extreme Southern Ocean heat loss and its mixed layer impacts revealed by the furthest south multi-year surface flux mooring. *in revision at Geophysical Research Letters*

Tamsitt, V., R. P. Abernathey, M. R. Mazloff, J. Wang, and L. D. Talley (2018). Transformation of deep water masses along Lagrangian upwelling pathways in the Southern Ocean *J. Geophys. Res. Oceans*, in press

Tamsitt, V., H. Drake, A. K. Morrison, L. D. Talley, C. O. Dufour, A. R. Gray, S. M. Griffies, M. R. Mazloff, J. L. Sarmiento, J. Wang, and W. Weijer (2017). Spiraling pathways of global deep waters to the surface of the Southern Ocean. *Nature Communications*, 8, 172

Alberty, M. S., S. Billheimer, M. M. Hamann, C. Y. Ou, V. Tamsitt, A. J. Lucas, M. H. Alford (2017). A reflecting, steepening, and breaking internal tide in a submarine canyon, *J. Geophys. Res. Oceans*, 122, 6872-6882, doi:10.1002/2016JC012583.

Tamsitt, V., L. D. Talley, M. R. Mazloff, and I. Cerovečki, (2016). Zonal variations in the Southern Ocean heat budget. *J. Climate*, 29(18), 6563-6579.

ABSTRACT OF THE DISSERTATION

Aspects of the three-dimensionality of the Southern Ocean overturning circulation

by

Veronica Tamsitt

Doctor of Philosophy in Oceanography

University of California, San Diego, 2018

Lynne D. Talley, Chair

The circulation of the Southern Ocean is unique due to the lack of meridional boundaries at the latitudes of Drake Passage. Westerly winds drive the Antarctic Circumpolar Current (ACC), linking the major ocean basins and facilitating inter-basin exchange of properties. Additionally, the steeply tilted isopycnals in the Southern Ocean allow interaction between the deep ocean and the atmosphere, and as a result the Southern Ocean has an outsized contribution to the global uptake and redistribution of heat, carbon and nutrients. Complex topography and eddies make this circulation fundamentally three-dimensional, but many features and associated mechanisms of this three-dimensional circulation are not well understood.

The objective of this thesis is to use the 1/6°, data-assimilating Southern Ocean State Estimate (SOSE), along with other high-resolution ocean models and available observations, to describe aspects of the three-dimensional structure of the upper cell of the Southern Ocean overturning circulation. First, we diagnose the upper ocean heat budget in the Southern Ocean (Chapter 2), and determine that a strong zonal asymmetry in the air-sea heat flux over the Southern Ocean is associated with large-scale meander the ACC mean path and associated asymmetry in geostrophic heat advection. Second, we use Lagrangian particle release experiments to show, for the first time, the full three-dimensional upwelling pathways of deep water from 30°S to the surface of the Southern Ocean (Chapter 3). We find that deep water moves south in narrow paths along the western and eastern boundaries of each ocean basin, then within the ACC upwelling is concentrated at hotspots associated with high eddy activity at major topographic features. Next, we quantify the water mass transformation along the upwelling pathways from Chapter 3, and find that although the upwelling in the ocean interior is largely along isopycnals, there is significant transformation just below the mixed layer and homogenization of deep water mass properties due to isopycnal mixing (Chapter 4). Finally, we highlight a newly identified poleward pathway of deep water along the eastern boundary of the Indian Ocean and describe the structure and variability of this pathway (Chapter 5).

Chapter 1

Introduction

The Southern Ocean is a key region for the global oceanic uptake and storage of heat, carbon and nutrients (Sarmiento et al., 2004; Frölicher et al., 2015). A zonally-averaged (two-dimensional) view of the Southern Ocean has proved very useful for understanding the leading-order dynamics of the overturning circulation (Marshall and Speer, 2012). However, the presence of topographic ridges and plateaus and the large-scale meridional excursions of the ACC along its circumpolar path mean that the circulation is fundamentally three-dimensional (e.g. Talley, 2013a; Thompson et al., 2016). Access to both higher-resolution ocean observations and eddy-permitting models and state estimates has opened a door to investigating the three-dimensional aspects of the circulation that are evident in observations in much greater detail (e.g. Sallée et al., 2010; Thompson and Sallee, 2012; Naveira Garabato et al., 2011; Talley, 2013a; Dufour et al., 2015; Thompson and Naveira Garabato, 2014; Mashayek et al., 2017). This thesis aims to explain some large-scale patterns of this three-dimensional circulation that are seen in observations by using state-of-the-art models, primarily the 1/6°resolution, data-assimilating Southern Ocean State Estimate (SOSE).

We first approach this overturning circulation from above in Chapter 2, with

an analysis of zonal variations in the Southern Ocean upper ocean heat budget. Prior work suggests that the primary heat budget balance in the Southern Ocean is between cooling by northward Ekman transport of cold Antarctic waters and ocean heat gain from air-sea flux (Dong et al., 2007). However, observations show a striking dipole pattern observed in air-sea heat fluxes over the Southern Ocean, with ocean heat gain in the Atlantic and Indian sectors of the ACC and ocean heat loss in the Pacific, suggesting a more complex heat budget (Large and Yeager, 2009). We diagnose the upper ocean heat budget in SOSE for the years 2005-2010, to determine what is balancing the air-sea heat flux along the ACC path. We show that while Ekman transport is an important cooling term, horizontal geostrophic advection is also an important term and is tied to the large scale meridional meander of the ACC. This result has important implications for the meridional overturning circulation, as it causes a distinct dipole in the buoyancy forcing that impacts the strength of the overturning (Radko and Marshall, 2006).

Another striking pattern seen in observations of hydrographic properties is the apparent spiraling of deep ocean properties southward and upward to the surface of the Southern Ocean. This suggests an important three-dimensional structure to this upwelling, which supplies carbon and nutrient-rich deep water to the sea surface. In Chapter 3, we discuss the release of Lagrangian particles in three eddying models to trace the three-dimensional upwelling pathways of deep water from the Atlantic, Indian and Pacific to the surface of the Southern Ocean. We find that deep water travels from 30°S to the ACC in narrow pathways along both the western and eastern boundaries of each basin. Once deep water reaches the ACC, upwelling in the interior is localized in hotspots at or downstream of major topographic features. This deep water eventually reaches the upper ocean in a broad region south of the ACC. We hypothesize that at the topographic hotspots, enhanced eddy kinetic energy drives particles southward and upward along tilted isopycnals. As particles travel from the deep basins to the sur-

face of the Southern Ocean, these southward and upward 'steps' at topographic features combine to give the effect of a spiral approaching the surface of the ocean around the Antarctic continent.

A key assumption in the conclusions of Chapter 3 is that the upwelling in the Southern Ocean interior is primarily along isopycnals. In Chapter 4 we examine the validity of this assumption by looking at water mass transformation along Lagrangian upwelling pathways in SOSE. We track the density along particle pathways and use this to look at distributions of the cumulative water mass transformation at different stages during upwelling. We show that while upwelling is largely along isopycnals in the ocean interior, there is substantial transformation toward lighter density classes below the mixed layer as a result of mixing with fresher Antarctic surface waters. We also look at temperature and salinity changes to show that significant along-isopycnal mixing leads to homogenization of deep water mass properties, and we compare the Lagrangian results to Eulerian water mass transformation calculated in SOSE.

Finally, in Chapter 5, we delve deeper into describing a pathway of deep water from the eastern Indian Ocean to the ACC along the southern coast of Australia. This pathway, identified in Chapter 3, has not previously been described in detail, owing to both a lack of observations of the deep ocean in this region and a lack of recognition of the importance of this pathway for carrying carbon-rich Indian Deep Water to the ACC. We combine Lagrangian pathway results and SOSE model fields with existing hydrographic observations and a Deep Argo float trajectory to confirm the existence of a deep poleward, boundary flow along that carries 14.2 Sv of deep water between 1500 m and 3000 m depth from 30°S along the southern coast of Australia to the ACC. Observations support the hypothesis that this pathway carries low-oxygen, high-nutrient, high-carbon Indian Deep Water to the Southern Ocean. We describe the structure and properties of this pathway, characterize the transport and variability of the flow and hypothesize about

the dynamics of the pathway.

Chapter 2

Zonal variations in the Southern Ocean heat budget

Abstract

The spatial structure of the upper ocean heat budget in the Antarctic Circumpolar Current (ACC) is investigated using the 1/6°, data-assimilating Southern Ocean State Estimate (SOSE) for 2005-2010. The ACC circumpolar integrated budget shows 0.27 PW of ocean heat gain from the atmosphere and 0.38 PW heat gain from divergence of geostrophic heat transport are balanced by -0.58 PW cooling by divergence of Ekman heat transport and -0.09 PW divergence of vertical heat transport. However, this circumpolar integrated balance obscures important zonal variations in the heat budget. Air-sea heat flux show a zonally asymmetric pattern of ocean heat gain in the Indian and Atlantic sectors and ocean heat loss in the Pacific sector of the ACC. In the Atlantic and Indian sectors of the ACC, the surface ocean heat gain is primarily balanced by divergence of equatorward Ekman heat transport that cools the upper ocean. In the Pacific sector, surface ocean heat loss and cooling due to divergence of Ekman heat transport are balanced by warming due to divergence of geostrophic heat advection, which is sim-

ilar to the dominant heat balance in the subtropical Agulhas Return Current. Divergence of horizontal and vertical eddy advection of heat are important for warming the upper ocean close to major topographic features, while the divergence of mean vertical heat advection is a weak cooling term. Our results show that topographic steering and zonal asymmetry in air-sea exchange lead to substantial zonal asymmetries in the heat budget, which is important for understanding the upper cell of the overturning circulation.

2.1 Introduction

The Southern Ocean component of the global meridional overturning circulation is fundamentally important to climate through air-sea exchange and redistribution of heat, freshwater, carbon and nutrients (e.g. Sarmiento et al., 2004; Ito et al., 2010). Westerly winds drive the eastward flowing Antarctic Circumpolar Current (ACC), linking the major ocean basins and allowing inter-basin exchange of properties. The circumpolar nature of the Southern Ocean and predominately zonal flow of the ACC have led to frequent use of zonally-averaged theories to describe the Southern Ocean overturning circulation. Residual-mean theories explain the circumpolar-mean overturning circulation as a balance between the northward Eulerian transport driven by wind forcing and an opposing southward eddy-driven transport (e.g. Karsten and Marshall, 2002; Marshall and Radko, 2003). However, a zonally averaged view of the Southern Ocean is limited because interaction of the flow with topography and asymmetries in air-sea exchange lead to zonal asymmetries in Southern Ocean dynamics and properties, including zonal geostrophic heat transport (Sun and Watts, 2002), eddy kinetic energy (Chelton et al., 1990), response of the mixed layer depth to wind variability (Sallée et al., 2010) and cross-front particle exchange (Thompson and Sallee, 2012).

The isopycnals in the ACC are steeply tilted upward toward Antarctica and out-

crop at the surface allowing upwelling of deep, dense water, which influences air-sea exchange. Surface buoyancy gain over the Southern Ocean is necessary to convert these upwelled water masses to lighter water masses at the surface and is important for setting the strength of the upper cell of the meridional overturning circulation (Radko and Marshall, 2006; Morrison et al., 2011). Freshwater flux dominates the total surface buoyancy flux poleward of the ACC, heat flux dominates equatorward of the ACC, while in the ACC latitude range both heat flux and freshwater flux contribute to buoyancy flux (Speer et al., 2000; Iudicone et al., 2008b; Cerovečki et al., 2013). Air-sea heat flux shows large spatial inhomogeneity in the ACC and as a result, heat fluxes are a major contribution to the impact of buoyancy fluxes on the overturning circulation in the ACC. However, our knowledge about air-sea fluxes has been severely limited due to a lack of direct observations (Bourassa et al., 2013) and air-sea heat fluxes have been identified as the largest contributor to uncertainty in the upper ocean heat budget (Dong et al., 2007; Faure et al., 2011).

Recently developed air-sea flux products that constrain the heat fluxes with additional observations and reduce the global long-term surface heat imbalance (Large and Yeager, 2009) as well as adjusted fluxes from state estimates constrained to observations (Fig. 2.1a,b) show agreement in large-scale patterns of air-sea heat fluxes in the Southern Ocean (Cerovečki et al., 2011). These improved heat flux products reveal a robust, large-scale zonally asymmetric pattern in the ACC of broad ocean heat gain in the Indian and Atlantic basins and a broad region of ocean cooling in the Pacific basin (Fig. 2.1b). The impact of this zonal dipole on the overturning circulation has been explored in an idealized model (Radko and Marshall, 2006), showing a stronger residual overturning circulation in the region of larger buoyancy gain due to stronger ocean heat gain in the Indian and Atlantic sectors. From in situ ocean observations, Sun and Watts (2002) show that the ACC warms where it flows equatorward in the Atlantic and Indian

sectors, and cools where it flows poleward in the Pacific sector. The zonal dipole air-sea heat flux pattern in Fig. 2.1 matches their inference of warming and cooling, although the SOSE and Large and Yeager (2009) heat flux pattern is zonally much broader than that proposed by Sun and Watts (2002).

Dong et al. (2007) used observations and a simple model to estimate the mixed layer heat budget in the Southern Ocean from 40°S to 60°S and inferred that in the domain-average and in each basin the dominant mixed layer balance is between air-sea heat gain and cooling by divergence of meridional Ekman advection of temperature, and that divergence of geostrophic advection of temperature plays a minimal role. This balance between air-sea heat fluxes and divergence of Ekman heat advection differs significantly from western boundary current regions, where poleward geostrophic advection of warm subtropical water is important in balancing ocean heat loss to the atmosphere in the mixed layer (Vivier et al., 2002; Dong and Kelly, 2004; Roemmich et al., 2005). Quasi-northward Ekman transport has been identified as the dominant cooling mechanism in the ACC upper ocean and is important for Subantarctic Mode Water formation (Sloyan and Rintoul, 2001a; Rintoul and England, 2002; Sallée et al., 2006, 2008). Recent work has suggested significant differences in the mixed layer heat balance in different zones north, south and within the ACC fronts (Sallée et al., 2008; Faure et al., 2011), and shown that regional heat balances depart from the zero-order balance between air-sea flux and Ekman heat transport, highlighting the importance of topography and mesoscale processes on the evolution of upper ocean temperature (Sallée et al., 2008; Vivier et al., 2009). Lateral eddy heat diffusion has been shown to contribute to substantial warming locally and is strongest downstream of major topographic features but vanishes with large-scale averaging (Sallée et al., 2008). Seasonal variability in the mixed layer heat budget is dominated by strong seasonal variability in the air-sea heat flux (Dong et al., 2007; Sallée et al., 2006) although Ekman temperature

advection also shows seasonal variability (Dong et al., 2007). Temperature tendency variance in the ACC mixed layer has been shown to be dominated by lateral advection, including both higher frequency transient eddies and lower frequency meanders (Vivier et al., 2009).

Previous observation-based heat budget calculations use simple mixed layer models that neglect important vertical physics due to a lack of sufficient subsurface observations (Vivier et al., 2009) and cannot completely close the heat budget primarily due to uncertainties in the air-sea flux datasets (Dong et al., 2007). The detailed spatial variability of the heat budget in the Southern Ocean is thus mostly unknown, particularly how the budget differs between regions with net air-sea heat gain and regions of air-sea heat loss. Eddy heat fluxes have been shown to be important in regions of the ACC (e.g. Sallée et al., 2006) but limited observations have made it difficult to diagnose the eddy contribution to the heat budget equation. Increased model resolution and improvement of ocean data assimilation techniques have prompted the development of eddy-permitting, multi-year state estimates of the ocean (e.g. Mazloff et al., 2010; Wunsch and Heimbach, 2013). A distinct advantage of analyzing the heat budget in a high-resolution, data-assimilating state estimate such as the Southern Ocean State Estimate (SOSE) is that the mass and heat budgets are closed at every grid point and vertical advective and diffusive processes are explicitly resolved or parameterized in the model. Additionally, numerous ocean observations in state estimates constrain the large scale upper ocean state so that the model representation of upper ocean stratification is consistent with observations, making it possible to explore the three-dimensional heat budget within the upper ocean.

The goal of this study is to examine the effects of ocean dynamics in the regions of ocean heat gain and loss along the ACC on the heat budget in the eddy-permitting, data-assimilating SOSE. This Southern Ocean heat budget analysis using

SOSE is timely and novel because of the improvement in air-sea fluxes through ocean state estimation compared with atmospheric reanalyses (Cerovečki et al., 2011) and the ability to fully close the heat budget at every grid point. Additionally, analysis of the upper ocean heat budget will provide insight into the role of surface heat flux as a component of buoyancy flux in setting the three dimensional structure and strength of the upper cell of the Southern Ocean meridional overturning circulation. In section 2 we describe the model and methods used in calculating the heat budget. The adjusted air-sea heat fluxes in the model are discussed in section 3, the heat budget and spatial and seasonal variability are analyzed in section 4. The results and conclusions are summarized in section 5.

2.2 Model and methods

2.2.1 The Southern Ocean State Estimate

The SOSE (Mazloff et al., 2010) is an eddy permitting, data assimilating model developed using software developed by the consortium for Estimating the Climate and Circulation of the Ocean (ECCO; `http://www.ecco-group.org`). The SOSE ocean dynamics is represented using the MITgcm (Marshall et al., 1997). The configuration of the model used here has 1/6° horizontal resolution and 42 vertical levels in the domain from 24.7°S to 78°S with an open northern boundary and a 900-s time step and sub-grid parameterizations as described in Mazloff et al. (2010). Using an adjoint method, the model is fitted to the majority of available observations in the Southern Ocean to minimize the squared difference between the model and observations iteratively by adjusting the "control vector" that consists of the initial conditions and atmospheric state. The initial and northern open boundary conditions are from a 1° global state estimate (Forget, 2010) and the initial atmospheric state is constrained by the ECMWF ERA-Interim

global reanalysis (Dee et al., 2011). Momentum, heat and freshwater fluxes between the atmosphere and ocean are determined using bulk formulae (Large and Yeager, 2009). The thermodynamic sea ice model is similar to that described by Fenty and Heimbach (2013) and includes albedo as a function of surface ice conditions and turbulent air-ice fluxes calculated using standard bulk aerodynamic formulae. The SOSE solution has been extensively validated and compared to observations (e.g. Cerovečki et al., 2013; Cerovečki and Mazloff, 2015). The SOSE adjusted air-sea fluxes have been validated against other available flux products and are consistent with the best modern flux estimates (Cerovečki et al., 2011). As expected, the largest differences between SOSE and other flux products tend to be in regions with strong mesoscale activity such as the ACC and western boundary currents.

2.2.2 Heat budget analysis

The SOSE iteration 100 solution used for this analysis is a 6-year (2005-2010), updated version of the solution described by Mazloff et al. (2010). Terms in the heat and salt budgets are diagnosed at each grid point from the model state and output as 5-day averages. The time evolution of temperature in the ocean is given by the sum of net heat exchange with the atmosphere, divergence of advective heat transport by both geostrophic horizontal, ageostrophic horizontal and vertical velocities, and 3-dimensional diffusive processes:

$$\underbrace{\frac{\partial T}{\partial t}}_{\text{temperature tendency}} = \underbrace{\frac{Q(z)}{\rho c_p dz}}_{\substack{\text{air-sea}\\ \text{flux}}} - \underbrace{\mathbf{u_g}\cdot\nabla_H T}_{\substack{\text{geostrophic}\\ \text{advection}}} - \underbrace{\mathbf{u_a}\cdot\nabla_H T}_{\substack{\text{ageostrophic}\\ \text{advection}}} - \underbrace{w\cdot\frac{\partial T}{\partial z}}_{\substack{\text{vertical}\\ \text{advection}}} + \underbrace{\kappa_H\nabla_H^2 T + \kappa_z\frac{\partial^2 T}{\partial z^2} + K_T^{turb}}_{\text{diffusion}} \tag{2.1}$$

where T is potential temperature, $\partial T/\partial t$ is the temperature tendency, Q is the

net air-sea heat flux in W/m^2 (positive is heat flux into the ocean) that includes depth-dependent shortwave radiation distributed vertically over several upper model layers, ρ is the density, c_p is the specific heat capacity of seawater, dz is the thickness of the model layer over which Q is distributed, $\mathbf{u_g}$ and $\mathbf{u_a}$ are the geostrophic and ageostrophic horizontal velocity vectors, respectively, ∇_H is the horizontal divergence operator, w is the vertical velocity, κ_H and κ_z are the horizontal and vertical diffusivity respectively, and K_T^{turb} is the K-profile parameterization (KPP) turbulent vertical diffusion term (Large et al., 1994). The KPP turbulent diffusion includes both vertical diffusion term and non-local transport to represent convective mixing; the two tend to oppose each other in the surface boundary layer. In SOSE, penetration of downward shortwave radiation below the surface is based on an assumption of exponential decay with depth (Paulson and Simpson, 1977), following Jerlov (1968)

$$Q(z) = Q(0)\left[R\exp\left(\frac{z}{\gamma_1}\right) + (1-R)\exp\left(\frac{z}{\gamma_2}\right)\right] \tag{2.2}$$

where $Q(0)$ is the downward shortwave radiation at the sea surface, z is depth and R, γ_1 and γ_2 are constants for water type IB as defined by Jerlov (1968). Shortwave radiation typically decays to 10% of its surface value in the upper 25 m and to below 1% by 75 m, so the heat budget solution is only significantly affected by the choice of water type in the upper 50 m. Geostrophic velocities were calculated for this analysis from the model hydrostatic pressure, and ageostrophic velocities were calculated here as the residual between the model velocity and calculated geostrophic velocity. Geostrophic horizontal advection and vertical advection were further decomposed into time-mean and transient eddy advection terms

$$\overline{u_g' T'} = \overline{u_g T} - \overline{u_g}\,\overline{T} \tag{2.3}$$

$$\overline{w' T'} = \overline{wT} - \overline{w}\,\overline{T} \tag{2.4}$$

where overbars denotes a 3-month seasonal mean and primes denote a deviation from this seasonal mean in the 6-year model run. This eddy definition is chosen based on the decorrelation time scale of 34 days in the ACC estimated from altimeter data by Gille and Kelly (1996).

For brevity, each of the terms in Eq. (2.1) will be referred to using the label indicated on the equations. For example, divergence of geostrophic temperature transport will be referred to simply as the geostrophic advection term. In the analysis the heat budget will be examined in two ways. First, horizontal maps of the heat budget terms in Eq. (2.1) vertically integrated over the upper ocean are presented to show major spatial patterns. Second, to focus more closely on zonal variations in the heat budget at every model grid point is integrated meridionally between ACC streamlines and vertically over the upper ocean. Identifying a robust streamline in the ACC is difficult due to the non-stationary and segmented fronts of the ACC but we choose to define streamlines using sea surface height (SSH) contours following numerous previous studies (e.g. Sokolov and Rintoul, 2009). The upper boundary of integration is the ocean surface and the lower boundary is 624 m, which is the model layer depth that includes the deepest winter mixed layers. This depth encompasses the top 20 model layers and below this level the spatially averaged temperature variance is greatly reduced. The heat budget terms are integrated to a constant depth level rather than to an isopycnal surface, as this method simplifies the analysis and volume is conserved. Modest adjustments to the depth of the lower boundary have little influence on the conclusions presented here.

2.3 Heat Budget

2.3.1 Time-mean air-sea heat flux

The most prominent feature of the net time-mean air-sea heat flux in the SOSE solution is the intense cooling associated with the western boundary current regions, particularly the Agulhas Return Current (ARC) flowing eastward across the Indian Ocean east of South Africa (Fig. 2.1b). South of these heat loss regions in the Atlantic and Indian basins, between Drake Passage (DP) at 60°W and Campbell Plateau (CP) at 170°E, is a broad region of ocean heat gain at ACC latitudes that is strongest in the northern extension of the ACC at the Malvinas Current and south of the ARC in the Indian sector. In contrast to the rest of the ACC, the Pacific Ocean sector, from CP east to DP, is dominated by weak net surface ocean heat loss, although in a given year the annual-mean heat flux can be weakly positive or negative. The broad scale coherent patterns of heat gain and heat loss in SOSE are consistent with other recent air-sea heat flux products (Large and Yeager, 2009; Cerovečki et al., 2011). SOSE additionally shows mesoscale variations in heat fluxes due to adjustments to the oceanic observations. For the remainder of this paper, Atlantic/Indian refers to the Southern Ocean sector bounded on the west by DP and east by CP, and Pacific refers to the remaining section of the Southern Ocean. We argue that considering these two sectors of the ACC based on topographic features is more appropriate to the dynamics and air-sea exchanges in the circumpolar Southern Ocean than considering the three major basins typically used.

The spatial pattern in the SOSE net air-sea heat flux zonal anomaly (Fig. 2.1c) is dominated by latent heat flux (Fig. 2.1f) and less so by the sensible heat flux (Fig. 2.1g). Shortwave (Fig. 2.1d) and longwave (Fig. 2.1e) components show relatively small spatial variation, apart from a meridional gradient, and tend to compensate one another. Sensible heat flux depends directly on the air-sea temperature difference, ΔT,

while latent heat flux depends indirectly on ΔT through the influence of temperature on the air-sea humidity difference, Δq (e.g. Large and Yeager, 2009). Wind speed also modulates the strength of these turbulent fluxes but is not the dominant control as wind speed can act to amplify the flux but requires the presence of a temperature or humidity gradient. Therefore, latent and sensible heat fluxes tend to respond to spatial patterns and variability in sea surface temperature (SST) (Yu and Weller, 2007) and to spatial patterns in atmospheric temperature. The SOSE time mean zonal anomaly of SST (Fig. 2.1a) is dominated by a dipole with colder SST in the Atlantic/Indian and warmer SST in the Pacific, which is remarkably similar to the pattern in air-sea flux. Similar to SST and net air-sea heat flux, atmospheric temperature also shows a zonally asymmetric pattern, with the quasi-stationary zonal wave 1, defined as the first zonal harmonic of the geopotential height field, accounting for up to 90% of the Southern Hemisphere mean spatial distribution in atmospheric pressure (van Loon and Jenne, 1972; Hobbs and Raphael, 2010). Milliff et al. (1999) suggested the zonal wave 1 pattern may represent a coupled ocean-atmosphere mode, and Hobbs and Raphael (2007) find statistically significant correlations between SST and atmospheric zonal wave 1 throughout much of the Southern Ocean.

2.3.2 Time-mean heat budget

In all regions of the Southern Ocean the dominant heat balance, integrated vertically over the upper 624 m, is between air-sea flux (Fig. 2.2a) and the total divergence of temperature advection (Fig. 2.2b), while diffusion is negligible. Individually considered geostrophic, ageostrophic and vertical advection terms locally display strong spatial inhomogeneity with positive and negative values an order of magnitude larger than the air-sea flux values, which cancel in the sum, particularly in ACC latitudes and western boundary current regions that have high eddy kinetic energy. The geostrophic advection

term (Fig. 2.2c) tends to be positive (increasing temperature) in the western boundary currents and ACC latitudes and is negative in the subtropical gyres where there are equatorward flows and a strong meridional temperature gradients.

The ageostrophic advection term (Fig. 2.2d) is negative through most of the domain, decreasing the temperature, due to Ekman transport driven by westerly winds bringing cold water equatorward. Ekman transport calculated from SOSE wind stress accounts for > 90% of the variance in ageostrophic transport in most locations. Differences between Ekman transport and ageostrophic advection are localized close to shallow topography and in regions with high eddy variability (Fig. A1). In these locations, we expect ageostrophic processes other than Ekman transport to be important at scales smaller than the Rossby radius of deformation (Rocha et al., 2015). These scales are at the limit of the smallest scales that are resolved in SOSE (Chelton and Deszoeke, 1998). However, the integrated contribution of these non-Ekman ageostrophic transports to the total ageostrophic transport is negligible (Mazloff et al., 2010) (see Appendix for more details).

The vertical advection term (Fig. 2.2e) is generally positive (heating the upper ocean) in subtropical regions due to downwelling driven by Ekman pumping associated with wind stress curl. It is also positive along the Antarctic continental shelf where the vertical temperature gradient is reversed with colder water at the surface and relatively warm water upwelling from below. Within the ACC, but outside of locations with high eddy activity, the vertical advection term is negative (cooling) as upwelling brings colder waters toward the surface.

Integrated vertically over the upper 624 m, the diffusion term (Fig. 2.2f) is negligible except in deep water formation regions along the Antarctic coast that are not considered in this analysis. Although diffusion is small in the depth-integrated budget, diffusion is an important term in the mixed layer and is responsible for a large vertical

redistribution of heat near the surface. The diffusion is strong within the upper 100 - 200 m in most locations and positive and negative signals cancel when vertically integrated to depths below the mixed layer.

The temperature tendency (Fig. 2.2g) is small as air-sea heat flux is largely balanced by total divergence of temperature transport (Fig. 2.2a,b), although it shows some large scale spatial patterns. Given that the model run spans only 6 years, the temperature tendency patterns are most likely due to interannual variability rather than a long term trend. The temperature tendency in Argo gridded data (Roemmich and Gilson, 2009) over the same time period shows similar spatial structure but is of somewhat smaller magnitude than in SOSE, which may be due to small model drift. However, the magnitude of the temperature tendency trend from 2005 to 2010 is small relative to the total temperature variability.

Compared to the mean, $\overline{\mathbf{u_g}} \cdot \nabla_H \overline{T}$ (Fig. 2.3a), the eddy, $\mathbf{u_g'} \cdot \nabla_H T'$ (Fig. 2.3b), component of the geostrophic advection term is small except in regions with high eddy variability in western boundary currents and in the ACC, where it is of a similar magnitude to the mean geostrophic advection term. In particular, divergence of eddy heat flux is large near major topographic features including Kerguelen Plateau (60-80°E), Macquarie Ridge (150°E) and the Pacific-Antarctic Ridge (150°W) as well as CP and DP (Fig. 2.3b), consistent with observed enhancement of eddy kinetic energy and cross-frontal transport in these regions (Chelton et al., 1990; Thompson and Sallee, 2012).

The mean component of the vertical advection term, $\overline{w}\frac{\partial \overline{T}}{\partial z}$ (Fig. 2.3c), dominates the total vertical advection term outside of the energetic western boundary currents and ACC. Close to Kerguelen Plateau, at the Pacific-Antarctic Ridge and east of DP, the mean vertical advection term is strongly negative (Fig. 2.3c), while the eddy component of the vertical advection term, $w'\frac{\partial T'}{\partial z}$ (Fig. 2.3d), is positive; hence there is strong compensation between the mean and eddy components in these locations (Fig. 2.3c,d).

The spatial pattern in the vertical eddy advection term (Fig. 2.3d) is similar to that of the eddy component of the geostrophic advection term (Fig. 2.3b) and is positive in most regions, suggesting that this eddy term represents the vertical component of along-isopycnal eddy heat flux, which leads to warming by upward eddy flux along poleward tilted isopycnals with an along-isopycnal temperature gradient (Wolfe et al., 2008).

Fig. 2.4b shows the vertically integrated terms that are mapped in Fig. 2.2, also integrated meridionally within the ACC. ACC boundaries are defined as the outermost time-mean SSH lines that are closed through DP (Fig. 2.4a). Large magnitude, small scale variations are apparent in the advection terms that are concentrated in 'hotspots' close to coastlines and shallow topography and in eddy-rich regions that dominate the larger scale signals (Fig. 2.4b).

To more clearly visualize how each heat budget term varies as a function of longitude, the vertically and meridionally integrated terms (Fig. 2.4b) are cumulatively summed with longitude (Fig. 2.4c). There is net ocean heat gain of 0.27 PW in the circumpolar integral although the pattern of air sea heat gain in the Atlantic/Indian sector and air-sea heat loss in the Pacific is apparent. As in Fig. 2.2, the total geostrophic advection is generally negative or negligible in the Atlantic/Indian sector and positive throughout the Pacific sector of the ACC, with the exception of a region from 70-100°E in the Indian sector, downstream of Kerguelen Plateau and 0-30°W, at the Brazil-Malvinas Confluence where it is also positive. This localized region of convergence of geostrophic heat advection downstream of Kerguelen Plateau is likely due to warm, subtropical ARC waters crossing the Subantarctic Front southward into the ACC downstream of Kerguelen Plateau (Wang et al., 2014). Similarly, downstream of Drake Passage the positive geostrophic advection term can be attributed to cross-frontal flow of subtropical Brazil Current waters into the ACC. Again, the ageostrophic advection is consistently negative at all longitudes along the ACC associated with northward Ekman transport of

colder water (Fig. A1). The total vertical advection has a weak net cooling effect, with localized contributions at major topographic features implying topographic control of vertical heat exchange (Fig. 2.4c). The cumulative sum of temperature tendency shows that small positive and negative temperature trends, when summed cumulatively along the ACC, are a reassuringly small contribution to the heat budget. The cumulatively summed diffusion is negligible (Fig. 2.4c).

Decomposition of the horizontal geostrophic and vertical advection components into contributions from the mean flow and transient eddies (Fig. 2.4d) shows that both horizontal and vertical eddy heat flux divergence are warming the upper ocean. This warming by eddy heat flux divergence is confined to localized regions, predominantly in the Kerguelen Plateau region where warm ARC waters reach the ACC and, to a lesser extent, the Macquarie Ridge. In the circumpolar integral, the mean and eddy components of the geostrophic advection term are of similar magnitude. However, the mean geostrophic advection term (Fig. 2.4d) is responsible for the majority of the zonal variation observed in the total geostrophic advection term (Fig. 2.4c). There is substantial cancellation between the mean and eddy components of the vertical advection term leading to weak net cooling by the total vertical advection term that is consistent with previous modeling studies of vertical heat flux (Wolfe et al., 2008; Morrison et al., 2013). Both the mean and eddy components of the vertical heat advection term have large magnitudes in regions associated with major topographic features, and are generally negligible elsewhere. Due to the cancellation between mean and eddy vertical heat fluxes, the net contribution to the heat budget is small relative to the horizontal advection terms, and likely has been overestimated in studies that do not include eddy heat fluxes (Dong et al., 2007). Note that because the heat budget is integrated to a constant depth level rather than an isopycnal, there are vertical displacements in isopycnals along the ACC path that may appear as vertical heat flux, which are not associated with diapycnal

vertical velocities, but they are small.

The mean temperature along the ACC path (Fig. 2.4c, dashed black), averaged vertically and between the two SSH contours shown in Fig. 2.4a, shows that the ACC is warmer in the Atlantic/Indian sector and cooler in the Pacific sector. The ACC mean temperature ranges from 6°C in the Atlantic to 3°C in the southeast Pacific. This temperature difference is significant as the temperature variance in the core of the ACC is of the order 1°C in SOSE. This temperature contrast from the Atlantic to the Pacific was previously shown by Sun and Watts (2002) and earlier authors; Sun and Watts (2002) attributed the heat sources to the Brazil Current and the Agulhas Return Current, that is, to subtropical western boundary current sources. Although our results are in agreement with (Sun and Watts, 2002), our results also indicate that horizontal advection in the Atlantic/Indian sector is not solely responsible for the heat content variation along the ACC, that is, air-sea heat fluxes contribute about half of the necessary heat input (Fig. 2.4c). The temperature difference along the mean path of the ACC also has important implications for the contribution of the mean flow to poleward heat transport in the Southern Ocean as the poleward flowing section of the ACC carries more heat than the equatorard flowing Malvinas Current (Sun and Watts, 2002).

The circumpolar integral of terms shown in Fig. 2.4, as well as integrated separately over the Atlantic/Indian and Pacific sectors are listed in Table 2.1. The circumpolar integral of air-sea flux in the ACC shows 0.27 PW ocean heat gain, which is a result of 0.35 PW of heat gain in the Atlantic/Indian sector and -0.08 PW heat loss in the Pacific sector. As is the case for air-sea heat flux, the sign of the time-mean geostrophic advection term differs between the two regions, with -0.01 PW in the Atlantic/Indian and 0.24 PW in the Pacific. The contributions to the circumpolar integrated horizontal and vertical eddy advection terms are dominated by the Atlantic/Indian sector because this sector captures all of the major eddy-rich topographic features along the ACC path

excluding CP and Pacific-Antarctic Ridge. The circumpolar integral of the geostrophic advection term is 0.38 PW and 0.27 PW air-sea heat gain is balanced by the sum of -0.58 PW cooling due to the ageostrophic advection term and -0.09 PW cooling due to the total vertical advection term. Thus, in the circumpolar integral, the dominant balance is between the heat gain due to geostrophic advection and air-sea flux terms and the heat loss due to the ageostrophic advection term. However, when integrated over each ocean basin separately, in the Atlantic/Indian sector air-sea heat gain and the eddy component of geostrophic advection balance cooling by the ageostrophic advection term, while in the Pacific sector the mean geostrophic advection term balances cooling by the ageostrophic advection term and air-sea heat loss. The time-mean temperature tendency is small but negative (cooling) over the entire ACC although this signal is confined to the Pacific sector where air-sea flux tends to be negative.

2.3.3 Seasonal variability

The time-mean heat budget is the residual of a much larger seasonal cycle, where seasonal variation in temperature tendency is dominated by the seasonal cycle in air-sea heat flux (Fig. 2.5). The circumpolar integrated ACC air-sea heat flux ranges from -2 PW in winter to 3 PW in summer and on seasonal scales is predominantly balanced by the temperature tendency, with a small negative offset due to net cooling by the sum of the geostrophic, ageostrophic and vertical advection terms. Notably, the ageostrophic advection term does not show a strong seasonal cycle, differing from a previous observational study (Dong et al., 2007). This difference in seasonality of the ageostrophic advection term may be attributed to seasonal variations in the mixed layer depth boundary of the mixed layer model of Dong et al. (2007), whereas a constant depth of integration is used in this analysis. Alternatively, variability in the small non-Ekman component of the ageostrophic advection term on non-seasonal timescales may contribute to the

lack of clear seasonal variability in ageostrophic advection in SOSE. However, the magnitude of the ageostrophic advection term is slightly larger in winter and spring (Fig. 2.5c,e), consistent with the seasonal cycle in the strength and position of westerly winds that force the Ekman transport. The magnitude and zonal patterns in the geostrophic and vertical advection terms (Fig. 2.5) and their corresponding mean and eddy components (not shown) do not show significant seasonal variation, consistent with the conclusion that the spatial variations in the advection terms are related to topographic features and intrinsic ocean variability.

Time series of the 3-month averaged, depth-integrated heat budget integrated in the Atlantic/Indian and Pacific sectors separately (similar to Table 2.1) demonstrate the large seasonal cycle in temperature tendency that closely follows air-sea heat flux in magnitude and sign but with a slight negative offset as a result of the sum of the seasonal mean advection terms in the budget (Fig. 2.6 a and b). Temporal variations in the seasonally-averaged advection terms are relatively small and unlike air-sea heat flux, the sign of the advective terms remains constant in all seasons. Note that there is substantial variability in the heat budget terms on shorter timescales that is not considered in this analysis. There is a significant difference in the geostrophic advection term between the Atlantic/Indian and Pacific sectors that is of a similar magnitude to the difference in air-sea heat flux (Fig. 2.6c), but the difference in vertical and ageostrophic advection terms between the two regions is small relative to the standard deviation of these terms. We hypothesize that the mean geostrophic advection term differs spatially due to large scale differences in the meridional direction of the ACC flow along its circumpolar path, with small divergence of geostrophic temperature advection in the Atlantic/Indian where the ACC flows equatorward and convergence of geostrophic temperature advection in the Pacific sector where the ACC mean flow is poleward. This zonal difference in geostrophic heat transport is mostly compensated by the zonal difference in air-sea heat

flux, leading to only a small temperature tendency difference between the two regions. The next section is devoted to exploring the physical explanation for the zonal variation in geostrophic advection and heat flux along the ACC in more detail.

2.3.4 The role of geostrophic advection in the ACC heat budget

Poleward flowing western boundary currents and their extensions are sites of intense ocean heat loss as mean geostrophic advection brings warm, subtropical water poleward under a colder atmosphere (Vivier et al., 2002; Dong and Kelly, 2004). The Pacific sector of the ACC is analogous to a western boundary current extension, as the mean geostrophic transport of the ACC is poleward as it enters the Pacific, transporting ACC water under a colder atmosphere, causing large turbulent (latent and sensible) heat losses. The ACC then veers sharply equatorward in the Malvinas Current after passing through Drake Passage, under a relatively warm atmosphere where there is a minimum in turbulent heat loss, resulting in net heat flux into the ocean. To demonstrate the similarities between the poleward flowing ACC in the Pacific sector and poleward-flowing western boundary current extensions, particularly the ARC, it is useful to compare and contrast the heat budget in these two regions.

Fig. 2.7 shows the time-mean integrated heat budget solution in the ARC region similar to that shown in Fig. 2.4 for the ACC. Convergence of geostrophic and vertical temperature advection are balanced mainly by ocean heat loss, with a smaller contribution from the ageostrophic advection term (Fig. 2.7c). This balance is consistent with previous analyses of the heat budget in western boundary currents that show that geostrophic advection is balanced by heat loss to the atmosphere (Dong and Kelly, 2004; Roemmich et al., 2005). Decomposition of horizontal and vertical advection into the mean and eddy components (Fig. 2.7d) shows that the horizontal geostrophic advection term is the largest positive term, bringing warm subtropical water into the region. How-

ever, the eddy component of the geostrophic advection term is negative, leading to substantial cancellation between the mean and eddy contributions to the total geostrophic advection term. Both the mean and eddy vertical advection terms are positive in the ARC, which differs from the ACC because wind stress curl drives downwelling of warmer surface water rather than upwelling at this latitude. The ARC heat balance is similar to the dominant balance in the Pacific sector of the ACC (Fig. 2.4c), where mean geostrophic advection warms the upper ocean and is balanced by cooling from both air-sea fluxes and Ekman advection. There are a few other differences between the ARC and the Pacific sector of the ACC: air-sea heat loss is the dominant cooling term in the ARC, whereas in the Pacific sector of the ACC cooling by the Ekman advection term is larger than the air-sea heat loss term. Also, both mean and eddy vertical advection contribute to net warming in the ARC, while in the Pacific sector of the ACC the vertical advection term is negative with substantial cancellation between the time-mean and eddy components (Fig. 2.4d). Given the difference in vertical temperature structure and stronger Ekman transport in the ACC, these differences are unsurprising.

Time series of the ARC (not shown) indicate that there is large variability in the geostrophic and ageostrophic advection terms, unlike in the ACC where the temperature tendency is mostly balanced by air-sea fluxes on seasonal timescales (Fig. 2.6d). The variability in the geostrophic advection term in the ARC is dominated by large non-seasonal variations in the transport and recirculations in the current, obscuring the seasonal cycle. The resulting temperature tendency averaged over the entire ARC has a less pronounced seasonal cycle than in the ACC. In this highly energetic region, the quantitative heat budget results are only weakly sensitive to the boundaries of integration but the sign of the integrated terms does not change and the qualitative result remains consistent. While the role of geostrophic advection in the time-averaged heat budget is similar in the ARC and the Pacific sector of the ACC, the temporal variability in the

geostrophic advection term in the ARC is much larger than in the ACC, unsurprising given the large variability in transport due to recirculations in the ARC.

2.4 Summary and Conclusions

We have analyzed the 3-dimensional spatial variations and seasonal variability in the upper ocean heat budget of the Antarctic Circumpolar Current (ACC) in the Southern Ocean State Estimate (SOSE) for the years 2005-2010. SOSE is eddy permitting, well-constrained by ocean observations in the top 2000 m of the ocean and has closed budgets, providing new insights into the heat budget in the Southern Ocean compared to the previous studies of the heat budget that have been limited by sparse observations, unresolved mesoscale processes and inadequate surface heat fluxes, leading to large imbalances in the heat budget (Dong et al., 2007). The circumpolar integrated heat budget in the ACC in SOSE shows 0.27 PW of ocean heat gain from the atmosphere and 0.38 PW heat gain from divergence of geostrophic temperature advection are balanced by -0.58 PW cooling by divergence of Ekman temperature advection and -0.09 PW divergence of vertical temperature advection. A summary of the dominant heat budget processes is shown in Fig. 2.8. Our principal conclusions are:

- Large scale patterns of air-sea heat fluxes from SOSE agree with the most recent heat flux products (Large and Yeager, 2009; Cerovečki et al., 2011), showing a robust zonally asymmetric pattern in the ACC, with ocean heat gain in the Atlantic/Indian sector and ocean heat loss in the Pacific sector.

- In the Atlantic/Indian sector of the ACC, 0.35 PW of surface ocean heat gain is opposed by -0.42 PW cooling by divergence of ageostrophic heat advection due to Ekman transport, consistent with Dong et al. (2007) and Sallée et al. (2006).

0.14 PW warming due to divergence of geostrophic eddy heat flux and -0.06 PW cooling due to divergence of vertical heat advection play a lesser role.

- In the Pacific sector of the ACC, both -0.08 PW ocean heat loss to the atmosphere and -0.16 PW cooling by the divergence of ageostrophic heat advection due to Ekman transport are mainly balanced by 0.25 PW convergence of geostrophic heat advection. The warming by divergence of geostrophic heat advection is achieved almost entirely by the mean geostrophic flow, unlike in the Atlantic/Indian sector where the mean component is insignificant and instead is dominated by eddy heat flux divergence associated with major topographic features.

- Comparison of the ACC heat budget with the poleward-flowing, subtropical Agulhas Return Current (ARC) suggests the dominant heat balance in the Pacific sector of the ACC is similar to that in the ARC and other poleward flowing western boundary current extensions.

- Divergence of both horizontal and vertical transient eddy heat flux causes significant warming in narrow regions associated with major topographic features with enhanced mesoscale energy (e.g. Naveira Garabato et al., 2011).

- The seasonal cycle in air-sea heat flux has a magnitude of 200 Wm^2 and is predominantly balanced by the seasonal cycle of temperature tendency, while the divergence of temperature advection does not show a distinct seasonal cycle.

We have demonstrated that mean geostrophic temperature advection is a dominant component of the Southern Ocean heat budget due to meridional standing meanders of the ACC and to a lesser extent the inflow of warm, subtropical boundary current waters into the ACC across the Subantarctic Front (Fig. 2.8). This result supports the inference of Sun and Watts (2002) that since heat content varies along the mean ACC

path there must be an associated net poleward heat transport. Sun and Watts (2002) concluded that subtropical water, particularly from the Brazil-Malvinas Confluence, is responsible for the variation in heat content along the ACC mean path. Our results indicate that air-sea heat flux is also a major source of heat to the ACC mean flow in the Atlantic/Indian sector; this difference is likely due to availability of modern flux products that were not available to Sun and Watts (2002). The atmosphere above the Southern Ocean is more zonally uniform than the ocean because it lacks the strong topographic control that steers the ACC meridionally over a 10° latitude range. The ACC gains heat from the atmosphere when it flows northward in the Malvinas Current and throughout the Indian and Atlantic sectors, in addition to advective ocean heat input by the Brazil Current and ARC, and releases some of this heat back to the atmosphere as it flows southward in the Pacific (Fig. 2.8). This phenomenon is analogous to the heat exchange by horizontal gyre circulations, and we have shown that the ACC budget in the Pacific is similar to the budget in the ARC and other western boundary current extensions where relatively warm waters are advected poleward. Perturbation experiments in SOSE or other models would help to elucidate the physical mechanism linking geostrophic advection and air-sea heat flux, but are beyond the scope of this study.

The dominant role of northward Ekman transport in the heat budget is indicative of the surface branch of the upper cell of the Southern Ocean overturning circulation, with ocean heat gain throughout the Atlantic/Indian sector transforming Antarctic Surface Water to lighter water as it is advected equatorward. Instead, in the Pacific where the net heat flux is weakly negative, freshwater fluxes must achieve the surface buoyancy gain necessary to close the upper cell of the overturning circulation. Although the full buoyancy budget is beyond the scope of this study, the striking asymmetry in air-sea heat flux presented here is also present in the total buoyancy flux in the Southern Ocean (Cerovečki et al., 2013; Radko and Marshall, 2006). Further work is needed to inves-

tigate the impact of this asymmetric buoyancy forcing on the strength and structure of the overturning circulation, expanding on the idealized model presented by Radko and Marshall (2006).

Our results have important implications for climate models; they imply that models must have accurate spatial correlations between mean velocity and temperature fields in order to simulate the poleward heat flux by the ACC. Low resolution models that approximate the total ACC volume transport well but lack the narrow, intense jets and meandering structure of the current may be misrepresenting heat transport by the mean ACC flow (e.g. Dufour et al., 2012). Additionally, models that do not resolve eddies accurately lack the important contribution of warming by divergence of eddy heat flux to the heat budget in regions near major topographic features. While SOSE at 1/6° resolves the ACC jet structure better than global coarse-resolution models, there are unresolved finer scale processes that may alter the mean geostrophic heat flux. Further work is needed with the next generation of higher resolution products to explore the impact of model resolution on mean ACC heat transport.

Because of the importance of air-sea heat and freshwater fluxes in determining the strength of the upper cell of the overturning circulation (Radko and Marshall, 2006), the pronounced zonal asymmetry in the ACC heat budget shown in this work illustrates the need for further work to understand the three-dimensional structure of the overturning circulation in the Southern Ocean. Understanding how observed and predicted future changes in buoyancy forcing will alter the strength of the overturning circulation is a necessary step toward understanding the role of the Southern Ocean in future uptake and storage of heat, carbon and nutrients.

2.5 Acknowledgements

This work was supported by NSF grant OCE1357072. M. R. Mazloff acknowledges support from NSF grant PLR1425989. Computational resources for the Southern Ocean State Estimate were provided by NSF XSEDE resource grant OCE130007. The SOSE iteration 100 solution is freely available for download (`http:/sose.ucsd.edu`). We thank two anonymous reviewers for comments that improved the quality of this manuscript.

Chapter Two, in full, is a reprint of the material as it appears in the Journal of Climate, 2016. Tamsitt, V., L. D. Talley, M. R. Mazloff, and I. Cerovečki, (2016). Zonal variations in the Southern Ocean heat budget. *J. Climate*, 29(18), 6563-6579. ©American Meteorological Society. Used with permission. The dissertation author was the primary investigator and author of this paper.

2.A Comparison between Ekman transport from winds and ageostrophic transport.

Here we briefly show a comparison between Ekman transport calculated from wind stress and ageostrophic transport calculated from the residual between total and geostrophic velocities in the Southern Ocean State Estimate. The components of Ekman transport, U_{ek} and V_{ek} ($m^2\ s^{-1}$) integrated over the Ekman depth, d_{ek}, are estimated from the SOSE zonal and meridional mean wind stress fields, $\overline{\tau}^x$ and $\overline{\tau}^y$, according to the relations $U_{ek} = \frac{\overline{\tau}^y}{\rho f}$ and $V_{ek} = \frac{\overline{\tau}^x}{\rho f}$, where ρ is the density and f is the Coriolis parameter. The ageostrophic transport, U_{ag}, is estimated by taking the difference between the total velocity, u, and the geostrophic velocity calculated from the SOSE pressure field, u_g, and integrating vertically from the surface to d_{ek} such that $U_{ag} = \int_{-d_{ek}}^{0} (u - u_g)\, dz$. For

this comparison we assume a constant Ekman depth of 100 m, based on observations of Ekman transport in the Drake Passage (Lenn and Chereskin, 2009); however the qualitative difference between the Ekman and ageostrophic transports is not sensitive to this choice.

Fig. A1 shows that the differences between the zonal and meridional components of Ekman transport and ageostrophic transport are concentrated in energetic regions particularly western boundary currents and close to major topographic features where ageostrophic transport dues to processes other than Ekman transport are expected. These differences are noisy and don't have a sign preference. Thus when the ageostrophic advection is integrated meridionally and zonally, the non-Ekman contributions are not significant and the ageostrophic transport is a good approximation to the Ekman transport.

Table 2.1: SOSE 2005-2010 mean heat budget terms from Eq. (2.1) in PW integrated over the upper 624 m and between SSH lines as described in section 2 for the entire ACC and the Atlantic/Indian and Pacific sectors separately.

Heat budget term (PW)	Total	Atlantic/Indian	Pacific
air-sea flux	0.27	0.35	-0.08
geostrophic advection	0.38	0.13	0.25
mean	0.23	-0.01	0.24
eddy	0.15	0.14	0.01
ageostrophic advection	-0.58	-0.42	-0.16
vertical advection	-0.09	-0.06	-0.03
mean	-0.23	-0.18	-0.05
eddy	0.14	0.12	0.02
diffusion	0	0	0
temperature tendency	-0.02	0.00	-0.02

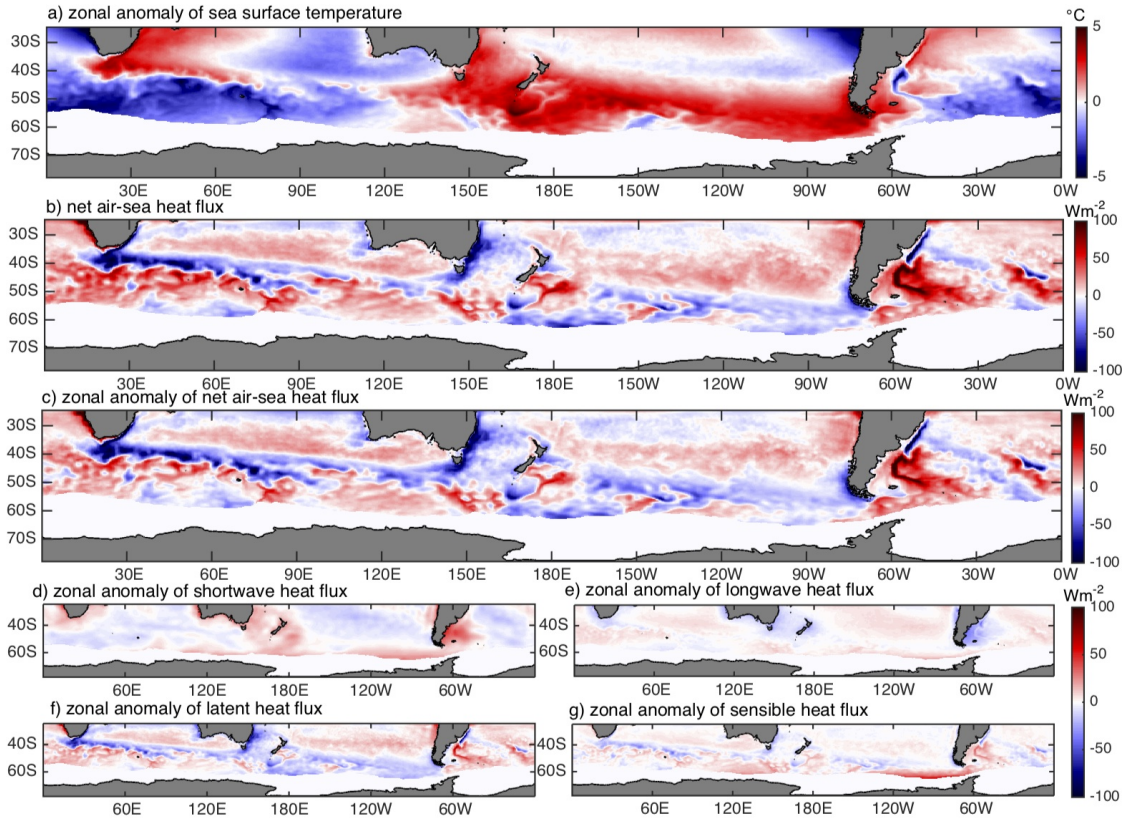

Figure 2.1: SOSE 2005-2010 mean of a) zonal anomaly of sea surface temperature (°C), b) net air-sea heat flux (W m^{-2}) with positive defined as heat flux into the ocean, c) zonal anomaly of net air-sea heat flux, d) zonal anomaly of net shortwave heat flux, e) zonal anomaly of net longwave radiation (incoming-outgoing) f) zonal anomaly of net latent heat flux and g) zonal anomaly net sensible heat flux. We have masked the temperature and fluxes in the region south of the 2005-2010 annual mean sea ice boundary where the fluxes are significantly influenced by sea ice as this region will not be considered in this analysis.

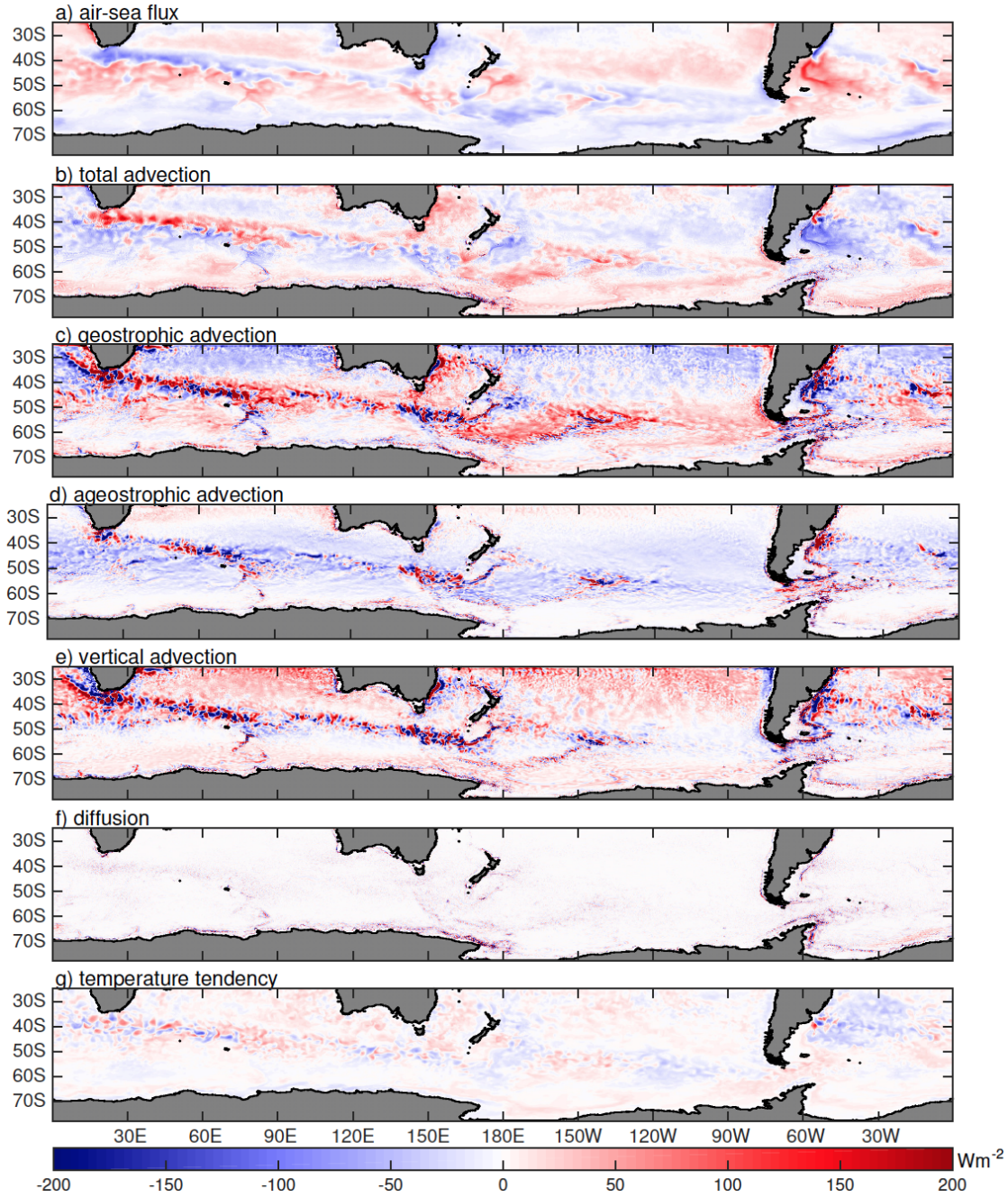

Figure 2.2: SOSE 2005-2010 mean heat budget terms from Eq. (2.1), integrated over the upper 624 m in W m^{-2}. Total divergence of temperature advection b) is the sum of the total geostrophic horizontal c), ageostrophic horizontal d) and vertical e) components of advection. Positive (red) is warming and negative (blue) is cooling.

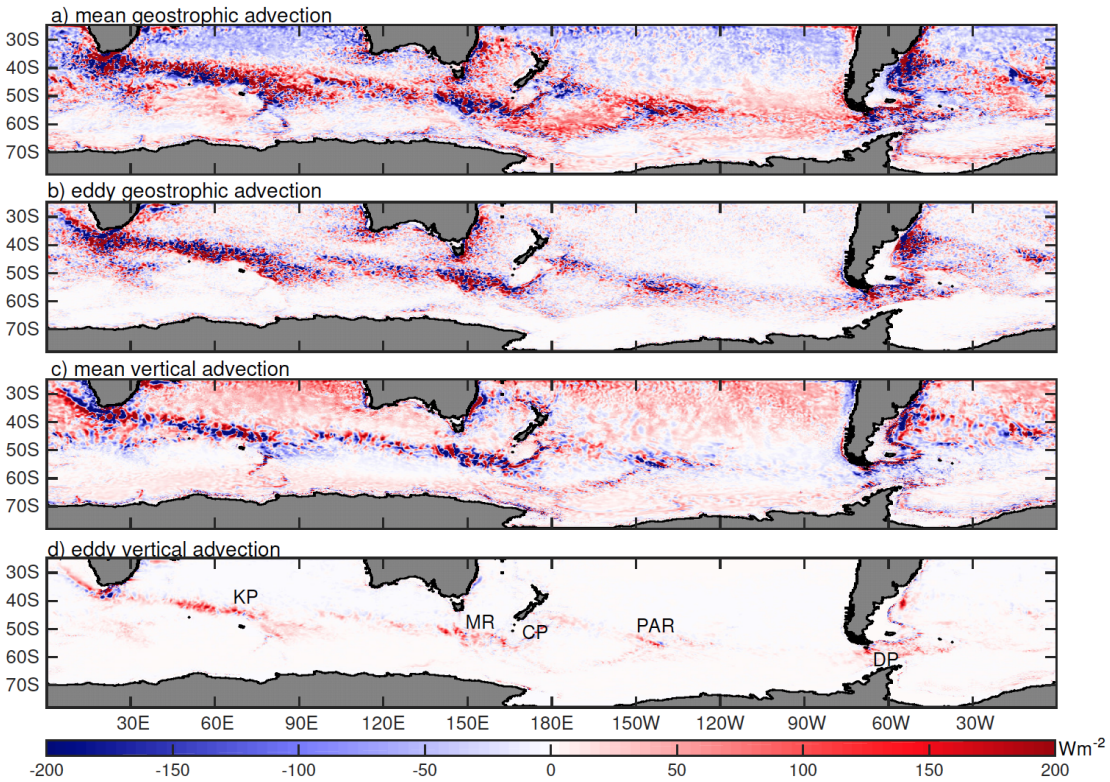

Figure 2.3: Similar to Figure 2.2 but for the time-mean and eddy components of horizontal geostrophic and vertical advection. The topographic features labelled on panel d) are from left to right: Kerguelen Plateau (KP), Macquarie Ridge (MR), Campbell Plateau (CP), Pacific-Antarctic Ridge (PAR) and Drake Passage (DP). Units are Wm^{-2}.

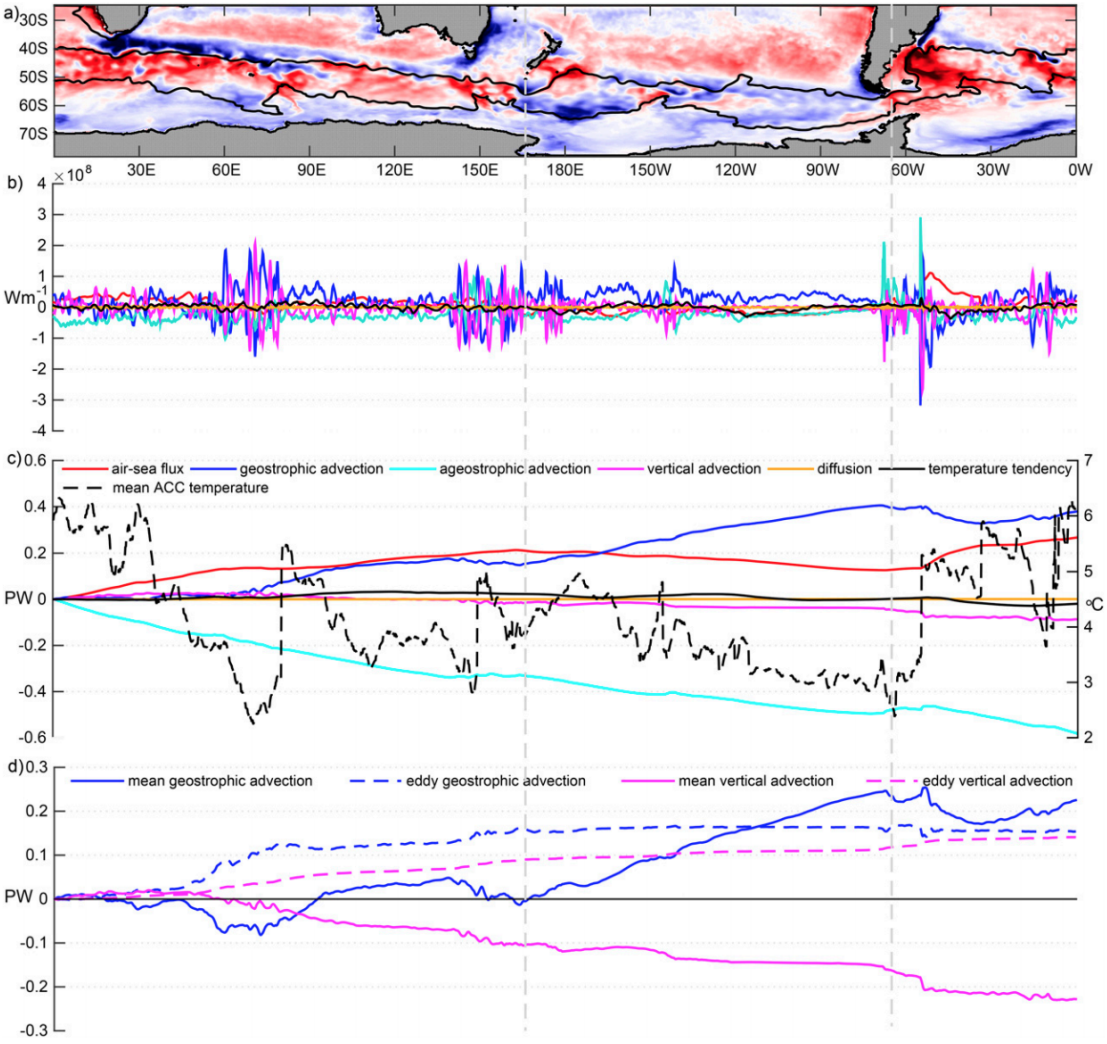

Figure 2.4: SOSE vertically and meridionally integrated heat budget solution: a) 2005-2010 mean net air-sea heat flux (colors) with SSH contours defining the northern and southern integration boundaries (solid lines), b) heat budget terms in Eq. (2.1) integrated to 624 m and between SSH contours (Wm^{-1})and c) cumulative sum of the terms in b) in PW as well as the mean temperature averaged vertically in the upper ocean (to 624 m) and between SSH contours in a) (black dashed line) and d) cumulative sum of mean and eddy contributions to the geostrophic and vertical advection terms (PW). Grey dashed lines mark Campbell Plateau and Drake Passage, separating the Atlantic/Indian sector from the Pacific sector. Total integrated values are listed in Table 1.

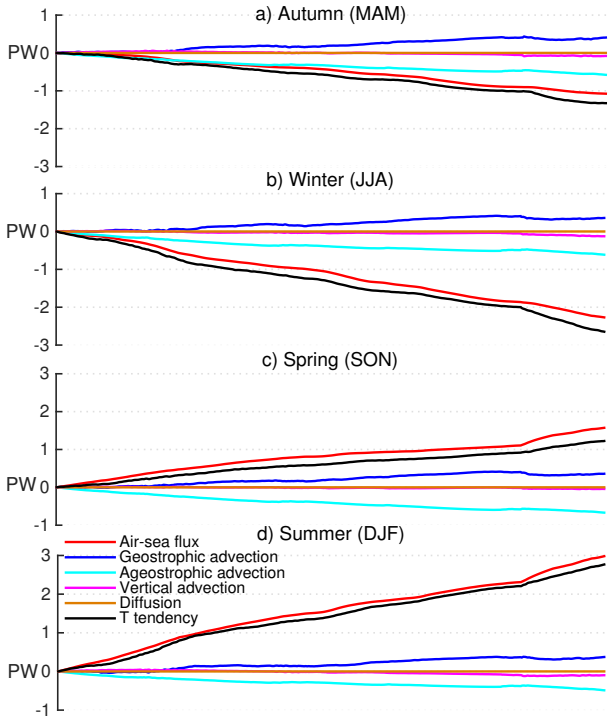

Figure 2.5: Cumulatively summed heat budget terms as in Figure 2.4 with each season separately, with the terms in Eq. (2.1): a) March, April, May (MAM), b) June, July, August (JJA), c) September, October, November (SON), and d) December, January, February (DJF). Note that the y axis limits in differs for each season to capture the large seasonal cycle in air-sea fluxes. All units are in PW.

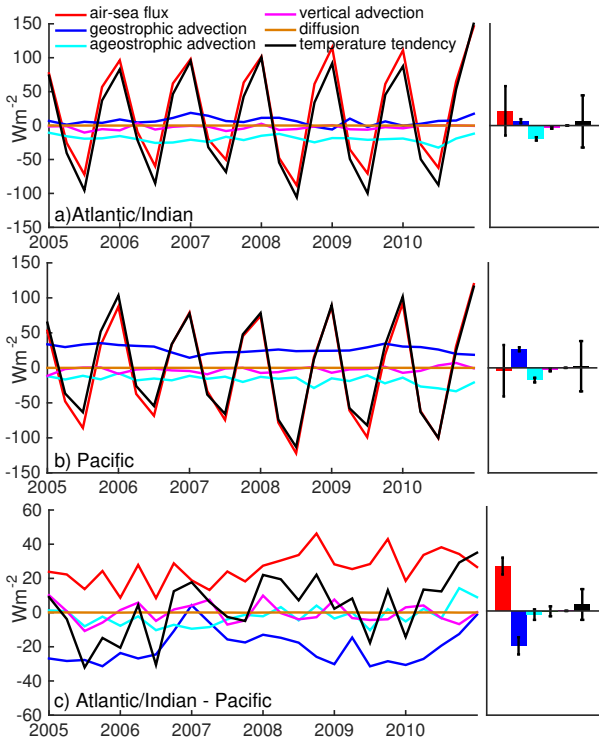

Figure 2.6: Time series of seasonal (3-month) integrated heat budget terms in Wm^{-2} (left) and time-mean terms (right) with error bars indicating one standard deviation above and below the mean for a) average of the Atlantic/Indian sector of the ACC, b) average of the Pacific sector of the ACC, and c) difference between a) and b).

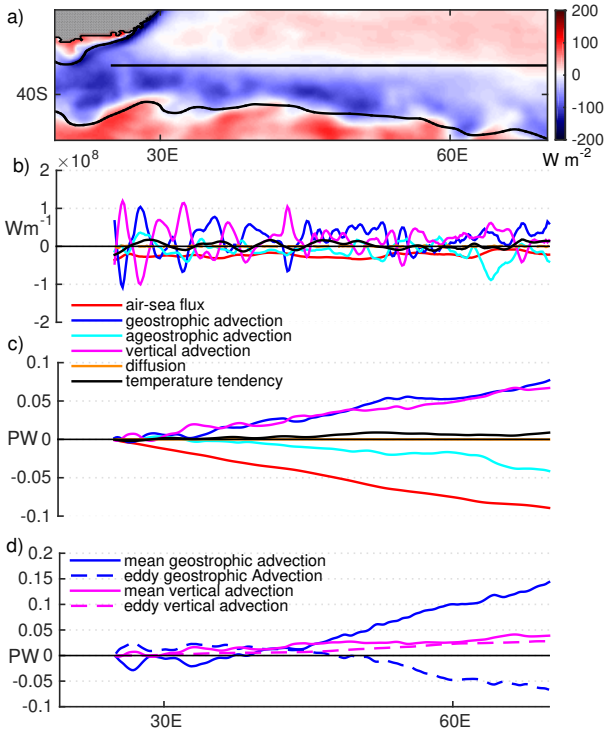

Figure 2.7: Integrated heat budget terms similar to Figure 2.4 for the Agulhas Return Current (ARC) cooling region: a) air-sea heat flux in the ARC region; black lines show the SSH contour used as the southern boundary and a line of constant latitude used as the northern boundary to integrate the heat budget terms in Eq. (2.1); b) heat budget terms in Eq. (2.1) integrated to 624 m and between meridional contours shown in a) (Wm^{-1}); c) cumulative sum of heat budget terms integrated to 624 m and between bounds in a); and d) cumulative sum of mean and eddy contributions to the geostrophic and vertical advection terms.

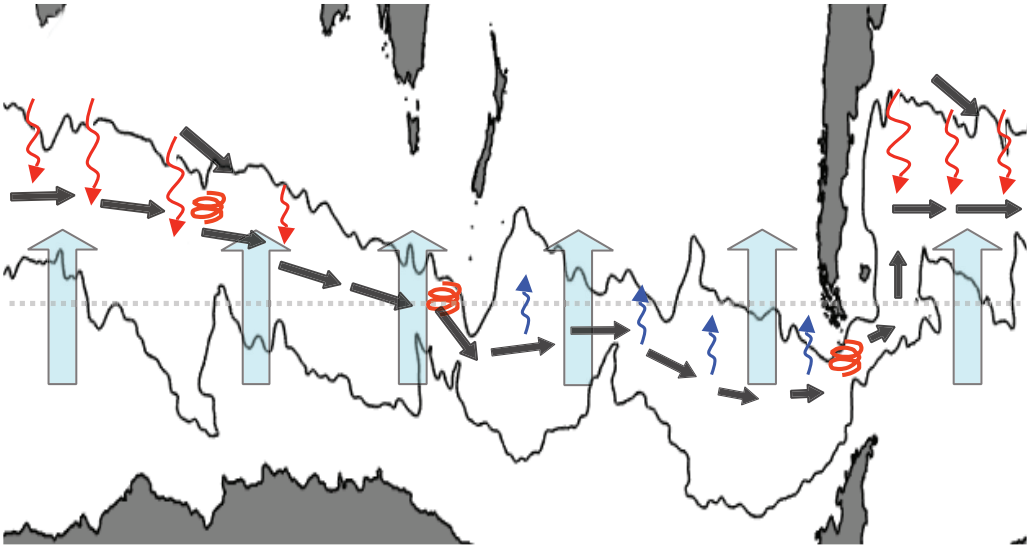

Figure 2.8: Schematic showing variations in the upper ocean heat budget along the ACC. Black lines are the SSH contours used as northern and southern boundaries of the ACC in this study. The dashed gray line marks the mean latitude of the ACC. Red and blue arrows indicate ocean heat gain and heat loss, large cyan arrows indicate cooling by divergence of Ekman temperature transport, dark grey arrows indicate the relative magnitude of the mean horizontal geostrophic transport, showing convergence in the Pacific sector and transport of subtropical water into the ACC from the ARC in the Indian sector and from the Brazil Current in the Atlantic sector, and red spirals indicate warming due to divergence of eddy heat flux associated with major topographic features.

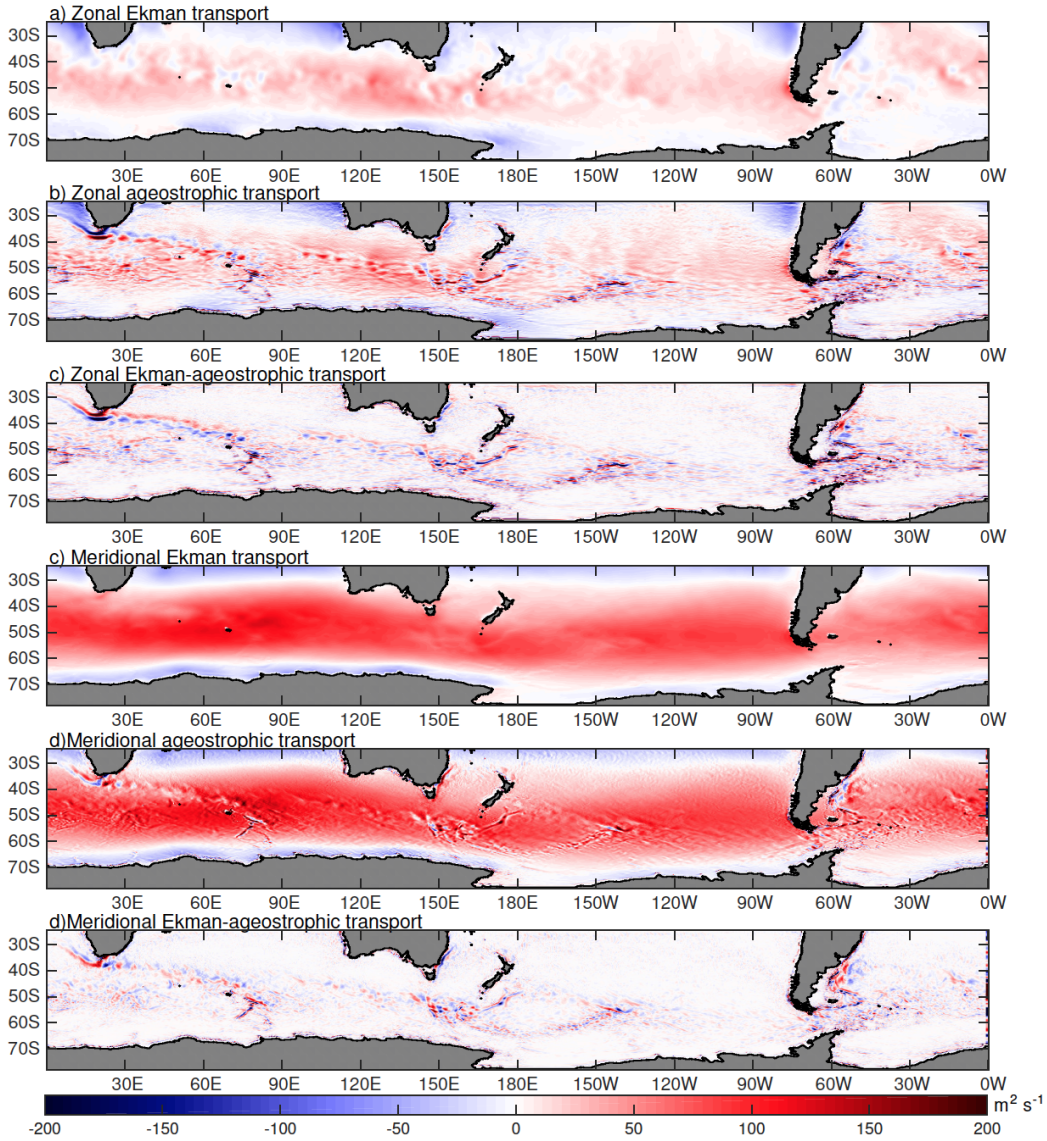

Figure 2.A1: Comparison between Ekman transport calculated from SOSE wind stress fields and ageostrophic transport calculated from the residual between total and geostrophic velocities integrated vertically over the Ekman layer. a) zonal Ekman transport, b) zonal ageostrophic transport, c) difference between zonal Ekman transport and zonal ageostrophic transport, d) meridional Ekman transport, e) meridional ageostrophic transport and f) difference between meridional Ekman transport and meridional ageostrophic transport.

Chapter 3

Spiraling pathways of global deep waters to the surface of the Southern Ocean

Abstract

Upwelling of global deep waters to the sea surface in the Southern Ocean closes the global overturning circulation and is fundamentally important for oceanic uptake of carbon and heat, nutrient resupply for sustaining oceanic biological production, and the melt rate of ice shelves. However, the exact pathways and role of topography in Southern Ocean upwelling remain largely unknown. Here we show detailed upwelling pathways in three dimensions, using hydrographic observations and particle tracking in high-resolution models. The analysis reveals that the northern-sourced deep waters enter the Antarctic Circumpolar Current (ACC) via southward flow along the boundaries of the three ocean basins, before spiraling southeastward and upward through the ACC. Upwelling is greatly enhanced at five major topographic features, associated with vigorous mesoscale eddy activity. Deep water reaches the upper ocean predominantly south

of the ACC, with a spatially nonuniform distribution. The timescale for half of the deep water to upwell from 30°S to the mixed layer is approximately 60-90 years.

3.1 Introduction

The global overturning circulation moves waters around the world's oceans, connecting surface and deep waters through two interlinked overturning cells, one with sinking in the far northern North Atlantic and adjacent Nordic Seas and the other with sinking along the Antarctic coastline (Marshall and Speer, 2012; Talley, 2013a). These processes are well documented, with the northern sites well mapped and the southern sites, in coastal polynyas, increasingly so (Nihashi and Ohshima, 2015). In contrast, the specific locations where these waters return back to the sea surface to complete the circuit are poorly known. Observations suggest that as much as 80% of the World Ocean deep water returns to the surface in the Southern Ocean with the remainder reaching the sea surface through upwelling to the thermocline in low latitudes (Lumpkin and Speer, 2007; Talley, 2013a). The vigor of the Southern Ocean return limb derives from the dynamics associated with the existence of an open circumpolar pathway around Antarctica in Drake Passage latitudes (Toggweiler and Samuels, 1998). Dense deep water is drawn upward along steeply tilted isopycnals (surfaces of constant density), driven by divergence of wind-driven Ekman transport and surface buoyancy forcing, enabling the return of deep water to the surface with minimal diapycnal mixing (Wolfe and Cessi, 2011; Watson et al., 2013). In the upper overturning cell, this upwelled water is transported northward via wind forcing and becomes lighter mode and intermediate waters. Below this, in the lower cell, the upwelled water is transformed into abyssal Antarctic Bottom Water (AABW) which sinks, moves northward, and is then converted to deep waters through diabatic mixing above the seafloor (Nikurashin and Vallis, 2011;

Naveira Garabato et al., 2016; Ferrari et al., 2016). The warm, upwelled water that nears the ice shelves of West Antarctica (Wå hlin et al., 2010) is recognized as a major factor in the high rate of ice shelf basal melt (Rignot et al., 2013); variability in upwelling is therefore one likely contributor to the accelerated melt rate documented in this region (Paolo et al., 2015), with long term consequences for sea level rise.

This major Southern Ocean return limb of the global overturning circulation is usually described in a two-dimensional sense (latitude-depth space), drawing on its parallel with the strongly zonally symmetric atmospheric dynamics. Mesoscale eddies have long been recognized as fundamental to the zonally-averaged view of the ACC, arising due to baroclinic instability associated with the sharply sloped isopycnals. In the upper ocean, southward eddy-induced transport directly opposes the northward Ekman transport, limiting the residual overturning magnitude and reducing the sensitivity of the overturning to strengthening westerly winds (Hallberg and Gnanadesikan, 2006; Morrison et al., 2013). Beneath the surface layer, eddies are the primary mechanism for the southward transport of deep water across the ACC fronts (Dufour et al., 2015), in the latitude and depth range that is unblocked by continental boundaries or topographic ridges ('Drake Passage effect') (Toggweiler and Samuels, 1995; Marshall and Speer, 2012). However, recent studies have demonstrated strong zonal variations in the Southern Ocean circulation, emphasizing the importance of taking into account the three-dimensionality of the circulation (Sallée et al., 2010; Thompson and Sallee, 2012; Naveira Garabato et al., 2011; Talley, 2013a; Dufour et al., 2015).

The southeastward pathway that the deep waters follow, entering from the basins lying to the north and then traveling around Antarctica until reaching the continental margin, is an aspect of the Southern Ocean circulation that is familiar from maps of the surface circulation. However, this circulation is rarely explored for its interaction with the upwelling of the deep waters along this path, and for the specific locations where en-

hanced upwelling occurs. The ACC spirals southeastward from its northernmost latitude just east of South America to its entry into Drake Passage from the Pacific, nearly 1700 km farther south(Orsi et al., 1995). The southward shift is consistent with a vorticity balance in which mean advection of planetary vorticity by the ACC balances vorticity generation by wind stress curl (i.e. Sverdrup balance). Previous work has noted the existence of a spiral structure in the Southern Ocean upwelling (Döös, 1995). However, to date the detailed geographic distribution and mechanisms for the upwelling along this ACC path have been largely unexplored.

The time scale for deep waters to reach the sea surface from each of the northern basins is important, both for setting the temporal response in the Southern Ocean to major changes in northern deep water formation rates (WAIS Divide Project Members, 2015) and for its control on biogeochemical processes that affect climate (Frölicher et al., 2015; Sarmiento et al., 2004). Relatively carbon-poor North Atlantic Deep Water mingles with much older, carbon-rich Indian and Pacific Deep Waters and all rise to the surface (Talley, 2013a). The relative amounts and time scales of these different northern deep water components impact the near-surface, upwelled ocean carbon and nutrient content and the heat supply to the Antarctic margins.

We document here the three-dimensionality of upwelling from the deep ocean interior to the surface of the Southern Ocean with observations and three independent, state-of-the-art, eddying ocean and climate models. Our analysis reveals the locations where the deep waters are most strongly shifted upwards and where they reach the sea surface. We find that upwelling along the southeastward spiral is not uniform. Where the ACC encounters major topographic features, flow-topography interactions create localized energetic eddy 'hotspots' (Chelton et al., 1990), which drive enhanced cross-frontal exchange (Thompson and Sallee, 2012; Dufour et al., 2015). Here we show for the first time that deep water upwelling is also strongly enhanced at these hotspots. We

also give a first estimate of the time scales of this upwelling and relative contributions of deep waters from the Atlantic, Indian and Pacific to upwelled waters in the Southern Ocean.

3.2 Results

3.2.1 Three-dimensional deep water spiral.

The broad three-dimensional pathway of upwelling in the Southern Ocean is illustrated using observed properties (Orsi and Whitworth, 2005) along a surface representing North Atlantic Deep Water (NADW; the neutral density surface 28.05 kg m^{-3}; Fig. 3.1a, Fig. 3.A1). The relatively warm, saline NADW, represented in Fig.3.1a by waters warmer than 1.6°C, enters the Southern Ocean from the deep Atlantic (2800 m depth) and spirals southeastward and upward through the ACC. Waters warmer than 1°C on this neutral density surface approach the Antarctic continental shelf (500 m depth) along the West Antarctic Peninsula and Amundsen Shelf south of 60°S, where incursions of upwelled, warm, northern-sourced deep waters have been implicated in the accelerated melting of ice shelves (Cook et al., 2016). Associated maps show the separate entrances of high nutrient/low oxygen Indian and Pacific Deep Waters (IDW and PDW) into the southeastward spiral (Fig. 3.A1 and Supplementary Note 1) (Orsi and Whitworth, 2005). The spiraling paths of NADW/IDW/PDW properties mostly follow the ACC fronts, and, upon close inspection, appear to cross fronts downstream of major topographic features (Fig. 3.A1).

More detailed geographic description and timescales of upwelling are difficult with the sparse Southern Ocean hydrographic data sets. We therefore use a Lagrangian modeling approach to quantify Southern Ocean upwelling and explore mechanisms controlling its pathways. We track virtual particles and their associated volume transports

(particle-transport) from the deep ocean interior (1000-3500 m layer) at 30°S until they reach the mixed layer in three independent eddying models: the Community Earth System Model (CESM), the Geophysical Fluid Dynamics Laboratory's Climate Model version 2.6 (CM2.6), and the Southern Ocean State Estimate (SOSE; See Methods for model and particle tracking details). We note that while the 1000-3500 m depth range spans a broad range of deep water densities, the focus here is on interior upwelling away from bottom boundary layer processes, rather than the upwelling of AABW from the abyssal ocean.

Modeled particles from the deep Atlantic preferentially spiral southeastward and upwards through the ACC (Fig. 3.1b,c and Video 3.1 using CM2.6; CESM and SOSE results are qualitatively similar). Similar spirals are also clear for modeled particles released in the Pacific and Indian Oceans (Fig. 3.A2, Videos 3.2-3.3 and Supplementary Note 2). The modeled Atlantic spiral (Fig. 3.1b) strongly resembles the observed pathway of the warm, saline NADW (Fig. 3.1a), although a different diagnostic is used (temperature on an isopycnal for the observations and probability of passing through a grid box for the models). Additionally, the model (Fig. 1b) also shows the preferred boundary current pathways from 30°S and the near-surface continuation of the NADW pathway along the Antarctic coast, which is unclear in the NADW temperature maximum due to mixing with colder surrounding waters before reaching Antarctica.

A comparison of the time-mean volume meridional transport at 30°S in CESM, CM2.6 and SOSE shows reasonable agreement in the magnitude and spatial structure of volume transport (Fig. 2). The vertically integrated southward volume transports in the 1000-3500 m depth range agree closely in the Pacific, with the largest differences in the western Atlantic and western Indian Ocean. The total Eulerian southward transport across 30°S between 1000 m and 3500 m is 28.8, 22.7 and 32.9 Sv in the CESM, CM2.6 and SOSE, respectively. These southward transports are slightly larger than the

net transport in the southward limb of the zonally averaged overturning streamfunction (Fig. 3.3; 24.4, 21.1, and 29.0 Sv in the CESM, CM2.6 and SOSE, respectively).

By comparison, the total Lagrangian upwelling particle-transport reaching the mixed layer south of 30°S is 13.2, 11.6, and 21.3 Sv in CESM, CM2.6, and SOSE, respectively. For all models, the Lagrangian transports are less than the Eulerian and overturning streamfunction transports. The two are not expected to agree in this case, and this is largely due to our definition of Lagrangian transport, whereby we only select particle trajectories that reach the mixed layer. In the overturning streamfunction, there is a portion of the southward upwelling limb that is entrained into either intermediate or abyssal waters in the interior without ever reaching the mixed layer. Additionally, there is likely a small fraction of Lagrangian particle-transport that takes longer than 200 years to upwell and thus is not captured in our total transport. NADW dominates the total upwelling particle-transport in all three models (51% in CM2.6 and CESM, 41% in SOSE), with the remaining transport split almost equally between the Indian and Pacific deep waters.

The time taken for particles to travel from 30°S to the mixed layer is in the range of decades to more than a century, with peak upwelling occurring at 41, 28 and 81 years after release in CESM, CM2.6 and SOSE, respectively (Fig. 3.4a, Table 3.1). We note that these transit times are considerably faster than a previous estimate of 140 years from a relatively coarse resolution (non-eddying) model(Iudicone et al., 2008c). We hypothesize from this previous study and our results that upwelling timescales are resolution dependent, which would explain the slower upwelling in the 1/6° SOSE compared to the 1/10° CESM and CM2.6. In CM2.6 and CESM, the median upwelling time for particle-transport originating in the Indian Ocean is slightly longer than the Atlantic and Pacific, while in SOSE, particle-transport from the Pacific takes substantially longer to upwell than from the Indian and Atlantic (Fig. 3.4b,c,d). There is a distinct difference

in upwelling from the Indian in SOSE relative to CESM and CM2.6, with large initial upwelling in the first 25 years (Fig. 3.4c, green line). This may arise from the relatively large particle-transport carried along the western boundary of the Indian Ocean by the Agulhas Current in SOSE, which leads to rapid coastal upwelling from the depths in the shallower part of the 1000-3500 m range.

The three-dimensional upwelling picture (Fig. 3.1b) is quantified for particle trajectories from all ocean basins in a two-dimensional view (Fig. 3.5), revealing the horizontal pathways of upwelling and their relative strengths. Particle-transport originating in the Atlantic, Indian and Pacific Oceans at 30°S flows southward before merging into the ACC. From here, up to 20% of the total particle-transport, depending on the model and basin of origin, move into parts of the Ross and Weddell Gyres and along the Antarctic coast. The pathways in Fig. 3.5 are remarkably insensitive to minor variations in the Lagrangian method (Figs 3.A3,3.A4,3.A5 and Supplementary Note 3). There are two distinct types of pathways into the ACC: via deep western boundary currents (DWBCs) along continents or topographic ridges, and along eastern pathways whose dynamics may be eddy-driven (Van Sebille et al., 2012). DWBCs are the shortest and fastest routes and have been previously identified in Lagrangian experiments (Döös et al., 2008). The DWBCs carry deep water beneath the Brazil Current in the Atlantic, beneath the Agulhas Return Current in the Indian, and broadly below both the East Australian Current in the Tasman Sea and East Auckland Current around New Zealand and out into the deep Pacific following topography. Another deep boundary pathway in the mid-Indian Ocean follows topographic ridges, especially the Southwest Indian Ridge (McDonagh et al., 2008).

The eastern pathways in each ocean basin are less documented than the DWBCs. Part of the NADW leaves the Atlantic just west of South Africa, having crossed the South Atlantic at mid-latitude, consistent with both observations and models (Reid,

1994; Garzoli et al., 2015). This pathway is hypothesized to be driven by southward eddy thickness fluxes imposed by the northwestward movement of shallow Agulhas rings (Van Sebille et al., 2012). While the current has been identified in observations at 115°E by its eastward transport and low oxygen content (Hufford et al., 1997), characteristic of IDW (Talley, 2013b), its global impact has not been appreciated and its physical cause has not been shown. We hypothesize that the eastern Atlantic eddy thickness flux mechanism (Van Sebille et al., 2012) may also operate in the Indian, driven by eddy transport south and west of Tasmania and flowing along the southern coast of Australia (Speich et al., 2002). In the eastern Pacific, a broad meandering pathway carries PDW southward, as identified in hydrographic observations (Reid, 1997; Faure and Speer, 2012). An inverse model of the Southeast Pacific circulation indicates that eddies likely play an important role in this pathway, but more work is needed to understand the underlying dynamics (Faure and Speer, 2012).

Although there is good agreement on the location of pathways in the three models, there are differences in the relative strengths of individual upwelling pathways. In particular, the contribution of the Pacific to the total particle-transport is relatively large in SOSE, and the strength of the eastern Indian and Pacific pathways varies significantly across the models. These differences are likely attributable to differences in meridional transport at 30°S in each model (Fig. 3.2) or differences in model spatial and temporal resolution (see Methods). Thus, we focus on the features that are common to all three models.

3.2.2 Topographic upwelling hotspots.

Fig. 3.5 shows the spatial distribution of particles at their final crossing of depth surfaces while upwelling. Upwelling in the ocean interior within the southeastward spiral is concentrated at the five major topographic features crossed by the ACC (shown in

Fig 6a,b for CM2.6 and Figs 3.A6,3.A7 for CESM and SOSE). These hotspots dominate the total upwelling across depth surfaces, with more than 55% of the total particle-transport upwelling across the 1000 m depth surface occurring in these five topographic hotspots in all three models, which span only 25% of the total zonal extent of the Southern Ocean (shaded in grey in Fig.3.6a). These hotspots occur within the ACC boundaries, so that most of the upwelling across 1000 m occurs within the ACC latitude range, between 40°S and 60°S (Fig. 3.6c). We note that there is also enhanced upwelling north of the ACC in the southward flowing western boundary currents, but we focus our attention on the mechanism for upwelling hotspots within the ACC.

The strongly localized distribution of upwelling at 1000 m differs from the uniform upwelling expected from wind stress curl over the Southern Ocean. The hotspots of upwelling within the ACC at 1000 m occur in regions of high eddy kinetic energy (EKE, see Methods for definition) associated with topography (blue contours in Fig. 3.6a,b, Figs 3.A6,3.A7 and Supplementary Note 4), where interactions between the mean flow and topography enhance eddy activity (Witter and Chelton, 1998; Thompson and Sallee, 2012). Recent studies have shown preferential southward transport of particles and tracers across ACC fronts in the upper 1500 m at topographic hotspots (Thompson and Sallee, 2012; Dufour et al., 2015). Our results show the central role of these same topographic hotspots in raising particles toward the surface as they follow the ACC path. The mean particle-transport crossing 1000 m in all regions where EKE exceeds 75 cm^2s^{-2} is an order of magnitude larger than the mean elsewhere, and there are statistically significant correlations between mean EKE at 1000 m and particle-transport crossing the 1000 m depth surface within the ACC of 0.33, 0.65, and 0.56 in CESM, CM2.6 and SOSE, respectively (Pearsons correlation coefficient with p-value<0.01). Within the ACC, EKE and upwelling at 1000 m are not expected to align perfectly, because all upwelling hotspots are associated with elevated EKE, while not all regions with high

EKE also have enhanced upwelling. Only locations that lie along the three-dimensional deep water pathways (Figs 3.1b, 3.5) at the 1000 m depth surface will show enhanced upwelling.

The upwelled water in the three models reaches the surface layer, represented by upwelling across 200 m (Fig. 3.6d,e,f and Figs 3.A6,3.A7), mostly along the Southern Boundary of the ACC and over broader spatial scales than the interior upwelling hotspots. This upwelling coincides with a region of enhanced buoyancy gain by surface freshwater fluxes from melting sea ice (Abernathey et al., 2016). The remaining upwelling transport reaches the surface throughout the subpolar gyres and along the Antarctic coastline, where it is exposed to buoyancy loss and may contribute to the formation of Antarctic Bottom Water. Even at 200 m, the broad distribution of upwelling, which is consistent with the broad pattern of negative wind stress curl, contains some localized enhancements associated with topographic hotspots (Fig. 3.6d). This agrees with a previous Lagrangian analysis that found enhanced upwelling into the surface ocean at topographic features (Viglione and Thompson, 2016). For example, upwelling across 200 m is enhanced in all three models at the Kerguelen Plateau, Macquarie Ridge and Pacific-Antarctic Ridge, although there are substantial differences in the relative importance of these hotspots at 200 m between the models (Fig. 3.6f and Figs 3.A6,3.A7). These differences in particle-transport at the 200 m depth surface compared to 1000 m indicates that differences in upper ocean processes between models impact the 200 m upwelling distribution, although lower spatial resolution could also contribute to the difference between SOSE and the two higher resolution models.

A schematic of a representative Southern Ocean upwelling pathway along an isopycnal surface is shown in Fig. 3.7. Deep waters move southward from 30°S along isopycnals that are at roughly constant depth, primarily in deep boundary currents, until joining the ACC where they follow the meandering paths of the ACC fronts (red

pathway in Fig. 3.7). Eddy advection drives flow across the ACC fronts in the ocean interior (yellow arrows). Within the ACC, isopycnals slope strongly upwards towards the surface, and simultaneously thin towards the south (Fig. 3.7b). Eddies act to reduce the meridional thickness gradients, hence advecting water southward and upward along isopycnals. The upwelling pathways indicate that, between topographic features, particles primarily follow mean ACC streamlines around Antarctica (Fig. 3.5 and schematically in Fig. 3.7). Where ACC fronts encounter topographic features, baroclinicity increases; strong eddy fields then develop downstream of topography (Thompson and Sallee, 2012), advecting water southwards and upwards along isopycnals. Therefore upwelling particles generally approach topographic features along more northerly ACC fronts and at greater depths, and exit downstream along more southerly ACC fronts and at shallower depths (Fig. 3.7b). Thus, the three-dimensional spiral is a superposition of the large-scale southeastward path of the mean ACC fronts from the Atlantic to the Pacific, and eddy-driven 'steps' southward and upward across fronts at topographic hotspots. This upwelling motion along particle trajectories can be visualized as a spiral staircase.

While we propose that along-isopycnal eddy transport is the dominant mechanism for upwelling at topographic hotspots within the ACC, diapycnal mixing may also play a non-negligible role in the upwelling of deep water at these hotspots. Observations suggest that interior diapycnal mixing is an important component of the Southern Ocean overturning (Sloyan and Rintoul, 2001a; Naveira Garabato et al., 2004; Katsumata et al., 2013; Naveira Garabato et al., 2016), particularly in the upper 1000 m and 1000-2000 m above the seafloor (Naveira Garabato et al., 2016). Additionally, it has been shown in Drake Passage that the strength of abyssal mixing is dependent on local eddy energy (Sheen et al., 2014). In this work, the focus on upwelling at hotspots associated with enhanced eddy activity is at mid-depths away from the surface or seafloor topography.

In the mid-depth ocean, along-isopycnal processes are expected to dominate over diapycnal processes. An analysis of the extent to which the interior upwelling pathways are adiabatic, and quantification of the diapycnal density change along Lagrangian trajectories at the upwelling hotspots is outside the scope of this study and is the subject of ongoing work.

3.3 Discussion

From our results we propose a new paradigm for the upwelling branch of the Southern Ocean overturning circulation that consists of a three-dimensional spiral, with most of the subsurface upwelling concentrated at the five major topographic features encountered by the ACC (Fig. 3.6): the Southwest Indian Ridge, Kerguelen Plateau, Macquarie Ridge, Pacific-Antarctic Ridge and Drake Passage. The spatial structure of upwelling and mechanisms highlighted in this study have important implications for climate. Upwelling deep water along the Antarctic continental shelf has driven an observed acceleration in basal ice shelf melt in recent decades (Cook et al., 2016). The three-dimensional pathways carrying deep water from the Atlantic, Indian and Pacific to the Antarctic continent described here provide a framework for understanding where relatively warm deep water is supplied to the Antarctic continental shelf and the origin of changes in the heat content of this water. Observations indicate that upwelling deep water preferentially reaches close to the Antarctic continent along the western Antarctic Peninsula (Fig. 3.1a), but further analysis of our model results are needed to determine the regionality of supply of deep water to the continental shelf in greater detail.

From our simulations, we find that the timescale for deep water in the 1000-3500 m depth range to travel from 30°S to the surface mixed layer is of the order of multiple decades to a century (Fig. 3.4). This upwelling timescale has implications

for the time taken for changes in the deep ocean to be relayed to the surface of the Southern Ocean where they can influence the atmosphere. For instance, the peak upwelling timescale (mode) from the three models for deep water to travel from 30°S in the Atlantic Ocean to the surface of the Southern Ocean ranges from 28 to 81 years. Chloroflourocarbon-based estimates of the timescale for water from deep water formation sites in the North Atlantic to first reach 20°S are on the order of 30 years (Rhein et al., 2015). This suggests a combined advective timescale from the northern North Atlantic to the Southern Ocean surface on the order of a century. This estimate is comparable to the time lag between abrupt climate changes in the Northern Hemisphere and Antarctica of 218$\pm$ 92 years and 208$\pm$ 96 years for warm and cold events, respectively, estimated from ice core records (WAIS Divide Project Members, 2015), which are likely propagated from the Northern Hemisphere to Antarctica via the ocean. Additionally, our estimates of Lagrangian particle-transport show that NADW dominates the total upwelling. This suggests that changes in the deep Atlantic may have a disproportionate impact on the deep water properties that reach the surface of the Southern Ocean, and thus have a greater influence on heat exchange with the atmosphere and cryosphere and on delivery of warm water to the Antarctic continental shelf (Armour et al., 2016).

Our result may have ramifications for the air-sea exchange of carbon dioxide, as variability in tracer uptake in the Southern Ocean is likely related to upwelling strength (Le Quéré et al., 2007; Lovenduski et al., 2008). The spatial patterns of where deep water enriched in natural carbon but lacking in anthropogenic carbon reaches the upper ocean (Fig. 3.6e and Figs 3.A6,3.A7) are highly localized, suggesting that carbon fluxes might also present localized patterns in relation to these upwelling hotspots, as suggested by the distribution of anthropogenic carbon uptake in an earlier iteration of SOSE (Ito et al., 2010). Further work is needed to determine the correspondence between the distribution of upwelling into the surface ocean shown here and surface observations, and

to what extent these upwelling patterns influence spatial distributions of carbon flux. The significant differences between the models in location of the deep water outcrops (Fig. 3.6d), in contrast with the strong agreement in the preferred locations of interior upwelling (Fig. 3.6a), emphasizes the importance of improving in situ observations of upwelling and carbon dioxide fluxes, which have high uncertainty due to sparse observations and large interannual variability (Landschützer et al., 2015). The spatially varying upwelling identified here means that Southern Ocean heat and carbon uptake estimates from sparse, ship-based observations are likely unreliable. New, year-round, float-based biogeochemical measurements are beginning to transform our knowledge of the Southern Ocean carbon cycle, and will allow quantitative validation of the importance of topographic hotspots in the natural and anthropogenic carbon budgets.

Climate change is predicted to drive a strengthening in Southern Hemisphere westerly winds (Swart and Fyfe, 2012), as has already been observed in recent decades (Marshall, 2003). This trend has led to a more energetic eddy field in the ACC (Hogg et al., 2015) and is expected to drive a further increase in EKE in the ACC in the future (Patara et al., 2016). Our finding that eddies play a key role in driving Southern Ocean upwelling indicates that upwelling rates are likely sensitive to wind-driven changes in the eddy field. More vigorous eddies in the ACC could increase the supply of carbon-rich deep waters to the sea surface, and hence may weaken the Southern Ocean carbon sink. However, more work is needed to uncover the response of the carbon sink to a change in the eddy field. Similarly, changes in the eddy field would likely also alter the supply of nutrients to the surface of the Southern Ocean, potentially altering the efficiency of the biological pump. Our results demonstrate that a deep understanding of the three-dimensional upwelling in the Southern Ocean is needed to determine the complex role of the Southern Ocean in the global heat, carbon and nutrient budgets.

3.4 Methods

Observations. Mapping of hydrographic properties on neutral density surfaces was carried out (Orsi and Whitworth, 2005) using high quality historical hydrographic data and the World Ocean Circulation Experiment (WOCE) observations of the 1990s. The maps in Fig. 3.1a and Fig. 3.A1 are derived from those in the WOCE Hydrographic Programme Southern Ocean atlas(Orsi and Whitworth, 2005), which used an objective mapping technique with elliptical search radii, with longer spatial scales following topographic contours. ACC fronts based on these hydrographic data are also shown in Fig. 3.A1 (Orsi et al., 1995).

Model simulations and state estimate. Offline Lagrangian analysis was performed in two global climate models (CM2.6 and CESM) and in the regional Southern Ocean State Estimate (SOSE).

CM2.6 is the high resolution version of the Geophysical Fluid Dynamics Laboratory's CM2-O coupled model suite (Griffies et al., 2015). It combines global nominal 1/10° resolution ocean and sea ice models with 50 km resolution atmosphere and land models. The ocean component is based on the MOM5 code, and employs no mesoscale eddy parameterization in the tracer equation. A year 1990 control simulation was used, with atmospheric CO_2 fixed at 355 ppm. CM2.6 is spun up for 84 years preceding the period used for analysis. Twelve years of 5-day averaged velocity fields were used for the Lagrangian analysis.

CESM is a high resolution coupled climate model with nominal 1/10° ocean and sea-ice resolution and 1/4° atmosphere and land resolution (Small et al., 2014). The ocean component uses the Parallel Ocean Program (POP2), with no mesoscale eddy parameterizations. A year 2000 control simulation was used, with atmospheric CO_2 fixed at 367 ppm. CESM is spun up for 80 years preceding the period used for analysis

here. Twenty years of monthly averaged velocity fields were used for the Lagrangian analysis.

The SOSE is a 1/6°, data-assimilating, ocean general circulation model based on the MITgcm, configured in a domain from 24.7°S to 78°S with an open northern boundary and a sea ice model (Mazloff et al., 2010). No mesoscale eddy parameterization is employed. Using software developed by the consortium for Estimating the Climate and Circulation of the Ocean (ECCO; `http://www.ecco-group.org`), the SOSE assimilates the majority of available observations using an adjoint method. For this study we used the SOSE iteration 100 solution, which has been validated against ocean and ice observations (Abernathey et al., 2016), and spans six years (2005-2010) with 1-day averaged velocity fields used for the Lagrangian analysis.

In addition to comparisons of the global model ocean and atmospheric states with observations, several papers specifically address the model representation of the ACC transport, Southern Ocean surface properties and overturning in CESM (Bishop et al., 2016), CM2.6 (Dufour et al., 2015; Morrison et al., 2016) and SOSE (Abernathey et al., 2016). A comparison of the time-mean volume meridional transport at 30°S in CESM, CM2.6 and SOSE shows reasonable agreement in the magnitude and spatial structure of volume transport (Fig. 3.2). The total southward transport across 30°S between 1000 m and 3500 m is 28.8, 22.7 and 32.9 Sv in the CESM, CM2.6 and SOSE, respectively; the portion that does not upwell south of 30°S could be entrained into abyssal water without first reaching the sea surface, or cross north of 30°S shallower than 1000 m. Estimated total southward transport from hydrographic observations in this depth range is a comparable 18 to 30 Sv dependent on the choice of layer, which also include northward transport; in isopycnal layers the maximized southward transport is order 42 Sv (Talley, 2008). The Southern Ocean upper overturning cell has similar structure in the three models (Fig. 3.3), but the abyssal overturning cell is significantly

weaker in CM2.6. The transports were calculated on potential density surfaces (referenced to 2000 m) online in CM2.6, using 30-day averaged output in CESM and on neutral density surfaces using daily averaged output in SOSE, which was remapped to approximate potential density surfaces (Abernathey et al., 2016).

The mixed layer depth in each model is calculated using an 0.03 kg m^{-3} density threshold (de Boyer Montégut et al., 2004). The upwelling pathways in all three models were found to be insensitive to the mixed layer definition (not shown). Mean eddy kinetic energy at 1000 m in each model was calculated from the 1-day averaged velocities in SOSE, 5-day averaged velocities in CM2.6 and 30-day averaged velocities in CESM. In this case 'eddies' are defined as deviations from the long-term time-averaged velocity field.

Lagrangian methods. The same particle release experiment was conducted offline with velocity output from each of the three models, using the Connectivity Modeling System(Paris et al., 2013) (CMS) in CM2.6 and CESM and Octopus (`http://github.com/jinbow/Octopus`) in SOSE. In each case, more than 2.5 million particles were released at 30°S in every grid cell between 1000 m and 3500 m depth. Particles were re-released at the same location every month for the duration of the model output velocities (6 years in SOSE, 12 years in CM2.6 and 20 years in CESM). The trajectories were integrated for a total of 200 years, looping through the model output in time such that the velocity fields return to the first time step once the end of the output has been reached (Van Sebille et al., 2013). To avoid unphysical upwelling that might occur as a result of small model drifts when looping velocity output, the particle depths are held constant during the looping time step. The time step for particle advection was 1 hour for the CMS experiments in CM2.6 and CESM, while for the Octopus experiments in SOSE the particle advection time step was 0.5 days. A 10-minute time step results in the same trajectories within a 100-day testing window because 1) the SOSE velocities are

saved as daily average and 2) a high order scheme (4th order Runge-Kutta) is used in the time integration. In Octopus, particles are numerically reflected at the sea surface and water-land boundaries. In CMS, an ad-hoc boundary condition enforcing no-flux and no-slip boundary conditions is imposed; however, 30% of released particles are lost to advection into topography within 200 years. It is unlikely that this loss significantly affected the upwelling pathways, as the particles lost to topography were strongly biased toward the deepest particles with relatively low transport that were initially released near topography at 30°S. However, it is possible that this difference in handling of particles at the boundary could have contributed to the relatively large upwelling particle-transport in SOSE, where no particles are lost at the boundaries.

There is no parameterization of small scale mixing used in the Lagrangian experiments, but a comparison in SOSE shows that upwelling pathways are relatively insensitive to the inclusion of a stochastic noise component to represent sub-grid scale diffusion (Fig. 3.A4).

After 200 years of particle advection, only particles that reached the surface mixed layer and remained south of 30°S were selected for analysis. Less than 5% of the total released particle trajectories fulfilled these criteria in all three simulations, leaving approximately 100,000 trajectories in each. Of the remaining 95% of particles released that did not upwell, approximately half of the particles are excluded because they had initial northward velocities and the majority of the remainder exit north of 30°S without upwelling, leaving <1.5% of particles south of 30°S that did not upwell into the mixed layer during the 200 year experiment. We only considered the portions of trajectories before particles reach the mixed layer. Pathways in Fig. 2 are insensitive to different mixed layer depth definitions or using a constant depth crossing of 200 m rather than mixed layer depth (data not shown).

It is common to use Lagrangian particle tracking to assess volume transports

between chosen sites in the ocean, by assigning a volume transport to each particle at its release (Blanke et al., 1999; Speich et al., 2001; Döös et al., 2008; Van Sebille et al., 2014; Thomas et al., 2015). Each particle was 'tagged' with the meridional volume transport (in Sverdrups) at its release location at 30°S by multiplying the meridional velocity by the area of the model grid cell at the particle release location. Because the model velocity fields are non-divergent, and a sufficient number of particles are released to allow for deformation of the flow, it is assumed that the transport carried by each particle is conserved over the length of the simulation (Blanke et al., 1999; Döös et al., 2008). This volume transport is then conserved along the trajectories until they reach the mixed layer, providing an estimate of the transport of upwelling deep water between 30°S and the mixed layer.

Particle transport weighting was used in Figs. 1, 4, 5 and 6, by summing the volume transports of each particle at each location, and normalizing by the total volume transport of all of the particles. Therefore, particles assigned with more transport initially have a larger contribution to the pathway distributions. Our spatial upwelling pathways are qualitatively unaffected by this transport weighting, although it does affect the relative timescales and strengths of different pathways. We refer to particle trajectories weighted by their initial transport at 30°S as 'particle-transport'. The accuracy of the resulting transport pathways depends on the number of particles deployed and complexity of the flow, so the accuracy of particle-transport pathways was tested by randomly halving the selection of particles and was found to be insensitive (Fig. 3.A5). Other recent experiments in eddy-resolving models show good agreement between Lagrangian transports and Eulerian transports on decadal timescales (Van Sebille et al., 2014).

Code availability SOSE is based on the MITgcm code framework, available at `http://mitgcm.org`. Code to run the CM2.6 experiment is available from `http://www.`

gfdl.noaa.gov/cm2-5-and-flor. The CMS, used for Lagrangian experiments with CESM and CM2.6, is an open-source Fortran toolbox available for download at https://github.com/beatrixparis/connectivity-modeling-system. The Octopus Lagrangian code, used with SOSE, is available at https://github.com/jinbow/Octopus. Analysis was completed using the open-source Python scientific stack (http://scipy.org). **Data availability** All data supporting this study are open and freely available. Hydrographic section data from the WOCE atlas are available at the NOAA National Centers for Environmental Information (https://www.ncei.noaa.gov/) and the CLIVAR and Carbon Hydrographic Data Office (http://cchdo.ucsd.edu). The model output from the CESM model is available through the Earth System Grid (earthsystemgrid.org). Output from CM2.6 used to generate figures in this paper are available from the corresponding author on reasonable request. SOSE Iteration 100 model output is available at http://sose.ucsd.edu.

3.5 Acknowledgements

V.T., L.D.T. and M.M. were supported by NSF OCE-1357072. A.K.M., H.F.D. and W.W. were supported by the RGCM program of the U.S. Department of Energy under Contract DE-SC0012457. J.L.S. acknowledges NSF's Southern Ocean Carbon and Climate Observations and Modeling project under NSF PLR-1425989, which partially supported L.D.T. and M.M. as well. C.O.D was supported by the National Aeronautics and Space Administration (NASA) under Award NNX14AL40G and by the Princeton Environmental Institute (PEI) Grand Challenge initiative. A.R.G. was supported by a Climate and Global Change Postdoctoral Fellowship from the National Oceanic and Atmospheric Administration (NOAA). S.M.G. acknowledges the ongoing support of NOAA/GFDL for high-end ocean and climate modeling activities. J.W. acknowledges

support from NSF OCE-1234473 and declare that this work was done as a private venture and not in the author's capacity as an employee of the Jet Propulsion Laboratory, California Institute of Technology. Computational resources for the Southern Ocean State Estimate were provided by NSF XSEDE resource grant OCE130007. Output from the ASD run of CESM was made available by J. Small (NCAR) and colleagues. We thank Alejandro Orsi for the gridded hydrographic observations, Stu Bishop for providing processed CESM output, and Ryan Abernathey, Haidi Chen and Nathaniel Tarshish for useful discussions on the manuscript. We thank the three anonymous reviewers for their very helpful comments that greatly improved the paper.

Chapter Three, in full, is a reprint of the material as it appears in Nature Communications. Tamsitt, V., H. Drake, A. K. Morrison, L. D. Talley, C. O. Dufour, A. R. Gray, S. M. Griffies, M. R. Mazloff, J. L. Sarmiento, J. Wang, and W. Weijer (2017). Spiraling pathways of global deep waters to the surface of the Southern Ocean. *Nature Communications*, 8, 172. The dissertation/thesis author was the primary investigator and author of this paper.

3.A Appendix

3.A.1 Supplementary Note 1

A motivation for this study is the set of maps in the WOCE Hydrographic Programme (WHP) atlas Volume 1: Southern Ocean (Orsi and Whitworth, 2005), with properties displayed along neutral density surfaces characterizing the Indian and Pacific Deep Waters (27.84 kg m^{-3}) and the North Atlantic Deep Water (28.05 kg m^{-3}). These maps were constructed by gridding hydrographic data from the National Oceanographic Data Center (NODC) and the WHP data collected in the 1990s. Fig. 3.1 and Fig. 3.A1 show properties along the latter neutral density surface, along with the four major ACC

fronts from one particular source (Orsi et al., 1995), bathymetry (single contour of 3000 m is superimposed), and the latitude band of Drake Passage, across which the deep waters must move in order to upwell to the sea surface. The gridded potential temperature shown in Fig. 3.A1b was replotted on the gridded depth from Fig. 3.A1a to produce the three-dimensional Fig. 3.1a, selecting only the region where gridded potential temperature is greater than 1.6 °C. From the full map, it is clear that water well above freezing reaches the Antarctic continent in the southeastern Pacific sector, as reviewed in the main text. The oxygen and nitrate maps show the inflow of low oxygen, high nutrient waters from the Pacific and Indian Oceans, and their spiral around Antarctica, rising to the sea surface as tracked using depth in Fig. 3.A1a.

Careful attention to the pathway of the warmest water and most extreme oxygen and nitrate in Fig. 3.A1 suggests that the cores of most extreme properties shift southward across the ACC fronts over or downstream of the major topographic obstacles, particularly noticeable at the Mid-Atlantic Ridge, Southwest Indian Ridge and the Pacific-Antarctic Ridge. However, there is not enough resolution in these fields to definitively show details of shifts across fronts, and upwelling of the core of properties associated with these obstacles is difficult to extract from the hydrographic observations. The numerical model analyses clearly show both of these. These maps also do not provide transports or time scales for the upwelling water, nor do they clearly show where the properties preferentially reach the sea surface. And finally they cannot show diapycnal transformation along the pathway of particles in the southeast spiral. The numerical models are used to explore all of these important aspects of the upwelling pathways and rates.

3.A.2 Supplementary Note 2

Three-dimensional upwelling pathways in CM2.6 from the Indian and Pacific basins are similar to the Atlantic, as they show narrow boundary pathways connecting 30°S to the ACC (Fig. 3.A2 and Videos 3.1-3.3). Figure 3.A1b and Figure 3.A2 show the cumulative pathways of deep water after 200 years of the particle-release experiment, so any information about the timescales of these pathways is not shown. To look at how the pathways evolve over time from the initial release of particles at 30°S, Videos 3.1-3.3 show the three-dimensional particle pathways at monthly snapshots from the time of release up to 50 years.

3.A.3 Supplementary Note 3

Unresolved sub-grid scale physics and dynamics and temporal averaging of the model velocities have an impact on particle trajectories. Thus we performed multiple sensitivity analyses using SOSE to assess the impact of varying model averaging timescales and Lagrangian methods on our results. First, the impact of adjusting the temporal averaging of model velocity data is compared for daily averaged, 5-day averaged and 30-day averaged velocities (Fig. 3.A3). SOSE velocities were saved as daily averaged output, but due to limited computer resources CM2.6 velocity output is only available as 5-day averages and CESM output is only available as 30-day averages. The maximum storage interval for accurate Lagrangian particle tracking depends on several factors related to dominant scales of length, velocity, model grid size and time. Experiments in the global 1/10° OFES model (the same resolution as CM2.6 and CESM used here) showed that connectivity transports and transit times (bulk measure of the flow) were relatively insensitive to time averaging on timescales of 3-days to 30-days (Qin et al., 2014). Here we compare the impact of time-averaging velocities on our particular

results, and we use SOSE because it has sufficiently high temporal resolution output available to test this (Fig. 3.A3), while CESM has only 30 day averaged output. We find that pathways are insensitive to averaging velocities on 5-day timescales compared to daily timescales north and within the ACC, but south of the ACC particle-transport is slightly higher in the 5-day averaged experiment than the daily averaged experiment (Fig. 3.A3b,d). The 30-day averaged experiment is also qualitatively similar to the daily and 5-day averaged experiment, but with somewhat less particle-transport in the ACC and more particle-transport south of the ACC than the experiment using daily averages (Fig. 3.A3c,e). It is important to note that only single-particle statistics are used in this analysis, which are expected to be mainly affected by the most energetic parts of the flow and thus are less sensitive to sampling frequency than other Lagrangian statistics. This could explain why the CESM results are similar to CM2.6 and SOSE even though the mesoscale is not well sampled in CESM. Further work is needed to fully interpret the differences in the experiments with different timescale averages, but the qualitative agreement of the upwelling pathways in SOSE with velocity averaging timescales up to 30-days suggest that our analysis of 30-day averaged velocities in CESM is justified.

Second, for some applications it is useful to add stochastic noise to trajectories with the aim of parameterizing diffusion by unresolved eddy motions that are absent in the explicitly resolved eddy field. Because the models used here are eddy-resolving or eddy-permitting, we have chosen not to include stochastic noise in the trajectory motions. To test whether the inclusion of stochastic noise significantly impacts our results, we repeated the experiment in SOSE with the addition of a random walk scheme. An additional displacement is added to particles at each time step by implementing the random number generator algorithm described in Kinderman and Monahan (1977) with zero mean and unit variance and a horizontal diffusivity of 25 $m^2\ s^{-1}$ and a vertical diffusivity of $1x10^{-5}\ m^2\ s^{-1}$. We show in Figure 3.A4 that the resulting pathways do not

change significantly with the inclusion of diffusion. With diffusion, there is slightly less particle-transport that travels close to the Antarctic continent and slightly less particle-transport following the Agulhas Current southward from 30°S, and a very slight increase in particle-transport within the ACC. There are several limitations to this comparison that are important to note. First, the stochastic noise we added to the trajectories is unbiased (positive and negative displacements are equally probable), which we know is not true in reality. Secondly, there are important sub-mesoscale advection and mixing processes not resolved in the models that are not parameterized. We acknowledge these limitations, and while the comparison in Figure 3.A4 is a first step toward determining the impact of mixing on particle trajectories, further work is needed to represent mixing processes more realistically.

Finally, sufficiently large numbers of particle trajectories are important to accurately represent the volume transport and provide robust statistics. We test the sensitivity of the particle pathways to the number of particles released by halving the number of particle trajectories used in the pathway analysis in SOSE (Fig. 3.A5). The comparison shows that the upwelling pathways are insensitive to halving the number of particles, indicating that we have released sufficient numbers of particles to capture the spatial structure of the upwelling pathways.

3.A.4 Supplementary Note 4

Upwelling across the 1000 m depth surface in CESM and SOSE is similar to that in CM2.6 (Figs. 3.A6a and 3.A7a). Note that because CESM output is 30-day averages, the eddy kinetic energy (contoured in blue in Fig. 3.A6a) does not include transient mesoscale variability on timescales less than 30-days. However, the spatial patterns of high EKE in CESM are very similar to those in CM2.6, which includes variability between 5-days and 30-days.

The particle-transport crossing the 200 m depth surface varies more across models than the 1000 m depth crossings (Figs. 3.A6b and 3.A7b) as it is influenced by mixed layer and upper ocean processes, which vary across the models.

Table 3.1: Timescales of upwelling in each model and each ocean basin. The mode is determined by first smoothing the transit time distribution, then finding the maximum value in the distribution.

Model		Median	Mean	Mode
CESM	Total	70	79	41
	Atlantic	61	72	48
	Indian	68	78	50
	Pacific	58	68	41
CM2.6	Total	62	72	28
	Atlantic	49	61	28
	Indian	68	78	48
	Pacific	47	60	22
SOSE	Total	92	96	81
	Atlantic	89	96	82
	Indian	76	82	29
	Pacific	109	111	93

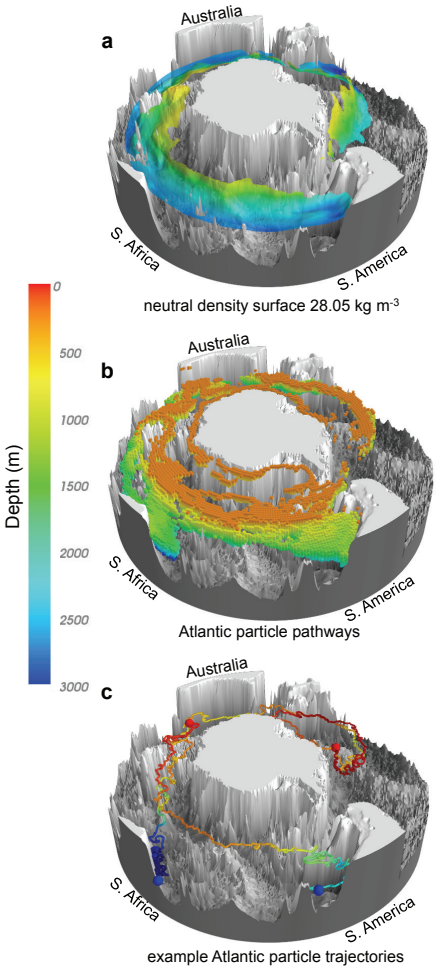

Figure 3.1: The three dimensional upward spiral of North Atlantic Deep Water through the Southern Ocean. (a) Observed warm water (>1.6°C) on the 28.05 kg m^{-3} neutral density surface from hydrographic observations (Orsi and Whitworth, 2005), south of 40°S, colored by depth (m). The isoneutral surface is masked in regions with potential temperature below 1.6°C. 1/4° ocean bathymetry (Smith and Sandwell, 1997) is shown in gray. (b) Modeled (CM2.6) particle pathways from the Atlantic Ocean, with particles released in the depth range 1000-3500 m along 30° S. Colored boxes mark 1° latitude x 1° longitude x 100 m depth grid boxes visited by more than 3.5% of the total upwelling particle-transport from release at 30°S to the mixed layer. Boxes are colored by depth, similar to (a). (c) Two example upwelling particle trajectories from CM2.6, one originating from the western Atlantic and the other from the eastern Atlantic. Trajectories are colored by depth as in (a) and (b), blue spheres show the particle release locations and red spheres show the location where the particles reach the mixed layer. Three-dimensional maps were produced using Python and Mayavi (Ramachandran and Varoquaux, 2011).

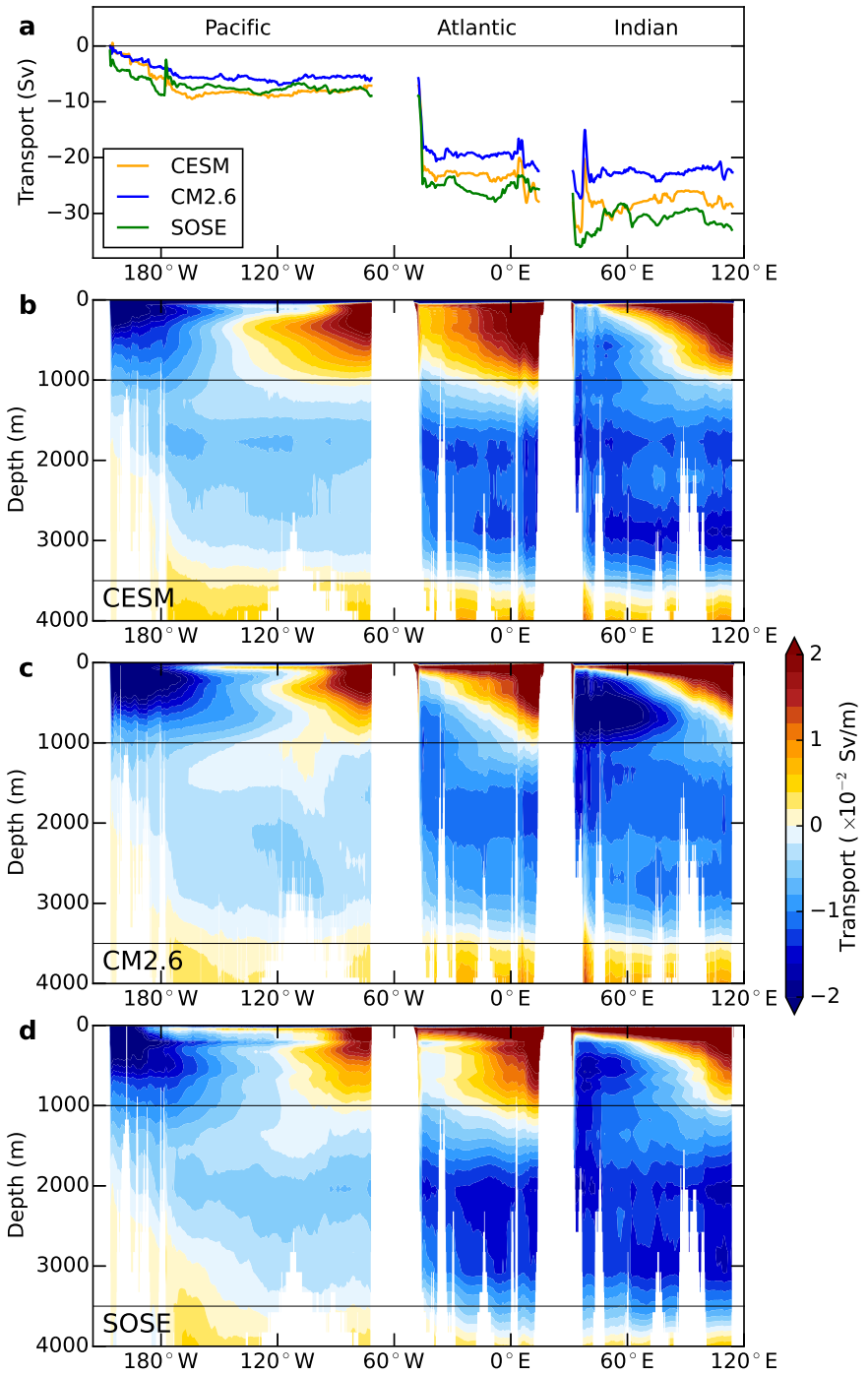

Figure 3.2: Model comparison of volume transports at 30°S. a) shows the volume transport in Sverdrups integrated over the depth range 1000-3500 m, b), c) and d) show the Eastward cumulative integrals of the time average meridional transport in Sv m^{-1} at 30°S in CESM, CM2.6 and SOSE, respectively. The transports in the b)-d) are normalized by the model vertical grid thicknesses.

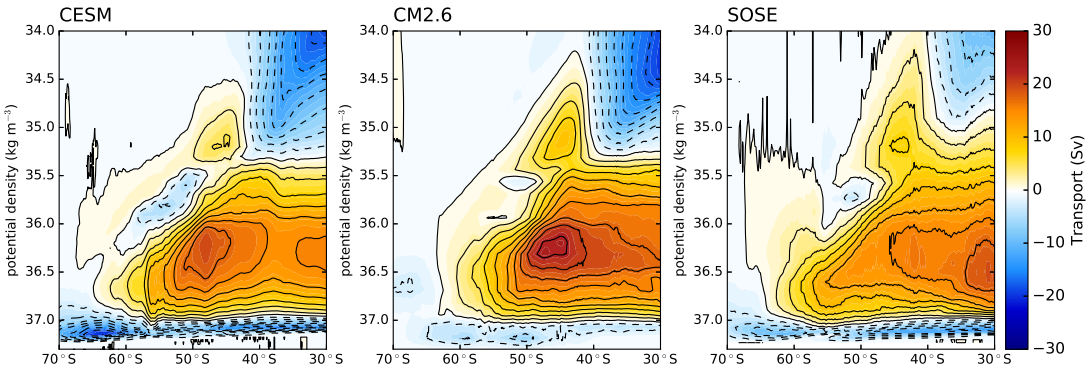

Figure 3.3: Model comparison of Southern Ocean zonally averaged circulation. Meridional overturning streamfunction (Sverdrups) in a) CESM, b) CM2.6 and c) SOSE. Solid and dashed contours represent positive and negative transport, respectively, with an interval of 2.5 Sv.

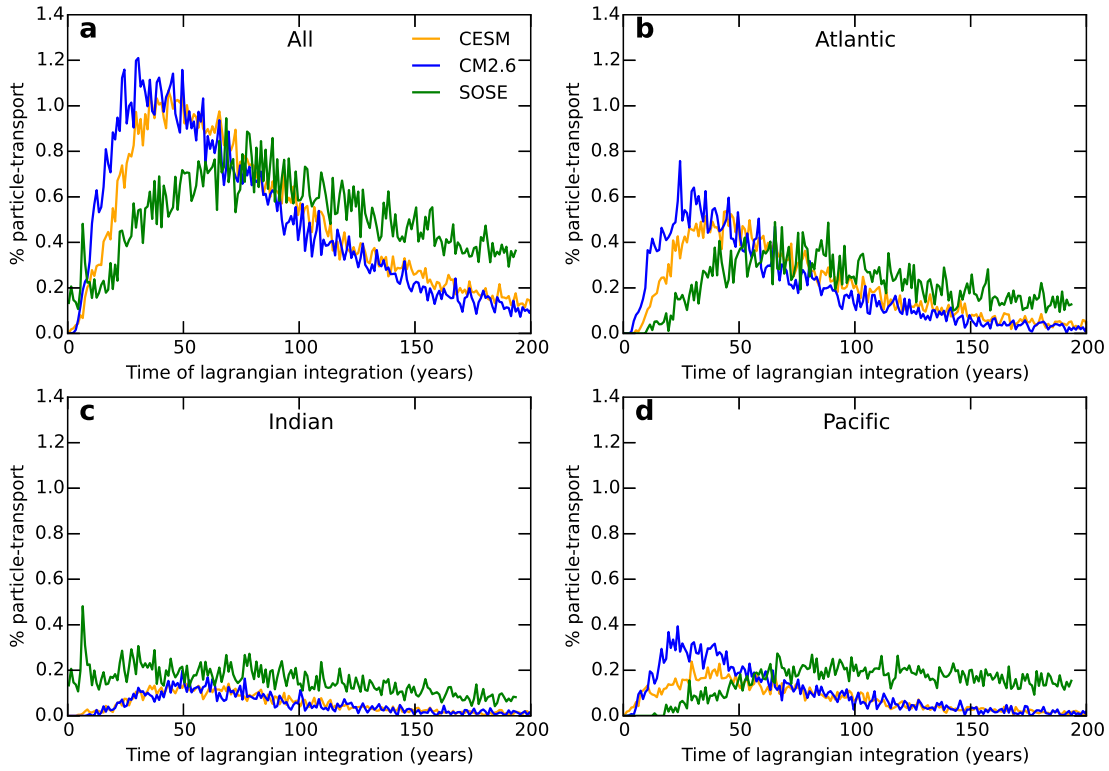

Figure 3.4: Particle upwelling timescales. Transit time distribution for particle-transport from 30°S to the mixed layer in the three models for particles originating in a) all basins, b) the Atlantic, c) the Indian and d) the Pacific.

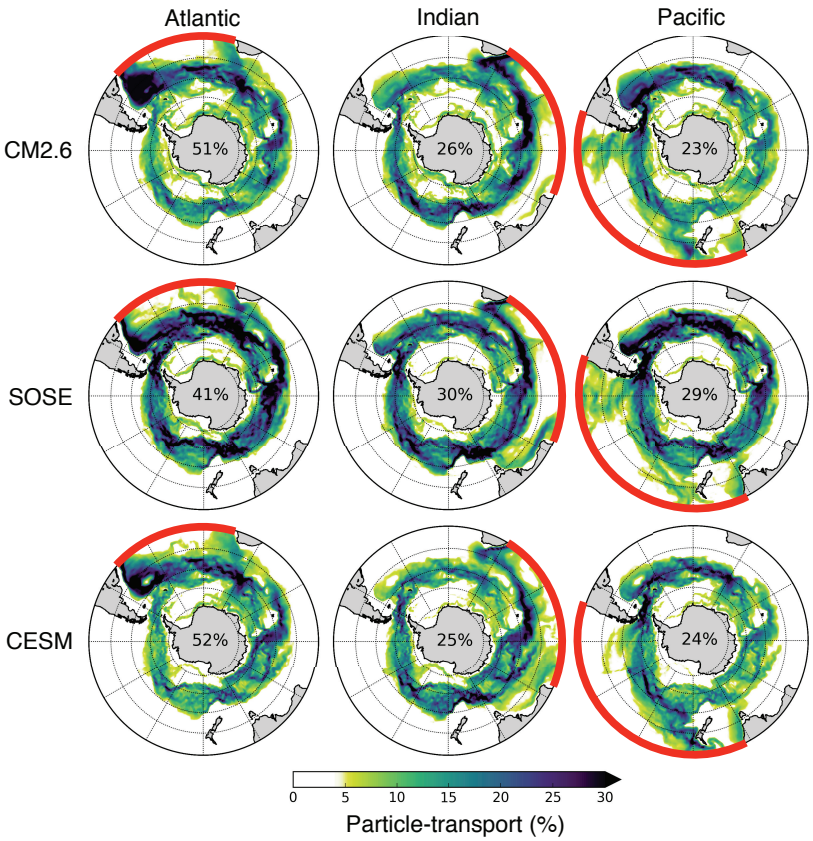

Figure 3.5: Particle pathways from 30°S to the mixed layer. Maps of the percent of total basin upwelling particle-transport visiting each 1° latitude x 1° longitude grid column at some time during the 200 year experiment from release at 30°S and before reaching the surface mixed layer for CM2.6, SOSE, and CESM. The percentages of particle-transports originating in the Atlantic, Indian and Pacific (release locations at 30°S marked in red) are shown separately, normalized by the total upwelling particle-transport originating in each basin. The percentages in the center of each panel indicate the relative contribution of the Atlantic, Indian and Pacific to the total upwelling particle-transport in each model.

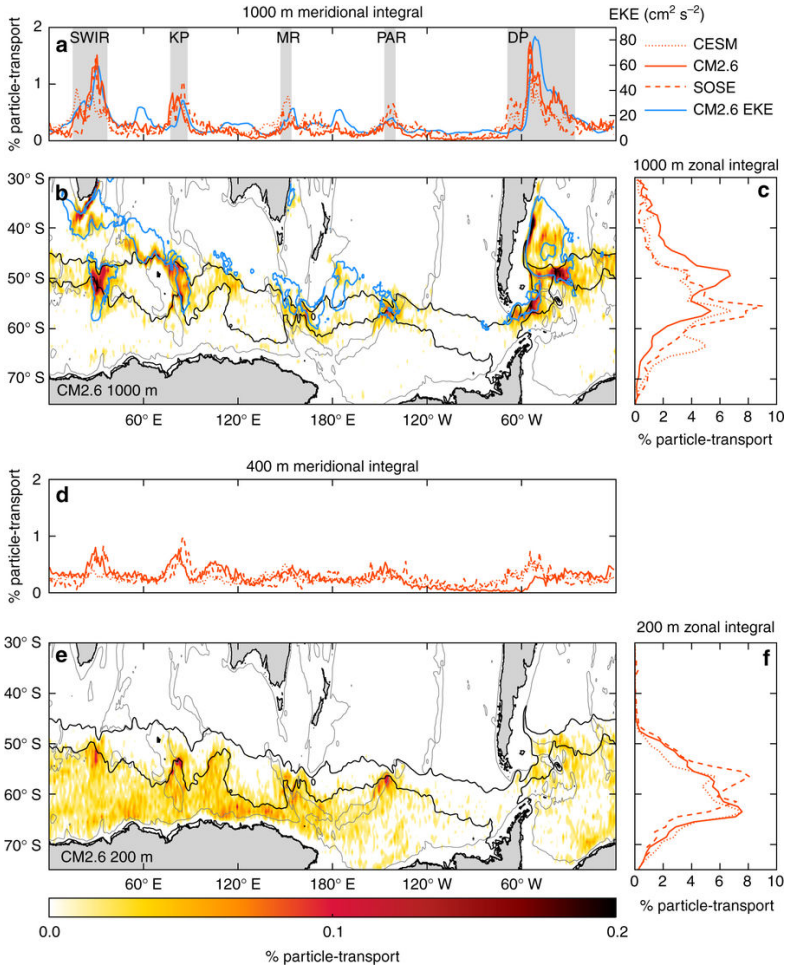

Figure 3.6: Upwelling of particles across depth horizons. (a) Percent of total upwelling particle-transport crossing 1000 m (1000 m is chosen because it is representative of upwelling in the interior and lies above major topographic features) as a function of longitude, integrated across all latitudes for all three models; the blue line shows the mean Eddy Kinetic Energy (EKE) at 1000 m in CM2.6 averaged between 30°S and Antarctica at each longitude; grey shaded bars show the location of the 5 major topographic upwelling hotspots: the Southwest Indian Ridge (SWIR), Kerguelen Plateau (KP), Macquarie Ridge (MR), Pacific-Antarctic Ridge (PAR) and Drake Passage (DP). (b) Percent of particle-transport crossing 1000 m in each 1° latitude x 1° longitude grid box between release at 30° S and the mixed layer in CM2.6. Blue contours indicate regions where the mean EKE at 1000 m in CM2.6 is higher than 75 cm^2 s^{-2}. (c) Percent of particle-transport crossing 1000 m depth as a function of latitude, integrated across all longitudes for all three models. (d) Same as (a) for 200 m, without EKE contours, (e) same as (b) for 200 m without EKE contours, and (f) same as (c) for 200 m. In all panels, we select the location at which particles cross depth surfaces for the final time along their trajectories. Qualitatively similar results are obtained from selecting first-crossing locations. Black contours in (b) and (e) are the outermost closed contours through Drake Passage of mean sea surface height in CM2.6, representing the path of the Antarctic Circumpolar Current.

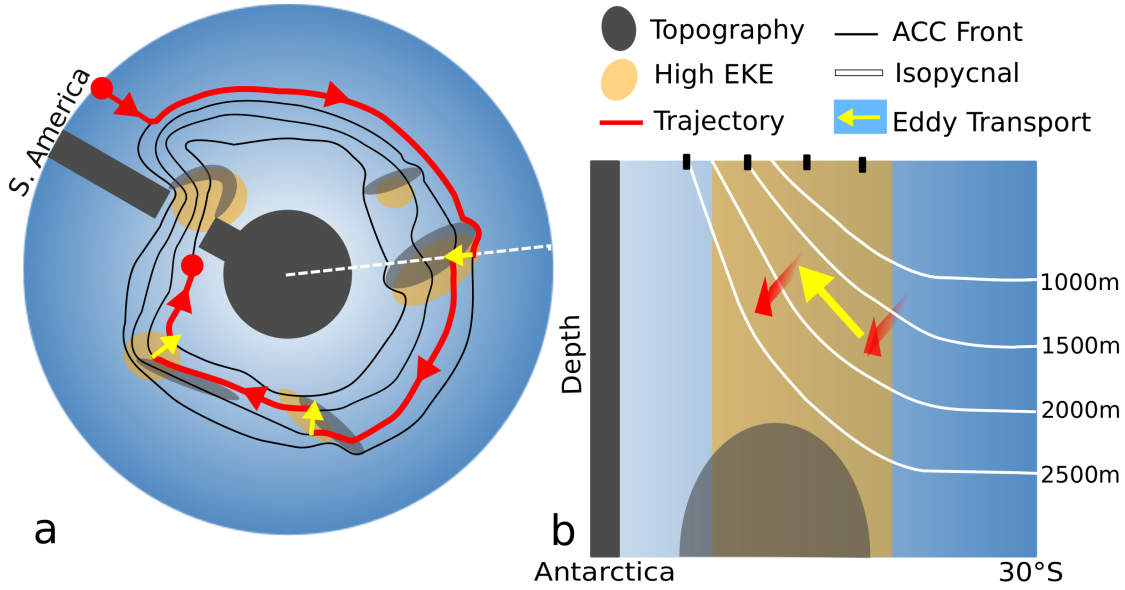

Figure 3.7: Idealized schematic illustrating the effect of eddy advection at topographic hotspots on upwelling pathways. (a) An idealized particle trajectory (red) follows time-mean Antarctic Circumpolar Current (ACC) streamlines (black) that flow southeastward around Antarctica from east of Drake Passage (blue surface indicating the particles' isopycnal surface, lighter color indicating shallower depths). The trajectory crosses streamlines and upwells (yellow arrows) in regions of high Eddy Kinetic Energy (EKE, yellow shading) at major topographic features (gray shading). This creates a superimposed southward/upward spiral as the particles shift southward and upward each time they encounter a region of high EKE. (b) A two-dimensional vertical cross-section of the Southern Ocean from Antarctica to 30°S, indicated by the white dashed line in (a). White lines show idealized isopycnal layers shoaling and thinning toward the South. The red arrows show the trajectory entering the high EKE region associated with topography along the northernmost ACC front and exiting the region, shallower and further south (front positions indicated by dotted lines).

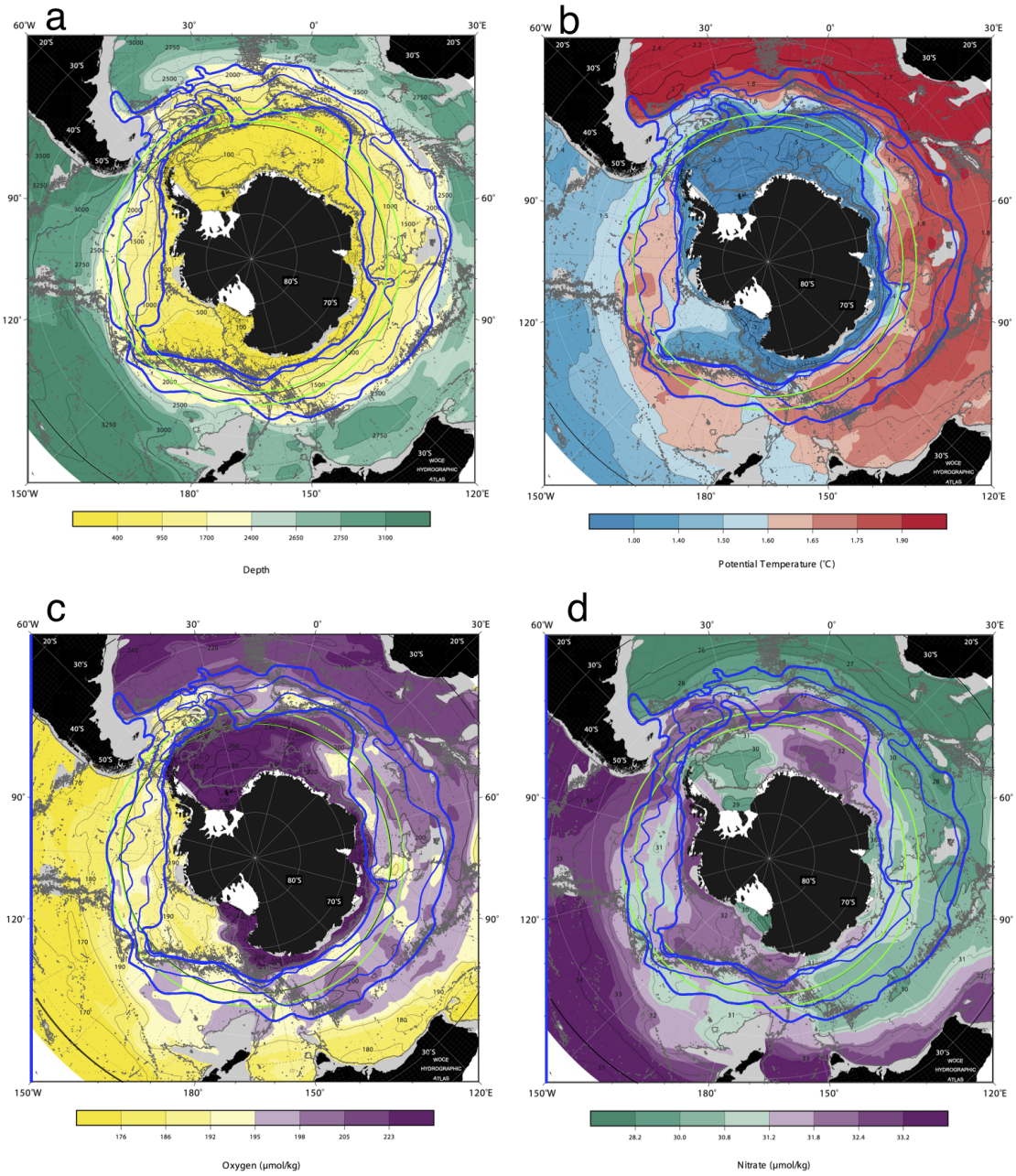

Figure 3.A1: Properties of the neutral density surface 28.05 kg m^{-3}, from the WOCE Hydrographic Programme Atlas Volume 1: Southern Ocean (Orsi and Whitworth, 2005):(a) Depth (m), (b) potential temperature (°C), (c) oxygen (umol/kg), (d) nitrate (umol/kg). Superimposed on the WHP maps are the 3000 m bathymetric contour (gray), ACC fronts (Orsi et al., 1995) (blue), and the latitude range of Drake Passage (green).

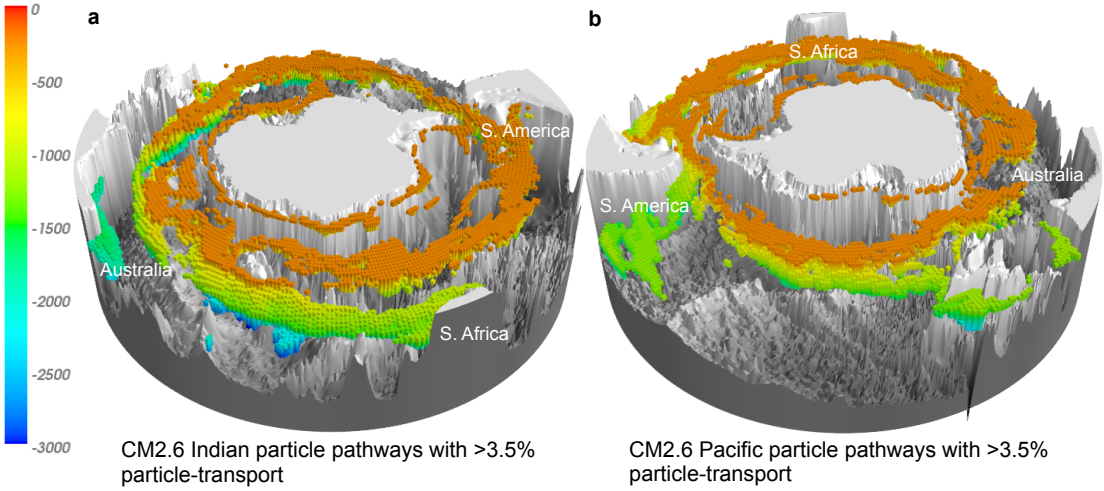

Figure 3.A2: Particle pathways in CM2.6 as in Figure 1b but for particles that originate in the (a) Indian Ocean and (b) Pacific Ocean. Particles leave the Indian Ocean along two pathways: in the Agulhas Return Current east of Africa and in a deeper tongue along the Australian south coast. Particles leave the Pacific Ocean along three pathways: from the Tasman Sea, from the New Zealand region, and between the East Pacific Rise and South America.

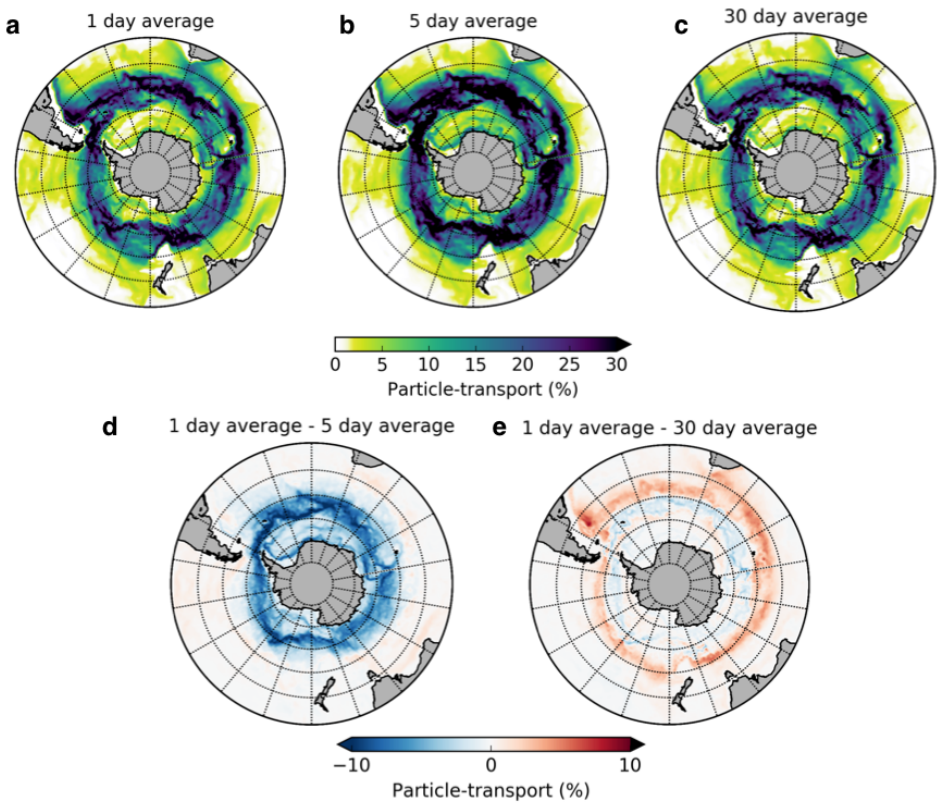

Figure 3.A3: Sensitivity of pathways in SOSE to velocity averaging. Percent of particle-transport visiting each 1° latitude x 1° longitude grid column from release at 30°S and before reaching the surface mixed layer for (a) SOSE daily averaged velocity output, (b) SOSE 5-day averaged velocity output, (c) SOSE 30-day averaged velocity output, (d) daily averaged velocities minus 5-day averaged velocities (a-b) and (e) daily averaged velocities minus 30-day averaged velocities (a-c). Note that the colorbar axis limits in panels (d) and (e) differ from (a), (b) and (c).

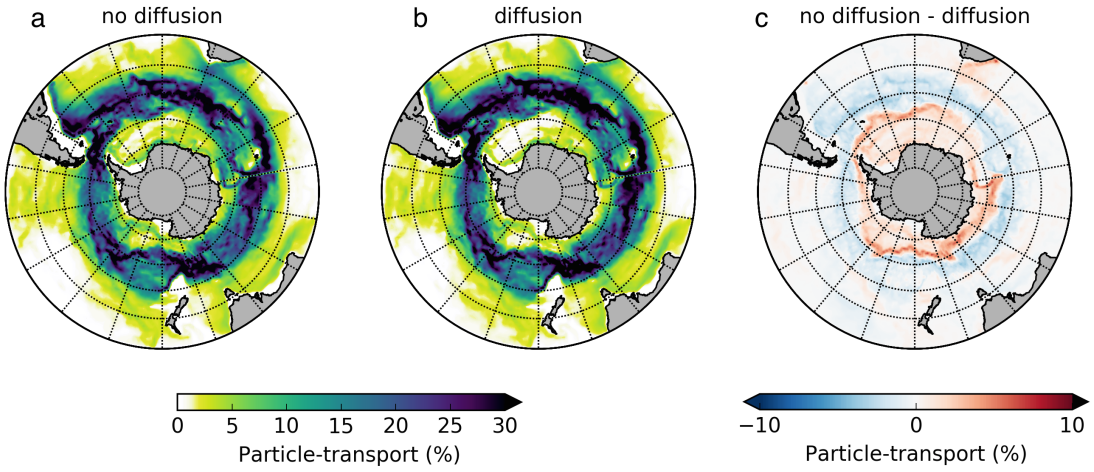

Figure 3.A4: Sensitivity of pathways in SOSE to inclusion of a stochastic noise component in the trajectory motion to represent sub-grid scale diffusion. Percent of particle-transport visiting each 1° latitude x 1° longitude grid column from release at 30°S and before reaching the surface mixed layer for (a) no diffusion, (b) with diffusion, and (c) no diffusion minus with diffusion (a-b).

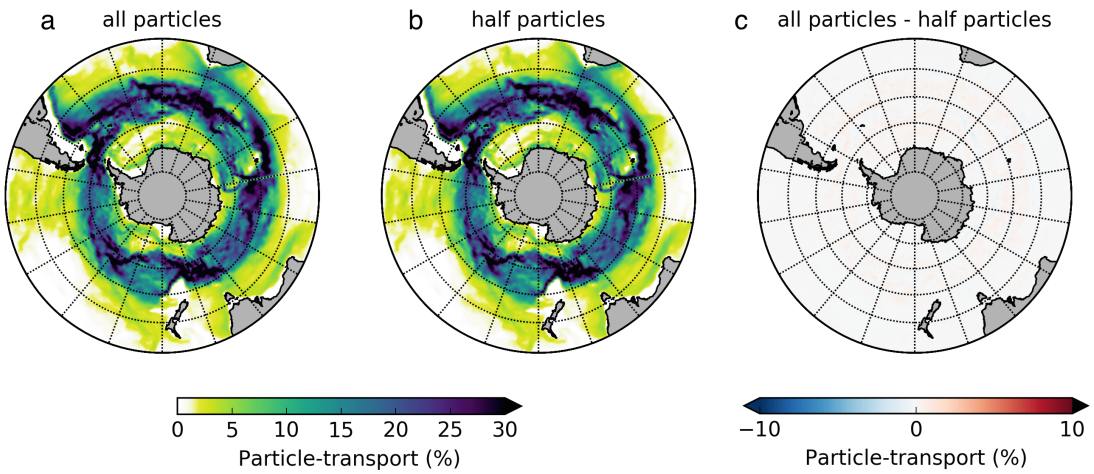

Figure 3.A5: Sensitivity of pathways in SOSE to halving the number of particles included in the pathway calculation. Percent of particle-transport visiting each 1° latitude x 1° longitude grid column from release at 30°S and before reaching the surface mixed layer for (a) all of the upwelled particle trajectories, (b) half of the total upwelled particle trajectories, and (c) all particle trajectories minus half of the particle trajectories (a-b).

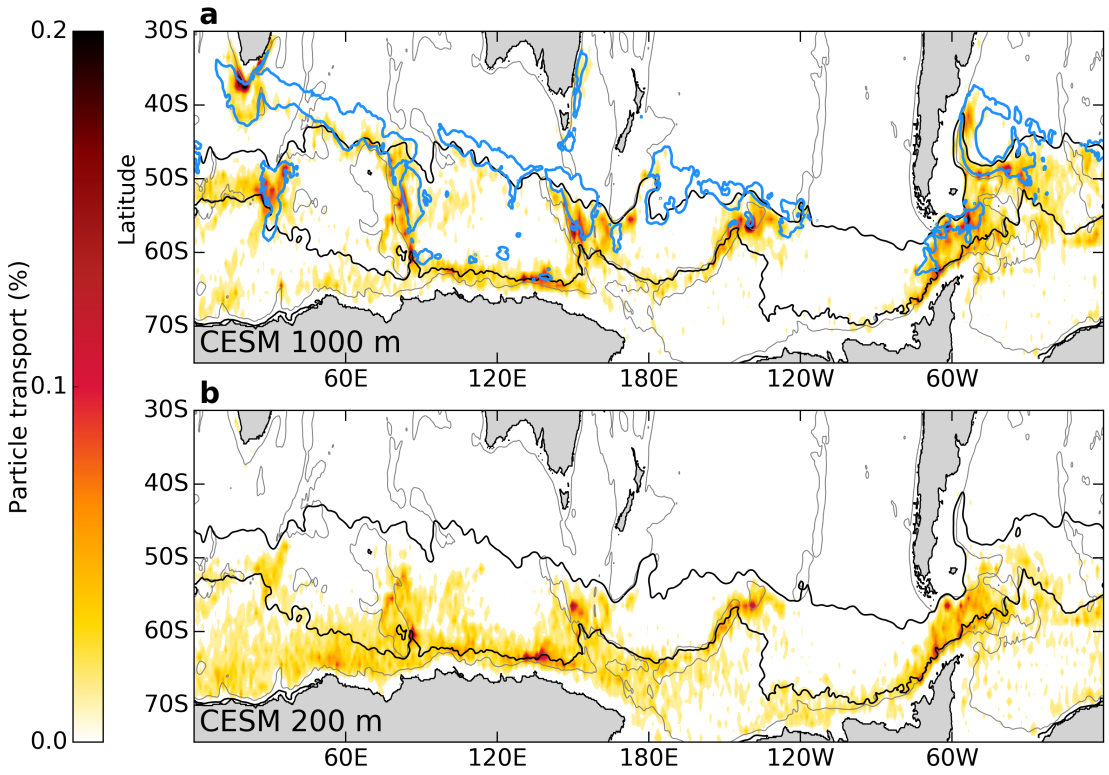

Figure 3.A6: Upwelling of particles across depth horizons. (a) Percent of particle-transport crossing 1000 m in each 1° latitude x 1° longitude grid box between release at 30° S and the mixed layer in CESM and (b) same as (a) for 200 m. In all panels, we select the location at which particles cross depth surfaces for the final time along their trajectories. Qualitatively similar results are obtained from selecting first crossing locations. Black contours are the outermost closed contours through Drake Passage of mean sea surface height in CESM, representing the path of the ACC. Blue contours in a) indicate regions where the eddy kinetic energy at 1000 m in CESM is higher than 75 cm^2s^{-2}.

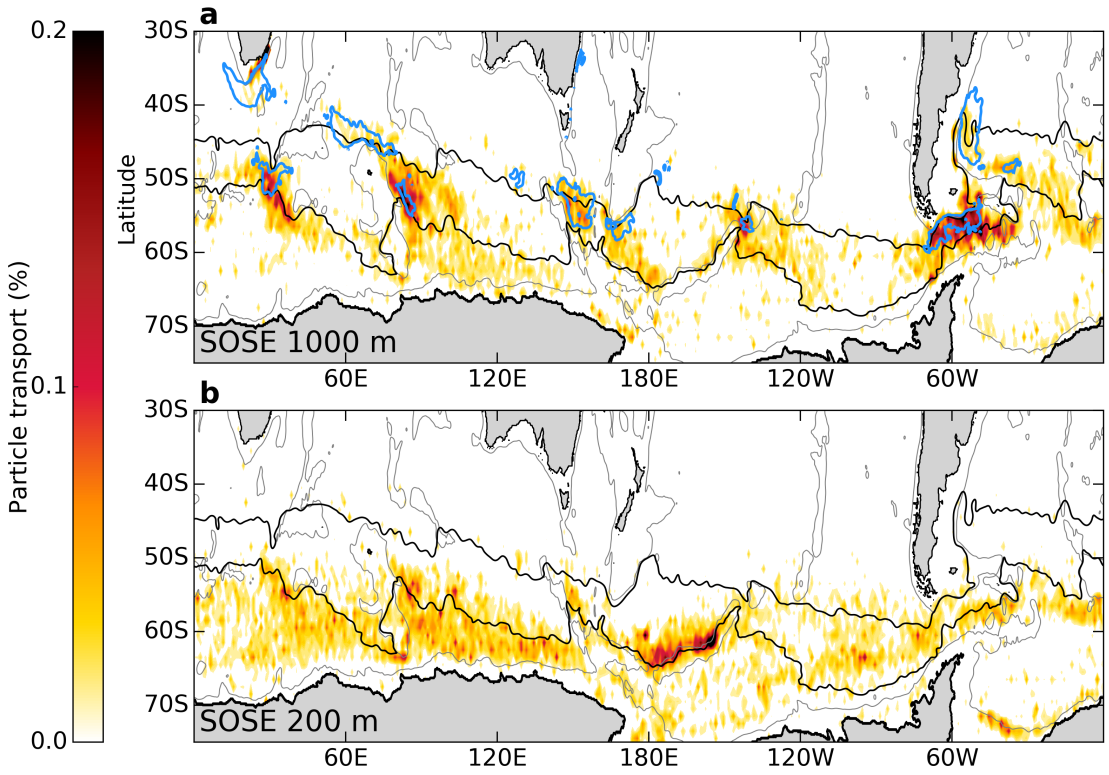

Figure 3.A7: Upwelling of particles across depth horizons. (a) Percent of particle-transport crossing 1000 m in each 1° latitude x 1° longitude grid box between release at 30° S and the mixed layer in SOSE and (b) same as a) for 200 m. In all panels, we select the location at which particles cross depth surfaces for the final time along their trajectories. Qualitatively similar results are obtained from selecting first crossing locations. Black contours are the outermost closed contours through Drake Passage of mean sea surface height in SOSE, representing the path of the ACC. Blue contours in (a) indicate regions where the eddy kinetic energy at 1000 m in SOSE is higher than 75 $cm^2 s^{-2}$.

Video 3.1: Deep water upwelling pathways from the Atlantic Ocean. Cumulative modeled (CM2.6) particle pathways for the first 50 years of the experiment from the Atlantic Ocean, with particles released in the depth range 1000-3500 m along 30°S. At each timestep, colored boxes mark 1° latitude x 1° longitude x 100 m depth grid boxes visited by more than 2.25% of the total upwelling particle-transport from release at 30°S to the current timestep. Boxes are colored by depth.

Video 3.2: Deep water upwelling pathways from the Indian Ocean. Cumulative modeled (CM2.6) particle pathways for the first 50 years of the experiment from the Indian Ocean, with particles released in the depth range 1000-3500 m along 30°S. At each timestep, colored boxes mark 1° latitude x 1° longitude x 100 m depth grid boxes visited by more than 2.25% of the total upwelling particle-transport from release at 30°S to the current timestep. Boxes are colored by depth.

Video 3.3: Deep water upwelling pathways from the Pacific Ocean. Cumulative modeled (CM2.6) particle pathways for the first 50 years of the experiment from the Pacific Ocean, with particles released in the depth range 1000-3500 m along 30°S. At each timestep, colored boxes mark 1° latitude x 1° longitude x 100 m depth grid boxes visited by more than 2.25% of the total upwelling particle-transport from release at 30°S to the current timestep. Boxes are colored by depth.

Chapter 4

Transformation of deep water masses along Lagrangian upwelling pathways in the Southern Ocean

Keypoints

- Upwelling of deep water is largely isopycnal in the Southern Ocean interior even at topographic upwelling hotspots
- Atlantic and Indian Deep Waters cool and freshen significantly along interior isopycnals, homogenizing deep water
- Significant transformation to lighter densities occurs below the mixed layer due to mixing with fresher surface waters

Abstract

Upwelling of northern deep waters in the Southern Ocean is fundamentally important for the closure of the global meridional overturning circulation and delivers carbon and nutrient-rich deep waters to the sea surface. We quantify water mass trans-

formation along upwelling pathways originating in the Atlantic, Indian and Pacific and ending at the surface of the Southern Ocean using Lagrangian trajectories in an eddy-permitting ocean state estimate. Recent related work shows that upwelling in the interior below about 400 m depth is localized at hotspots associated with major topographic features in the path of the Antarctic Circumpolar Current, while upwelling through the surface layer is more broadly distributed. In the ocean interior upwelling is largely isopycnal; Atlantic and to a lesser extent Indian Deep Waters cool and freshen while Pacific Deep waters are more stable, leading to a homogenization of water mass properties. As upwelling water approaches the mixed layer, there is net strong transformation toward lighter densities due to mixing of freshwater, but there is a divergence in the density distribution as Upper Circumpolar Deep Water tends become lighter and dense Lower Circumpolar Deep Water tends to become denser. The spatial distribution of transformation shows more rapid transformation at eddy hotspots associated with major topography where density gradients are enhanced; however, the majority of cumulative density change along trajectories is achieved by background mixing. We compare the Lagrangian analysis to diagnosed Eulerian water mass transformation to attribute the mechanisms leading to the observed transformation.

4.1 Introduction

Eighty percent of the World Ocean deep water is thought to return to the surface in the Southern Ocean (Talley, 2013a; Lumpkin and Speer, 2007). This upwelling of deep water plays an integral role in the global ocean uptake and redistribution of heat, carbon and nutrients (Frölicher et al., 2015; Sarmiento et al., 2004). Additionally, the upwelling of relatively warm deep water in the Southern Ocean has been driving the recent accelerated mass loss of Antarctic ice sheets (Cook et al., 2016). Early theories

of the global ocean overturning proposed that diapycnal mixing in the ocean interior was necessary to convert dense water formed at high latitudes to lighter surface waters (Munk, 1966; Munk and Wunsch, 1998), but direct measurements of mixing suggest that ocean mixing in the open ocean interior is an order of magnitude too small (Waterhouse et al., 2014). An alternative mechanism for returning deep water to the ocean surface with minimal mixing has emerged, via wind-driven upwelling along steeply tilted isopycnals in the Southern Ocean in the upper 2000 m(Toggweiler and Samuels, 1998; Sloyan and Rintoul, 2001b), while below this dipaycnal mixing is key for upwelling of abyssal waters. Recent observational studies indicate that the reality lies somewhere between the no-mixing limit and upwelling driven entirely by diapycnal mixing (Watson et al., 2013; Katsumata et al., 2013), but the role of mixing in the upwelling of deep water in the Southern Ocean remains poorly constrained.

Southern Ocean circulation is unique due to the lack of meridional boundaries at the latitudes of Drake Passage, enabling the circumpolar flowing Antarctic Circumpolar Current (ACC), linking the major ocean basins and allowing inter-basin exchange of properties. Steeply tilted isopycnals facilitate isopycnal upwelling of Circumpolar Deep Water (CDW) to the surface of the Southern Ocean, where it is directly modified by surface buoyancy fluxes. Theoretical modeling shows that a strong adiabatic overturning cell in the Southern Ocean is possible with isopycnals outcropping in both hemispheres and negligible interior diapycnal mixing; all diapycnal processes in this paradigm occur within the ocean's surface layer (Wolfe and Cessi, 2011).

However, observational studies suggest that the interior ocean mixing is an important component of the Southern Ocean meridional overturning circulation (Sloyan and Rintoul, 2001b; Naveira Garabato et al., 2004; Katsumata et al., 2013; Naveira Garabato et al., 2016). Near-bottom mixing in hotspots over rough seafloor topography (Ledwell et al., 2000; Polzin, 1997) can accomplish upwelling of the denser Lower

Circumpolar Deep Water (LCDW) to lighter Upper Circumpolar Deep Water (UCDW). Additionally, some LCDW density classes outcrop along the Antarctic continental slope rather than at the surface, and thus intense mixing in the bottom boundary layer facilitates transformation of these density classes to lighter water masses (Ruan et al., 2017). However, most of this bottom boundary layer mixing occurs within 1000 m of the bottom (Naveira Garabato et al., 2004; St. Laurent et al., 2012; Waterhouse et al., 2014), so away from the continental slope and shallow topographic features, it is not clear how important mixing is in upwelling of deep water in the 1000 m-2000 m depth range (Toggweiler and Samuels, 1998). Recent analysis of repeat observations across Drake Passage indicates that diapycnal mixing sustains the overturning in the upper 1000 m and in the 1000 m-2000 m above the seafloor, while in between, isopycnal stirring dominates in the Antarctic Intermediate Water and Upper Circumpolar Deep Water (UCDW) density classes (Naveira Garabato et al., 2016; Mashayek et al., 2017).

While there are many observations characterizing local episodes of intense turbulent mixing at rough topography, these measurements are sparse and infrequent in time, making it difficult to scale this to the integrated diapycnal mixing that affects the large scale overturning. Tracer release experiments are suited for addressing this question, but to date these efforts have been confined to regional studies, which are then extrapolated to the circumpolar Southern Ocean (Watson et al., 2013; Mashayek et al., 2017). Additionally, while there is evidence that diapycnal mixing in the interior of the Southern Ocean is elevated in hotspots associated with topography (Naveira Garabato et al., 2016; Watson et al., 2013; Ruan et al., 2017), these hotspots make up a relatively small fraction of the total volume of the deep Southern Ocean. Therefore, for an upwelling deep water parcel, it is not well understood how mixing at these hotspots contributes to the integrated density change along the path from the deep ocean to the surface. There are several different approaches applied to estimating regional mixing

using finescale parameterizations (Kunze et al., 2006) and inverse methods (Zika et al., 2010). To date there are multiple globally constrained estimates of the contribution of mixing to the overturning circulation, including inverse methods (Ganachaud and Wunsch, 2000; Sloyan and Rintoul, 2001b; Groeskamp et al., 2017) and finescale parameterizations from float profiles (Whalen et al., 2012). In addition to these methods, Lagrangian experiments in ocean general circulation models and state estimates can provide a complimentary perspective to the role of mixing in upwelling because of the ability to isolate large-scale density modification along upwelling deep water pathways (Döös et al., 2008; Iudicone et al., 2008a).

Recent Lagrangian model analyses show that this upwelling is spatially non-homogeneous and is enhanced at hotspots associated with major topographic features (Tamsitt et al., 2017). Using Lagrangian particle tracking in three eddying ocean models, Tamsitt et al. (2017) traced pathways of deep water from between 1000 m and 3500 m depth at 30°S in the Atlantic, Indian and Pacific to the surface of the Southern Ocean. Upwelling water followed narrow pathways along each ocean boundary to the ACC, before spiraling upward and southward in the ACC (Fig. 4.1a,b,c). Tamsitt et al. (2017) found that upwelling of deep waters in the interior (shown at 1000 m depth, which is representative of the interior up to 500 m depth) is concentrated in high EKE regions at or downstream of topography (Fig. 4.1) and hypothesize that this concentrated upwelling is due to vigorous eddy activity facilitating enhanced cross-frontal exchange, carrying water southward and upward along tilted isopycnals. However, the role of diapycnal mixing in these upwelling pathways, particularly at the topographic upwelling hotspots, was not investigated.

In this work, building on Tamsitt et al. (2017), we employ an eddy-permitting ocean state estimate to address how deep water transforms along Southern Ocean interior upwelling pathways, and where diapycnal mixing processes are important along

these pathways. We use a Lagrangian particle tracking approach to quantify the density changes along these pathways and determine where significant water mass transformation occurs due to diapycnal mixing in the ocean interior, removed from the strong influence of surface buoyancy fluxes. This Lagrangian approach is powerful because it is possible to track the cumulative effect of interior mixing on the density of a water mass from its deep water source to the surface, along Lagrangian trajectories. Additionally, we quantify temperature and salinity modifications individually to differentiate between isopycnal water mass modification and diapycnal mixing processes. We quantify the contribution from diapycnal mixing in upwelling hotspots associated with topography to the total diapycnal change. However, since some interior upwelling happens close to ridges and plateaus, elevated bottom mixing could be an important factor that is not included in the model analyzed here, and so we cannot evaluate its potential to increase diapycnal change in these locations. Finally, we relate Lagrangian density changes in the interior to diagnosed Eulerian diapycnal velocities in the interior to gain insight into the processes driving water mass transformation.

In section 2 we describe the model and Lagrangian and Eulerian methods of quantifying water mass transformation. The total transformation along Lagrangian trajectories are discussed in section 3.1, the contributions from temperature and salinity in section 3.2, and the spatial distribution of transformation in section 3.3. The results and conclusions are presented in section 4.

4.2 Model and Methods

4.2.1 The Southern Ocean State Estimate

The Southern Ocean State Estimate (SOSE) is an eddy-permitting, data-assimilating, ocean general circulation model based on the MITgcm (Mazloff et al., 2010). The model

is configured in a domain from 24.7°S to 78°S with an open northern boundary, with 1/6° horizontal resolution and 42 uneven vertical levels, ranging from 10 m thickness at the sea surface to 250 m in the abyssal ocean. SOSE employs software developed by the consortium for Estimating the Climate and Circulation of the Ocean (ECCO; `http://www.ecco-group.org`) to assimilate the majority of available in situ observations using an adjoint method. Assimilated observations include, but are not limited to, Argo profiling float data, Global Ocean Ship-based Hydrographic Investigations Program (GO-SHIP) hydrographic data, Marine Mammals Observing the Ocean Pole to Pole (MEOP) CTD data, satellite-based sea surface height and sea surface temperature. The solution is optimized by minimizing a cost function, which is the uncertainty-weighted misfit of the model state and the observations. A 1° global state estimate (Forget, 2010) is used for the initial and northern open boundary conditions. The atmospheric state is initialized using the ECMWF ERA-interim global reanalysis (Dee et al., 2011), and these initial conditions and atmospheric state are adjusted by the model adjoint to minimize the cost function. SOSE air-sea fluxes have been extensively validated and shown to reduce biases in reanalysis flux products (Cerovečki et al., 2011).

Sub-gridscale paramaterizations are employed to represent small scale mixing processes, with coefficients typical of those used in eddy-permitting models. The horizontal biharmonic diffusivity parameterization (10^{10} m^4 s^{-1}) is employed to represent the unresolved sub-grid scale mixing (Mazloff et al., 2010). There is no isopycnal mixing paramaterization in SOSE. Rather, the resolved eddies themselves, obeying dynamical constraints, naturally stir along isopycnals. The small-scale tracer variance generated by this isopycnal stirring is dissipated by a combination of vertical, horizontal, and numerical mixing. The K-profile parameterization (KPP) scheme (Large et al., 1994) is employed to represent unresolved mixing processes, and below this the diffusivity decays to a constant background vertical diffusivity ($10^{-5}m^2$ s^{-1}) in the interior below the

KPP boundary layer.

Although SOSE includes no additional parameterizations besides a constant background diffusivity below the KPP boundary layer, mixing arises due to constant vertical mixing or cabbeling or thermobaricity that result from a combination of eddy mixing and nonlinearities in the equation of state. Thus density changes in the ocean interior can be enhanced by strong gradients generated by mesoscale eddy activity. SOSE does not adequately resolve bottom boundary layers due to low vertical resolution of the model grid in the deep ocean nor does it include internal lee wave parameterizations. Thus, there are diapycnal mixing processes in the abyssal ocean responsible for significant water mass transformation of Antarctic Bottom Water (AABW) that are not represented here (Nikurashin and Ferrari, 2013; Waterhouse et al., 2014). Therefore we will focus only on the magnitude and spatial distribution of diapycnal changes in deep water density classes in the interior.

For this study we use the SOSE iteration-100 solution, which has been extensively validated against observations (Abernathey et al., 2016; Tamsitt et al., 2016, 2017), and spans six years (2005-2010).

4.2.2 Lagrangian experiment and analysis

The Lagrangian particle release experiment was run offline with the SOSE daily velocity output, using Octopus (`https://github.com/jinbow/Octopus`) (Tamsitt et al., 2017). The particle tracking model uses a fourth-order Runge-Kutta scheme in time, and the tri-linear interpolation scheme in space to retrieve particle velocity from the surrounding 8 gridded SOSE velocity points. Particles are integrated with the deterministic SOSE daily averaged velocities with a parameterization of diffusion for unresolved processes that are absent from the explicitly resolved velocity field. The diffusion is modeled by a random walk scheme, as described in Tamsitt et al. (2017), with a hor-

izontal diffusivity of 25 m^2 s^{-1} and a vertical diffusivity of $1x10^{-5}$ m^2 s^{-1}. The model implements a reflective boundary condition at the surface and bottom. When particles are within the ML, a random reshuffle of the vertical position of the particle within the ML is included every 5 days to represent ML turbulence that is not explicitly resolved in the SOSE velocities (Tamsitt et al., 2017). The majority of this analysis will focus on the particle trajectories prior to first entering the ML, so will not be significantly affected by the ML parameterization.

A total of more than 2.5 million particles were released at 30°S in the 1000-3500 m depth range in each ocean basin at each grid point (14 vertical levels in SOSE), spanning the σ_2 density range 36.2-37.1 kg m^{-3}, similar to that described in Tamsitt et al. (2017). Particles were re-released at the same location every 30 days for the 6 years of SOSE daily-averaged output, and trajectories were integrated for 200 years, looping the model velocity output similar to a previous Lagrangian particle release experiment using SOSE (Van Sebille et al., 2013). Small model drifts can cause unphysical jumps in density at the looping time-step. To prevent this causing artificial changes in density along trajectories, the vertical position of particles is adjusted to conserve neutral density (γ_n) at the looping time step. Previous work looking at a deep pathway in the South Atlantic found that spatial pathways were insensitive to changes in the length of velocity output used (Van Sebille et al., 2012). However, in this case, with only 6 years of velocity output there may be temporal variability on decadal and longer timescales that is not captured. Longer velocity output is currently unavailable, but in the future further investigation into the importance of longer timescale velocity variability on the results would be valuable.

Similar to Tamsitt et al. (2017), we select the subset of particles with initial southward velocities at 30°S that remain south of 30°S and reach the ML during the 200-year experiment as representing the upwelling branch of the Southern Ocean overturning

circulation. There are several reasons for rejecting particles that go north of 30°S: 1. because we re-release particles at 30°S every month for the first 6 years, the pathways of particles that go north and return back south are represented, provided that they remain within the range of depths as the release; 2. this isolates transformation happening to deep water particles only south of 30°S; and 3. SOSE has a northern boundary at 25°S where particles can leave the northern boundary so we cannot account for the particles that exit this boundary. The resulting analysis includes 87,000 particle trajectories, less than 5% of the original >2.5 million particles released. This small fraction arises mostly because of very broad initial conditions, and we are confident that the sample adequately represents the vast majority of the Southern Ocean upwelling and have accounted for the destination of the remaining particles. Breaking down the fate of all of the particles: at the release, 44% of the particles have initial southward velocities in the depth layers we are interested in (the velocities are split almost equally northward and southward and we had initially seeded over a slightly broader depth range). Considering only those that do go south initially, 75% of these cross north of 30°S at some stage and do not upwell within 200 years, 15% go north of 30°S at some point before returning south and upwelling in the Southern Ocean, and 2.5% remain south of the 30°S and never upwell. The remaining 7.5% stay south of 30°S and upwell within 200 years, which are the particles analyzed here. The fate of the 2.5% that remain unaccounted for in the Southern Ocean without upwelling is of interest, and we have quantified that 10% of these remaining particles entered the AABW density class without upwelling.

In Tamsitt et al. (2017), the authors 'tagged' particles with volume transport at the release location to track the relative transport carried by particles between 30S and the mixed layer. With this tagging method, the total transport of the upwelled particles using the same criteria as this analysis in SOSE is 21.3 Sv, compared to 29 Sv in the southward limb of the overturning streamfunction in SOSE. We note that the two esti-

mates are not expected to agree exactly as we only select particle trajectories that reach the mixed layer, while in the overturning streamfunction, there is a portion of the southward upwelling limb that is entrained into either intermediate or abyssal waters in the interior without ever reaching the mixed layer. Additionally, there is likely a small fraction of Lagrangian particle-transport that takes longer than 200 years to upwell and thus is not captured in our total transport. The upwelling pathways in SOSE were shown to agree well with two 1/10° resolution models, and all three showed similar topographic hotspots of upwelling (Tamsitt et al., 2017).

The timescale for particles to upwell from 30°S to the ML in SOSE is approximately 60-90 years, although these timescales are faster in the 1/10° models. It is likely that a 'tail' of upwelling particles that take longer than 200 years to upwell is not captured, as shown in the shapes of the transit time distributions (Figure 4 in (Tamsitt et al., 2017)). As a result, slower upwelling pathways (e.g. from the Pacific Ocean) may be underrepresented in our results. The ML was defined in SOSE at each location and time using the second derivative of density to find the inflection point at which $\partial\rho/\partial z$ switches sign. This method was chosen because it gives reasonable estimates over a broad range of regions, where threshold methods may not perform well in poorly stratified regions such as the Weddell and Ross Seas (Holte and Talley, 2009). We note this mixed layer depth definition differs slightly from the KPP boundary layer depth, which is defined using a bulk Richardson number criterion and means that the depth at which the KPP scheme has enhanced vertical diffusivities may differ somewhat from the mixed layer depth.

The potential temperature, salinity (PSU) are recorded following each individual trajectory, from which we calculate the potential density referenced to 2000 m (σ_2) using the TEOS-10 nonlinear equation of state (McDougall and Barker, 2011). σ_2 is chosen as the 2000 m reference density, reflecting the mean depth of the initial particle release

locations. We choose to analyze σ_2 rather than γ_n because σ_2 is a quasi-material variable, that is, it changes only as a result of irreversible mixing processes, while γ_n is not (McDougall and Jackett, 2005; McDougall and Barker, 2011). Additionally, there are technical difficulties that make it very challenging to calculate the Eulerian water mass transformation rate in γ_n online in SOSE (see Section 2.3). We recognize that there are disadvantages to using σ_2, particularly the fact that thermobaric effects are not included in the analysis in σ_2, that are captured by calculating water mass transformation in γ_n. Thermobaric effects are strong in the Southern Ocean because of steep isopycnal slopes and large isopycnal temperature gradients (Klocker and McDougall, 2010; Stewart and Haine, 2016; Groeskamp et al., 2016). Thus, to show that our results are not qualitatively influenced by the choice of density coordinate, we show the overall Lagrangian water mass transformation in both σ_2 and γ_n, but present the rest of the analysis in σ_2 in order to compare with Eulerian water mass transformation in SOSE (Section 3.3).

The majority of particles cross into the ML at depths in the upper 100 m - 200 m, but there is a long tail of particles that upwell across deep winter MLs (Fig. 4.2a). The SOSE solution has a deep convection event in the Weddell Sea in 2005 (which did not occur in ocean observations), leading to MLs deeper than 1000 m, but these influence only a small fraction of particles. It has been demonstrated that the instantaneous ML is not a good boundary to separate the region of the ocean with large diapycnal changes due to surface processes from the interior, and that significant water mass transformation occurs just below the ML (Iudicone et al., 2008c). Therefore, to separate particles in the interior from particles exposed to surface heat and freshwater fluxes, we define the "surface diabatic layer" (SDL) as the maximum σ_2 at each latitude and longitude that outcrops at least once during the 6-year SOSE iteration (Fig. 4.2) (Cerovečki and Marshall, 2008). This essentially separates isopycnal layers that "feel" the surface at some time during the 6 years from those that are never exposed to surface fluxes. This is

similar to the "mixed layer bowl" concept used by Marshall et al. (1999) and Iudicone et al. (2008a), which identifies the maximum ML depth at each location.

We wish to clarify the language used to describe water mass transformation in this analysis. A process is considered "adiabatic" if it occurs without exchange of heat and also without the internal dissipation of kinetic energy (McDougall and Barker, 2011). In the literature, the word "adiabatic" is often used to refer to a circulation that occurs without modifying the buoyancy of seawater. This usage is correct in idealized models that consider only temperature and not salinity (e.g. Wolfe and Cessi, 2011; Nikurashin and Vallis, 2011). However, when salinity is present, it is more accurate to describe a circulation pathway as "isopycnal" when the buoyancy remains constant and "diapycnal" when it is not. We strive to use these terms correctly, making exceptions in cases of established terminology, such as the "surface diabatic layer" (Cerovečki and Marshall, 2008), which refers to the upper-ocean layer that is exposed to surface forcing.

The SDL in SOSE shows very dense waters, with σ_2>37.1 kg m^{-3}, outcropping south of the ACC at some time during the 6-year iteration (Fig. 4.2b). The mean SDL depth exceeds 1000 m in the Weddell and the western Ross Seas, due to inversions in the σ_2 profile in these regions (Fig. 4.2c). Outside of these two regions, the SDL depth is similar to the "mixed layer bowl", and the results following are qualitatively similar using a "mixed layer bowl" rather than the SDL (not shown) (Fig. 4.2d). Particles take a median of 79 years, with a standard deviation of 42 years, to travel from 30°S to first crossing of the SDL, compared to a median of 17 years (25 years standard deviation) to travel between first crossing of the SDL and crossing the ML. Thus, an average particle spends approximately 1/5 of its total upwelling time traveling between the SDL and the ML.

It is worth noting that with background diffusion, we should not view any single particle trajectory as a "pathway", but view water mass pathways as a statistical quan-

tity from an ensemble of particles. It is useful to define the probability density function based on a large group of particles, which can be used to calculate the first and higher order moments to gain more insight into the process of the water mass transformation. The probability density function (PDF) in this Lagrangian method is simply defined as the normalized particle distribution within any variable space tagged along the particle trajectories, such as density, temperature, salinity or eddy kinetic energy. It is numerically calculated by binning particles and counting the particle numbers in each bin. We denote the property χ of the i^{th} particle as χ^i. The particle PDF in χ space is written as

$$P(\chi) = \frac{1}{N}\sum_{i=1}^{N}\xi_i,$$
$$\xi_i = \begin{cases} 1, \text{ if } \chi - \delta/2 < \chi^i \leq \chi + \delta/2 \\ 0, \; else \end{cases} \tag{4.1}$$

where N is the total number of particles, and δ is the bin width. In the following, we will replace χ with density, potential temperature, salinity, and eddy kinetic energy to examine the Southern Ocean upwelling pathways from different perspectives.

4.2.3 Eulerian water mass transformation analysis

A useful complementary analysis to the Lagrangian experiments is to directly calculate Eulerian water mass transformation in SOSE, which will be compared and contrasted with the Lagrangian results in section 3.3. Water mass transformation quantifies the rate at which water masses change their properties due to irreversible thermodynamic processes (mixing and boundary fluxes). Here we consider water mass transformation in σ_2 potential density coordinates (Marshall et al., 1999). In a steady state, the net water mass transformation within an ocean basin must match the volume inflow/outflow

at the basin boundary (Walin, 1982). Because of this conservation property, water mass transformation rates are usually presented as integrals over whole basins. However, it is also possible to calculate a transformation map, which describes the rate of water mass change at each point in space (e.g. Brambilla et al., 2008). This "local" transformation rate is equivalent to the diapycnal velocity in thickness-weighted isopycnal coordinates (Young, 2012).

The potential density equation is

$$\frac{D\sigma_2}{Dt} = \dot{\sigma}_2 = \frac{\partial \sigma_2}{\partial \theta}\dot{\theta} + \frac{\partial \sigma_2}{\partial S}\dot{S}\,, \tag{4.2}$$

where $\dot{\theta}$ and $\dot{S}$ represent all non-advective sources (i.e. external forcing and mixing) of potential temperature (θ) in degrees Celsius and salinity (S) in PSU, respectively. The partial derivatives $\partial\sigma_2/\partial\theta$ and $\partial\sigma_2/\partial S$ are related to thermal expansion and haline contraction and are evaluated from the model's thermodynamic equation of state (Jackett and Mcdougall, 1995). The local transformation rate is defined as

$$\omega(x, y, \sigma_2, t) = \frac{\partial}{\partial \sigma_2}\overline{\int_{\sigma_2' < \sigma_2} \dot{\sigma}_2 dz} \tag{4.3}$$

where the overbar indicates a time average (here over the six-year SOSE integration interval) and the integration is performed in the vertical up to the target isopycnal depth. ω has units of m s^{-1}.

This expression is evaluated numerically by discretizing σ_2 into 400 unevenly spaced bins. The bin spacing $\Delta\sigma_2$ varies from 0.025 kg m^{-3} at low density to 0.0025 kg m^{-3} at high density. This spacing was chosen to provide good resolution of the high-density polar water masses, which occupy a relatively small segment of the density

range but with a large depth range. Within each bin, (4.3) is evaluated numerically as

$$\omega(x,y,\sigma_2,t) = \frac{1}{\Delta\sigma_2}\overline{\sum_{k=1}^{N_z} \dot{\sigma}_2 h_c \Delta z_f \delta(\sigma_2 - \sigma_2')} \tag{4.4}$$

where h_c is the partial grid cell fraction (Adcroft et al., 1997), and Δz_f is the height of the tracer grid cell, and N_z is the number of vertical grid cells. The function $\delta(\sigma_2 - \sigma_2')$ is a numerical delta function, defined as

$$\delta(\sigma_2 - \sigma_2') = \begin{cases} 1 & \text{if } (\sigma_2 - \Delta\sigma_2/2) <= \sigma_2' < (\sigma_2 + \Delta\sigma_2/2) \\ 0 & \text{else} \end{cases} . \tag{4.5}$$

The time averaging in (4.4) is performed "online," i.e. at every timestep as the model is running, using the MITgcm LAYERS package. (The highest possible temporal resolution is required for accurate calculation of of water mass budgets (Cerovečki and Marshall, 2008; Ballarotta et al., 2013; Bryan and Bachman, 2015).) The non-advective potential density tendency $\dot{\sigma}_2$ is the sum of six individual sub-components corresponding to surface forcing, vertical mixing (including the KPP parameterization), and horizontal mixing for both potential temperature and salinity, enabling a detailed decomposition of the thermodynamic processes that drive changes in water mass density.

Over a very short interval, ω should in principle be equal to the rate with which Lagrangian particles move across isopycnal surfaces. This equivalence breaks down, however, for long averaging times and when only a subset of particles is analyzed (as is the case for the upwelling particles examined here). Nevertheless, comparing Lagrangian density changes to Eulerian water mass transformation maps helps understand the thermodynamic drivers of the density changes (e.g. mixing vs. surface forcing).

4.3 Results

4.3.1 Lagrangian water mass transformation

It is instructive to take a probabilistic approach to cumulative density changes along particle trajectories, thus showing the likelihood of a deep water particle falling within a range of densities using particle PDFs as defined in Equation 1. With this tool we can quantify the probability that a water parcel from the deep ocean will upwell along isopycnals, and the likelihood that its density will increase or decrease. We define the density anomaly, $\Delta\sigma_2$ (in units of kg m^{-3}), as the difference between density at a given point in time and the initial density at the release location at 30°S. $\Delta\sigma_2$ represents the cumulative, or net, density change between release and a given location and time, and thus density increases and decreases can occur in between that are compensated, leading to no net density change. We note that as particles get closer to the sea surface, particularly as they travel between the SDL and ML, the $\Delta\sigma_2$ values misrepresent the actual diapycnal density change, as the σ_2 coordinate drifts further from the true isopycnal surface toward the sea surface. (Particles that become lighter in σ_2 are actually becoming even more buoyant, as seen by the rotation of σ_θ contours relative to σ_2 contours.) We bin the density and density anomaly in 0.1 kg m^{-3} bins to obtain the sample PDF. In Figure 4.3, we show the PDFs of density and density anomaly at the particle release location, first crossing of the SDL and first crossing of the ML, with the contributions from particles originating in the Atlantic, Indian and Pacific to the total PDF shown individually (Fig. 4.3).

The distribution of density at the particle release locations (Fig. 4.3a) is broad but unevenly distributed in σ_2 space. Because the particles are released in an even distribution in depth space at 30°S, they are unevenly distributed in density space and the chosen subset of particles that eventually reach the ML furthers the uneven sampling in

density space. In this case, we have chosen to distribute evenly in depth space as this more accurately represents the total volume of upwelling deep water and thus density classes with larger volume have a larger contribution to the bulk density statistics. As is clear in Figure 4.3a, our analysis includes a broad range of densities, so to further understand the changes in density during upwelling, we define separate water masses within this range. Using the same water mass definitions as used to analyze the same iteration of SOSE in Abernathey et al. (2016) (following Speer et al. (2000) and Downes et al. (2011)), we define four water masses: Intermediate Waters (IW), Upper Circumpolar Deep Water (UCDW) and Lower Circumpolar Deep Water (LCDW) and Antarctic Bottom Water (AABW) (Table 4.1). The results are not sensitive to the exact water mass definitions. We also note that we refer to deep water originating in each ocean as North Atlantic Deep Water (NADW), Indian Deep Water (IDW), and Pacific Deep Water (PDW), but for this analysis these definitions refer only to the basin of origin and not a particular density range.

At 30°S, the mode in the PDF of σ_2 is 36.9 kg m^{-3} and the distribution is skewed toward lighter densities, with a sharp drop off in the probability of particles being denser than 36.9 kg m^{-3} and a broad tail of lighter particles. The particles are divided with 8.3% initially in the IW density range, and the remaining split almost equally between the UCDW and LCDW density classes. The distributions of σ_2 in each basin show that upwelling particles originating in the Pacific dominate the total number of upwelling particles, and more Pacific particles originate at lighter densities than those originating in the Atlantic and Indian Oceans.

When particles first cross the SDL, the distribution of particle σ_2 has become more evenly distributed, with fewer particles occupying the lightest density classes, and a broadened peak encompassing dense UCDW and light LCDW (Fig. 4.3b). The distribution of $\Delta\sigma_2$ at the time when particles cross the SDL for the first time is symmetric

and centered close to zero (i.e. no net density change), with a mean $\Delta\sigma_2$ of -0.01 kg m^{-3} and a standard deviation of 0.16 kg m^{-3} (Fig. 4.3d). Thus the net diapycnal transformation in the ocean interior prior to reaching the SDL is small, mostly characterized by a spread of the PDF to both higher and lower densities rather than a shift in the mean. We note that the the small total mean density decrease below the SDL is mostly due to particles originating in the Atlantic and Indian, with mean $\Delta\sigma_2$ of -0.01 and -0.03 kg m^{-3}, respectively, while the mean Pacific $\Delta\sigma_2$ is negligible.

In contrast, when particles reach the ML for the first time, the distribution of σ_2 of particles from all origins has changed significantly, with 68% of particles lighter than at their initial density at release. There is a broad tail at higher densities, including 2.1% of particles denser than 37.2 kg m^{-3}, which have mixed with denser waters to enter the AABW density class prior to reaching the ML (Fig. 4.3, Table 4.1). We note that this 2.1% of particles only captures particles converted to AABW that upwell to the mixed layer and thus does not represent the full conversion of deep waters to AABW, as there is likely a subset of particles converted to AABW that never reach the mixed layer. At the ML crossing, the PDF of $\Delta\sigma_2$ remains symmetric, but the distribution is shifted toward substantially lighter densities, with a mean density anomaly of -0.12 kg m^{-3} and standard deviation of 0.24 kg m^{-3}. This distribution is similar for all three basins of origin. This shows that between the SDL and ML, particles undergo much larger net density changes relative to changes before crossing the SDL, with a strong bias toward lighter densities. This result justifies the use of SDL as a definition for separating the interior ocean, where the upwelling is relatively isopycnal and transformation results from mixing, from the upper ocean where surface forcing also contributes resulting in a much larger net density change.

Figure 4.4 shows the same PDFs as Figure 4.3 but calculated using γ_n as the density coordinate rather than 4.3. The distributions of density and density anomaly are

very similar, indicating that our conclusions are not particularly sensitive to the choice of density coordinate. In particular, the $\Delta\sigma_2$ and $\Delta\gamma_n$ at the SDL crossing (Figs. 4.3d,4.4d) are almost identical, with the same mean and very similar standard deviations (0.16 for $\Delta\sigma_2$ and 0.14 for $\Delta\gamma_n$). Above the SDL, where there are larger differences between σ_2 and γ_n surfaces, the density change is generally larger in γ_n than σ_2. The mean of $\Delta\gamma_n$ at the ML crossing are -0.26 kg m^{-3}, more than double that of $\Delta\sigma_2$ (-0.12 kg m^{-3}) and the standard deviation of $\Delta\gamma_n$ (0.76 kg m^{-3}) is three times that of $\Delta\sigma_2$ (0.24 kg m^{-3}). The result that density decreases more in γ_n is somewhat surprising, as previous water mass transformation analyses indicate that thermobaricity (which is captured in γ_n but not σ_2) increases density in deep waters in the Southern Ocean (Groeskamp et al., 2017).

Given the wide range of initial densities captured in Figure 4.3a, it is useful to look at the evolution of particle densities as a function of initial density as differing transformation of individual density classes may be obscured in the bulk PDFs in Figure 4.3. Figure 4.5a shows a joint PDF of particle initial release density and density at the SDL crossing, with values above the 1:1 line indicating a net density increase and below the 1:1 line indicating a net density decrease. These changes result from mixing, which can cause density to increase or decrease, or from cabbeling, which only increases density, or thermobaricity, which can increase or decrease density. The lightest waters (IW density class) show a distinct shift toward the denser UCDW density class, while particles originating in the UCDW density class with σ_2>36.8 kg m^{-3} shift toward lighter densities during upwelling, leading to a convergence of these two water masses. This density convergence may result from mixing of different source deep waters as they interact in the ACC. The small net lightening of the UCDW implies that the mixing processes making them lighter are more vigorous than cabbeling. In contrast, the particles originating in the densest LCDW tend to become denser during upwelling, with a very small fraction reaching AABW densities by the time they cross the SDL. Cabbeling

may contribute significantly to this densification of LCDW, as observations suggest that there is significant formation of dense LCDW and AABW by cabbeling in the Southern Ocean (Foster, 1972; Groeskamp et al., 2016).

The buoyancy gain of UCDW particles and buoyancy loss of the densest LCDW particles results in divergence toward two separate water masses in the ocean interior, as is visible in the two peaked structure in Figure 4.3b. This transformation of deep water toward lighter IW and denser AABW in the ocean interior prior to reaching the mixed layer has been shown in previous model analysis (Iudicone et al., 2008a). We note that because we consider only particles that upwell to the ML, there is likely a subset of deep water particles entrained into AABW that never outcrop into the mixed layer and thus are not captured in this Lagrangian analysis.

After crossing the SDL, but before reaching the ML, a strong shift toward lighter densities is clear for all particles apart from those crossing the SDL at densities greater than σ_2 = 37.0 kg m^{-3}. These densest waters show similar likelihoods of increasing or decreasing density before reaching the ML, causing further divergence of the densest waters from the bulk of particles reaching the ML as UCDW. Our analysis shows that while upwelling in the interior below the SDL is relatively isopycnal, the upwelling deep water experiences large diapycnal changes before crossing the ML, is significantly modified by mixing, and is influenced by surface heat and freshwater fluxes. This is consistent with previous work that finds substantial water mass transformation below the ML (Iudicone et al., 2008a). Again we compare the density anomaly in σ_2 (Fig. 4.5a,b) to γ_n (Fig. 4.5c,d) and find the results are qualitatively very similar, but there are larger density decreases between the SDL and ML when calculated in γ_n relative to σ_2 similar to (Fig. 4.4). To aid in the comparison with Eulerian water mass transformation in SOSE, for the remainder of the analysis we will show the lagrangian transformation using σ_2 as the density coordinate.

Our results suggest that some of the deep water originating in the Atlantic and Indian that is initially in the LCDW density range is converted to the UCDW density range prior to reaching the mixed layer (Figs. 4.3a,b), resulting in distributions of densities at the SDL crossing that are more similar to the Pacific deep water distribution (which is essentially unchanged). We find that the transformation of deep water between 30°S and reaching the northern ACC boundary differs by basin (not shown), but once particles enter the ACC and eventually cross the SDL, the density distributions are much more similar, but retain small mean density differences, as will be shown in more detail in the next section. Very few particles analyzed here that upwell all the way to the mixed layer are transformed to AABW before crossing the SDL. However, it is important to note that transformation of Deep Waters to AABW may take place largely below the mixed layer and in polynyas; particles that transform from Deep Water to AABW without entering the mixed layer are not represented in our analysis. Moreover, the AABW production rate appears to be significantly underestimated in SOSE compared with observed transports, as reported in many papers and summarized in Talley (2013a). Further analysis in upcoming years with models of increased spatial resolution and more realistic polynya representation will be of great interest in this regard.

4.3.2 Changes in temperature and salinity

We further decompose the density change along trajectories into separate contributions from temperature and salinity, using the relationship $\Delta\sigma_2 = -\alpha(\theta, S)\Delta\theta + \beta(\theta, S)\Delta S$, where θ is potential temperature, S is salinity, α is the thermal expansion coefficient, and β is the haline contraction coefficient (both coefficients calculated at a pressure of 2000 db). We note that this decomposition would not be possible with neutral density without the addition of a constant factor that depends on space (Iudicone et al., 2008b). Similar to Iudicone et al. (2008a), we approximate this using an inte-

gral approach as $\Delta\sigma_2 \approx -\alpha(\overline{\theta},\overline{S})\Delta\theta + \beta(\overline{\theta},\overline{S})\Delta S$, where the overbar is the average of the initial and final values. The sum of the temperature and salinity contributions to $\Delta\sigma_2$ derived in this way agrees closely with the total density change (Fig. 4.6).

At the SDL crossing, there is strong compensation between temperature and salinity changes, but with a large overlap in the $\Delta\theta$ and ΔS distributions. $\Delta\theta$ is shifted toward positive values, indicating mixing with colder water, while salinity is shifted toward negative values, indicating mixing with fresher water (Fig. 4.6a). The colder and fresher water that mixes along isopycnals with the upwelling deep water likely originates as Antarctic Surface Water at the sea surface. At the ML crossing, there is less overlap in the $\Delta\theta$ and ΔS distributions and they are no longer density-compensated, with the ΔS distribution centered further to the left (Fig. 4.6a). Therefore, the shift in $\Delta\sigma_2$ toward lighter densities between the SDL and the ML is accomplished by decreasing salinity. In the same iteration of SOSE, Abernathey et al. (2016) found that vertical mixing of salt is the dominant contribution to the total water mass transformation in these same density classes due to mixing in the upper ocean, consistent with our Lagrangian result that ΔS causes the shift of σ_2 toward lighter densities above the SDL.

The distribution of particle densities can also be visualized in thermohaline coordinates (i.e. θ-S space), which can shed insight on the circulation beyond geographical coordinates (Zika et al., 2012; Döös et al., 2012; Groeskamp et al., 2014) (Fig. 4.7). This allows a clear distinction to be made between compensated changes in temperature and salinity due to isopycnal mixing and diapycnal mixing which leads to density change. We note that changes in θ-S coordinates can occur both as a result of advection of a particle across temperature and salinity gradients, and due to local changes in temperature and salinity at a fixed location (Groeskamp et al., 2014). Figure 4.7 shows three examples of particle trajectories in θ-S space and their corresponding geographic locations, illustrating different pathways. Combining all upwelling trajectories, joint PDFs

of particle θ and salinity in thermohaline coordinates at the release, SDL crossing, and ML crossing shows the progression of upwelling deep water from relatively warm and salty to colder and fresher at the SDL crossing and to three distinctly separate water masses at the ML crossing (Fig. 4.8).

Between 30°S and the SDL, the core water mass properties of particles originating in the Atlantic show a predominantly isopycnal shift from the warm, salty signature of NADW toward colder, fresher waters (Fig. 4.8a). In contrast, there is weaker modification of particles originating in the Indian (Fig. 4.8b), and very little modification of deep water with Pacific origin (Fig. 4.8c) below the SDL. The result is a convergence of water masses with different initial properties toward a single similar T-S distribution by the time particles reach the SDL (Fig. 4.8d). Because the change in temperature and salinity is mostly density-compensated even though well known (e.g. Sloyan and Rintoul, 2000)), this transformation of NADW along density surfaces is often taken for granted, but was central to a global analysis of the ocean circulation in thermohaline coordinates (Zika et al., 2012). In addition to compensated change in properties, there is a very slight density decrease in Atlantic and Indian waters between 30°S and the SDL, as in Figure 4.3b.

Between the SDL and ML, the θ-S properties diverge into three distinct water masses: a relatively warm, salty water mass of particles that upwell into the ML in subtropical western boundary currents (annotated as i. in Fig. 4.8a); a broad, colder water mass spanning UCDW density classes (annotated as ii. in Fig. 4.8a); and a separate water mass with close to freezing temperatures with the saltiest waters crossing into AABW densities (annotated as iii. in Fig. 4.8a). As shown in Figure 4.5, this also indicates the divergence of water mass properties into two distinct branches prior to entering the ML and being exposed to direct surface buoyancy fluxes. It is also clear in Figure 4.8d that the center of mass of the density distribution of Atlantic deep water is initially

slightly denser than Indian and Pacific deep waters. This mean density difference, albeit small, remains similar at 30°S, the SDL and ML, although the θ-S characteristics change substantially. Thus, although there is convergence of water masses in θ-S space in the interior and a large overlap in the density distribution of different deep waters, the difference in center of mass of the particle distribution between the Atlantic and Indo-Pacific deep waters is preserved during upwelling. This is consistent with the results of Talley (2013a) and others that find the signature of deep waters of Atlantic origin is found at a higher density (and below) Indian and Pacific deep waters.

An important caveat that errors in our estimates of diapycnal change in σ_2 coordinates may be important in the upper ocean is clearly illustrated by the difference in slope of σ_2 and σ_0 contours in θ-S space shown in Figure 4.8d. The density change between the SDL (magenta) and ML (orange), where particles are in the upper ocean, is significantly larger in σ_θ than in σ_2, suggesting that our $\Delta\sigma_2$ may be underestimating the true density change in the upper ocean.

4.3.3 Spatial distribution of transformation

It is clear from sections 3.1 and 3.2 that there are significant transformation along Lagrangian upwelling pathways in the interior of the Southern Ocean, but we take this a step further to look at where these processes occur spatially. Using the local density time rate of change along particle trajectories, $d\sigma_2/dt$, we bin the particle $d\sigma_2/dt$ in 1° latitude x1° longitude spatial bins for all particles at all times, and average all values in each bin to obtain an ensemble estimate of the density change rate at each location. Additionally, we separate the times at which particles are below the SDL and above the SDL, and bin average these separately to estimate the mean $d\sigma_2/dt$ in the ocean interior and the $d\sigma_2/dt$ above the SDL (Fig. 4.9).

The maps of ensemble mean $d\sigma_2/dt$ in the interior and in the SDL show that,

to first order, $d\sigma_2/dt$ along trajectories in the SDL is an order of magnitude larger than in the interior (Fig. 4.9). In the interior, although $d\sigma_2/dt$ is relatively small, there is clearly enhanced ensemble mean $d\sigma_2/dt$ of similar magnitude to above the SDL in some locations, particularly in boundary currents, close to major topographic features and along the Antarctic coastline. Regions with high EKE (region within green contours in Fig. 4.9a) encompass much of the enhanced interior $d\sigma_2/dt$ in boundary currents and near topography, but exclude enhanced transformation elsewhere, particularly along the Antarctic continental slope. The background transformation below the SDL is generally very weakly increasing density (positive transformation), but there are notable regions where particle density is decreasing (negative transformation). This includes the Agulhas Return Current and regions at major topographic features along the ACC, including the Kerguelen Plateau, Macquarie Ridge, Pacific-Antarctic Ridge and Drake Passage, where there are hostpots of negative transformation (Fig. 4.9a). The weak negative transformation in the Agulhas Current and Agulhas Return Current region is likely an important contribution to the weak mean negative $\Delta\sigma_2$ at the SDL of particles originating in the Atlantic and Indian (Fig. 4.3d) as particles from the Western Indian and Eastern Atlantic pass through this region (Fig. 4.2a,b).

In order to determine which processes cause diapycnal density change, it is useful to compare the Lagrangian statistics with Eulerian estimates of transformation across density surfaces, which can be broken into contributions from surface fluxes of temperature and salt, horizontal mixing, and vertical mixing. The cumulative transformation recorded by particles could have occurred anywhere along their trajectories, which do not remain on a single density surface, so are not expected to agree precisely with the water mass transformation across a given isopycnal surface. We focus here on the Eulerian transformation on an isopycnal due to horizontal and vertical mixing, and particularly in the interior, to compare with the density changes along Lagrangian trajectories below

the SDL and ML.

The transformation due to mixing across the 36.7 kg m^{-3}<σ_2<36.9 kg m^{-3} range (corresponding to the center of the UCDW density class) shows a very small transformation north of and within the ACC and broad negative transformation toward lighter densities south of the ACC (Fig. 4.10). This region of negative transformation of light UCDW along the southern ACC boundary and south of the ACC encompasses the locations where most particles first outcrop into the mixed layer (Figure 4.1e).

This distribution is consistent with the Lagrangian distributions of σ_2 and $\Delta\sigma_2$, which show generally small transformation during interior upwelling but a distinct shift toward lighter densities as they approach the ML, which occurs predominantly south of the ACC. There are a few notable exceptions to this pattern, with significant positive transformation on the southern side of the ACC in Drake Passage, along the Pacific-Antarctic Ridge, south of Kerguelen Plateau and in the western Ross Sea. In these locations, density increase by mixing of temperature exceeds density decrease due to mixing of freshwater (Fig. 4.10b,c).

The broad region of negative transformation south of the ACC is due to mixing of both temperature and salinity, although along some regions along the southern ACC boundary there is strong compensation between mixing of temperature and salt, with mixing of salt dominating in these locations (Fig. 4.10b,c). This is generally in agreement with the Lagrangian temperature and salinity contributions to $\Delta\sigma_2$ in Fig. 4.6. However, the $\Delta\theta$ and ΔS contributions from the Lagrangian analysis indicate that mixing of heat leads to a net increase in density for most particles, which would correspond with positive transformation, while the map of transformation due to mixing of temperature shows regions of both positive and negative transformation.

The result that mixing of freshwater is the dominant term transforming UCDW to lighter densities is consistent with previous water mass transformation analyses showing

that vertical mixing of deep water with fresher waters above dominates the total mixing contribution to transformation (Abernathey et al., 2016), and leads to conversion of UCDW to IW below the ML (Iudicone et al., 2008a). Iudicone et al. (2008a) propose that this freshening occurs as UCDW is approaching the upper ocean in the region south of the ACC where upward Ekman pumping brings UCDW up to where it encounters strong salinity gradients just below the mixed layer, mixing with fresher water to gain buoyancy.

The transformation averaged over isopycnal layers for 37.0 kg $m^{-3} < \sigma_2 <$ 37.15 kg m^{-3}(Fig. 4.11) corresponds to the secondary peak in densities at the SDL crossing (Fig. 4.3b) within the LCDW density class. Separating the transformation due to mixing of temperature and mixing of salt clearly shows strong compensation, consistent with the Lagrangian analysis (Fig. 4.6). Over this density range, the impact of mixing is to very weakly increase density north of and within the ACC, with localized areas of stronger density increase and decrease south of the ACC where the isopycnals are closer to the sea surface (Fig. 4.11). The broadly positive transformation within and north of the ACC in this range is a result of horizontal mixing (not shown) and is consistent with the Lagrangian statistics showing that particles initially in the denser LCDW density range tend to increase density in the interior, diverging from the lighter water masses during upwelling to the SDL (Fig. 4.5). There is stronger transformation, both positive and negative, south of the ACC where the LCDW density surfaces shoal toward the surface. In particular, there is strong positive transformation near the Antarctic continent where these density surfaces outcrop, corresponding to regions of AABW formation. This densification is caused by dominance of cooling by mixing of temperature (Fig. 4.11b) over freshening by mixing of salt (Fig. 4.11c). Further north in the Weddell and Ross gyres, transformation by mixing of temperature is weak or even negative, indicating warming, and thus the next effect of mixing is to make water lighter in these regions.

Both the Lagrangian $d\sigma_2/dt$ in the ocean interior (Fig. 4.9) and the Eulerian transformation (Figs. 4.10, 4.11) show coherent hotspots of enhanced density change at major topographic features (contoured in grey) where interaction of the mean flow with topography generates vigorous eddy activity. These locations at and downstream of topography are similar to the locations of maximum interior upwelling in the ACC, including the Southwest Indian Ridge, Kerguelen Plateau, Macquarie Ridge, Pacific Antarctic Ridge and Drake Passage region (Fig. 4.1a,b) (Tamsitt et al., 2017). In the ocean interior far from the surface, the total diapycnal mixing is dominated by the horizontal component (not shown), which may be a result of the SOSE prescribed sub-grid mixing parameterizations. Nevertheless, the interior mixing is greatly enhanced in regions with strong fronts and eddy activity, which generate strong horizontal density gradients, which with a constant diffusivity leads to larger transformation.

To quantify the contribution of eddy hotspots associated with topography to cumulative diapycnal transformation along upwelling pathways, we bin particle $d\sigma_2/dt$ by EKE levels. Using the time-mean surface EKE distribution, with the assumption that the spatial pattern of EKE is similar at all depths, we sum the absolute value of $d\sigma_2/dt$ for each particle in each 10 m^{-2} s^{-2} surface mean EKE bin, to obtain the contribution to the particle total transformation as a function of EKE (Fig. 4.12). Comparing the cumulative RMS of particle $d\sigma_2/dt$ as a function of EKE to the total volume in each EKE bin illustrates that areas with high EKE have a disproportionately large influence on particle density change given their volume. This is clearly visible in Fig. 4.12 by the divergence of the two lines at high EKE values (greater than 100 m^{-2} s^{-2}, contoured on Figs. 4.1d and 4.9). However, this divergence is small and the majority of the volume is in regions with low EKE. Therefore, close to 75% of the cumulative RMS $d\sigma_2/dt$ occurs at EKE<100 m^{-2} s^{-2}, while the remaining 25% occurs in regions with EKE>100 m^{-2} s^{-2}. Therefore, while most interior upwelling (i.e. crossing of depth surfaces) occurs

at topographic hotspots (Fig. 4.1d and (Tamsitt et al., 2017)), diapycnal change (crossing of density surfaces) is not as strongly concentrated at these hotspots. This supports the hypothesis presented by Tamsitt et al. (2017) (their Figure 7), that the upwelling is predominantly isopycnal in these hotspots. With this new knowledge, the Tamsitt et al. (2017) isopycnal upwelling at topographic hotspots should be modified to reflect the fact that density change along upwelling pathways the ocean interior is somewhat enhanced in the topographic hotspots, but these density changes are small relative to the transformation that occurs between the SDL and the ML.

4.4 Summary and Conclusions

We have quantified the cumulative water mass transformation along Southern Ocean Lagrangian upwelling pathways in the ocean interior and have summarized the overall water mass transformation and processes involved in an idealized schematic (Fig. 4.13). In the interior, upwelling predominantly follows isopycnal surfaces up until reaching a surface diabatic layer, defined by the densest isopycnal that outcrops at a given location, above which there is strong transformation toward lighter density classes as a result of freshening due to mixing with fresher surrounding water. Despite interior density changes being relatively small, the density distribution of deep water shows a clear migration toward two separate density classes during upwelling, which indicates the early stages of the separation of upwelling waters into the upper and lower branches of the overturning circulation, which is completed by buoyancy fluxes at the sea surface. Although the pathways are close to isopycnal, compensated changes in temperature and salinity leads to homogenization of different source deep waters by mixing with relatively cold, fresh subpolar water.

There is large seasonality of surface buoyancy fluxes and winds, particularly

associated with sea ice, which may lead to seasonality in the density changes along upwelling particle trajectories. This has been shown to be important for water mass transformation due to sea ice in the Southern Ocean (Abernathey et al., 2016). Further analysis of the differences in upwelling and water mass transformation in different seasons is needed to determine how seasonal processes influence upwelling and water mass evolution along these pathways. Additionally, nonlinearities in the equation of state lead to significant water mass transformation in the Southern Ocean due to cabbeling and thermobaricity (Groeskamp et al., 2016). In particular, analysis of observations show significant LCDW formation from UCDW due to nonlinear water mass transformation (Groeskamp et al., 2016). Because most of our analysis is done using potential density, the contribution to the water mass transformation from thermobaric effects are not captured using this density coordinate. However, the qualitative agreement between results using potential density and neutral density indicates that the inclusion of thermobaricity does not change our conclusions, but more work is needed to further quantify the role of nonlinear processes in water mass transformation in upwelling pathways.

There are additional challenges to understand how Lagrangian methods can introduce errors in the density change recorded along particle trajectories, and more attention is needed to address these concerns. There are several potential sources of errors. 1. The aliasing effect: errors are introduced in the trajectory integration using 1-day mean velocity. The effect of super-inertial velocity fluctuation was not taken into account. This type of error is possibly uncorrelated, meaning that it will not introduce a drift in the mean property of a cloud of particles. But it can introduce additional spreading of a cloud of particles, i.e., changing its rate of change of the second moment. However, this type of error should be small because the decorrelation time scale for balanced eddy motion in the Southern Ocean is much larger than 1 day. The deviations from the linear interpolation between daily mean velocities should be negligible comparing to the daily

mean velocity. 2. The random shuffling parameterization in the mixed layer is ad hoc, without rigorous derivation. This is not an important error source in our study as we focus on particles before entering the ML. 3. The horizontal and vertical background mixing parameterizations and values used in SOSE may not represent the true ocean physics. This question is beyond the scope of Lagrangian methods alone but rather is related to numerical simulations in general, for which these parameterizations are continually evolving based on new experimental insights. 4. The Eulerian and Lagrangian models use very different numerical schemes to describe advection processes, each with distinct numerical discretization errors. Since SOSE's conservation laws are derived in an Eulerian finite-volume framework, it is unlikely that the Lagrangian particles maintain rigorous conservation of temperature and salinity the way that grid cells do. In spite of these limitations, the qualitative agreement between the Lagrangian particle and the Eulerian tracer analyses in this study validates the use of the Lagrangian method, which can provide a detailed view of the water mass pathways that is lacking in Eulerian analysis.

Our result that deep source water properties homogenize during upwelling differs somewhat from the prevailing view of NADW and IDW/PDW upwelling in the Southern Ocean interior as separate in density and property space (Talley, 2013a), with denser NADW preferentially feeding into the lower cell and IDW/PDW preferentially entering the upper cell. However, despite the homogenization in properties and broad overlap in the density distribution of Atlantic, Indian and Pacific deep waters, our results do show that the mean of the NADW density distribution remains slightly denser than Indo-Pacific deep waters, and this difference is preserved throughout the transformation that occurs during upwelling. An important caveat to our result is that we consider only particles that upwell all the way to the mixed layer, and thus do not capture deep water that is transformed into AABW in the interior, entering the lower cell without upwelling

to the sea surface. It is possible that analysis of all deep water trajectories entering the Southern Ocean may show a preferential conversion of denser NADW into AABW in the interior, and further work is needed to investigate transformation of deep waters into AABW. In addition, as with many other ocean models with similar resolution, SOSE underestimates the rate of AABW formation processes, thus more detailed analysis of this transformation should be investigated in models that better capture AABW formation.

Here we show that although upwelling predominantly follows isopycnals in the ocean interior, the distinct salty, warm signature of NADW is eroded by density-compensated mixing with colder, fresher water during upwelling through the Southern Ocean interior prior to the influence of surface buoyancy fluxes, leading to homogenization of deep water properties. This result parallels findings from Lagrangian analysis of outflow pathways of AABW, which also show homogenization of distinct source water properties (Van Sebille et al., 2013). At the same time, the overall divergence of densities during interior upwelling into a dominant UCDW water mass and a distinct smaller, dense, LCDW water mass shows the role of interior diapycnal mixing in initializing the water mass transformation necessary for the Southern Ocean upper and lower overturning cells, the rest of which is accomplished by buoyancy fluxes at the surface.

While the instantaneous rate of density change experienced by a particle at topographic hotspots in the ocean interior is elevated compared to elsewhere, the small volume extent of these hotspots, and relatively small amount of time particles spend in these regions means that the majority of cumulative density change along upwelling pathways in the ocean interior occurs as a result of background mixing, consistent with the results of Holzer and Primeau (2006). Additionally, the cumulative transformation in the ocean interior (below the SDL) is dwarfed by density changes influenced by surface fluxes in the upper ocean prior to reaching the mixed layer. In the context of Tamsitt et al. (2017), these results indicate that while upwelling across depth surfaces is strongly

concentrated at hotspots associated with topography, *diapycnal* upwelling across density surfaces is less clearly enhanced at these hotspots. However, SOSE lacks sufficient vertical resolution to resolve the bottom boundary layer, and does not parameterize lee wave driven mixing, and thus is missing important boundary processes that may contribute significantly to the modification of LCDW. While it is well understood that eddy stirring brings water in contact with intense mixing close to topographic features, recent work from tracer release experiments also suggests that slow mean flows and recirculating eddies trap tracers near topography for long times, increasing the amount of mixing in these hotspots (Mashayek et al., 2017). We have shown in the model that in the ocean interior, there are hotspots of density change at or downstream of topographic features and relative density change is somewhat elevated in regions with high EKE. In reality, water parcels upwelling along major ridges and plateaus are likely to interact with the bottom boundary layer, experiencing more mixing that is not resolved in this model. Thus we hypothesize that topographic hotspots contribute a greater fraction of the total density change in the ocean interior than reported here. Further research using observations and Lagrangian experiments in higher resolution models are necessary to fully determine the role of mixing hotspots in transformation of upwelling deep water.

The transformation of upwelling deep water masses in the Southern Ocean has important implications for the fate of nutrients and carbon, as most of the deep carbon and nutrient reservoir enters the Southern Ocean via the Indian and Pacific. Further work is needed to determine how these upwelling pathways supply natural carbon from the deep ocean to the sea surface and the influence of interior mixing on the pathways and rates.

4.5 Acknowledgments

V.T., R.P.A. and L.D.T. were supported by NSF OCE-1357072. R.P.A. acknowledges support from NSF grant OCE-1357133. MRM is supported by NSF Award PLR-1425989. J.W. acknowledges support from NSF OCE-1234473 and declare that this work was done as a private venture and not in the author's capacity as an employee of the Jet Propulsion Laboratory, California Institute of Technology. We acknowledge high-performance computing support from Yellowstone (`ark:/85065/d7wd3xhc`) provided by NCAR's Computational and Information Systems Laboratory, sponsored by the National Science Foundation, and from the Yeti HPC cluster, provided by Columbia University Research Computing Services. SOSE Iteration 100 model output is available at `http://sose.ucsd.edu`. Lagrangian trajectories used in this paper are available from the corresponding author upon request. The authors Sjoerd Groeskamp and one anonymous reviewer whose comments greatly improved the manuscripts and thank H. Drake and A. Morrison for extensive discussions on the Lagrangian analysis, and I. Cerovečki for useful discussion on water mass transformation.

Chapter Four, in full, is a reprint of the material as it appears in the Journal of Geophysical Research: Oceans. Tamsitt, V., R. P. Abernathey, M. R. Mazloff, J. Wang, and L. D. Talley (2018). Transformation of deep water masses along Lagrangian upwelling pathways in the Southern Ocean *J. Geophys. Res. Oceans*, in press. The dissertation/thesis author was the primary investigator and author of this paper.

Table 4.1: Water mass definitions, showing the neutral density (γ_n) range used in the the same iteration of SOSE in Abernathey et al. (2016), and the equivalent σ_2 ranges for upwelling water in this study. The rightmost three columns show the percentage of total upwelling particles in each density class at the particle release location at 30°S, at the first crossing of the SDL and at the first crossing of the ML.

Water mass	γ_n (kg m^{-3})	σ_2 (kg m^{-3})	% at release	% at SDL	% at ML
IW	27.0 - 27.5	<36.6	8.3	7.2	25.8
UCDW	27.5 - 28.0	36.6 - 36.95	46.6	55.3	50.7
LCDW	28.0 - 28.2	36.95 - 37.2	45.1	37.5	21.4
AABW	>28.2	>37.2	<0.1	<0.1	2.1

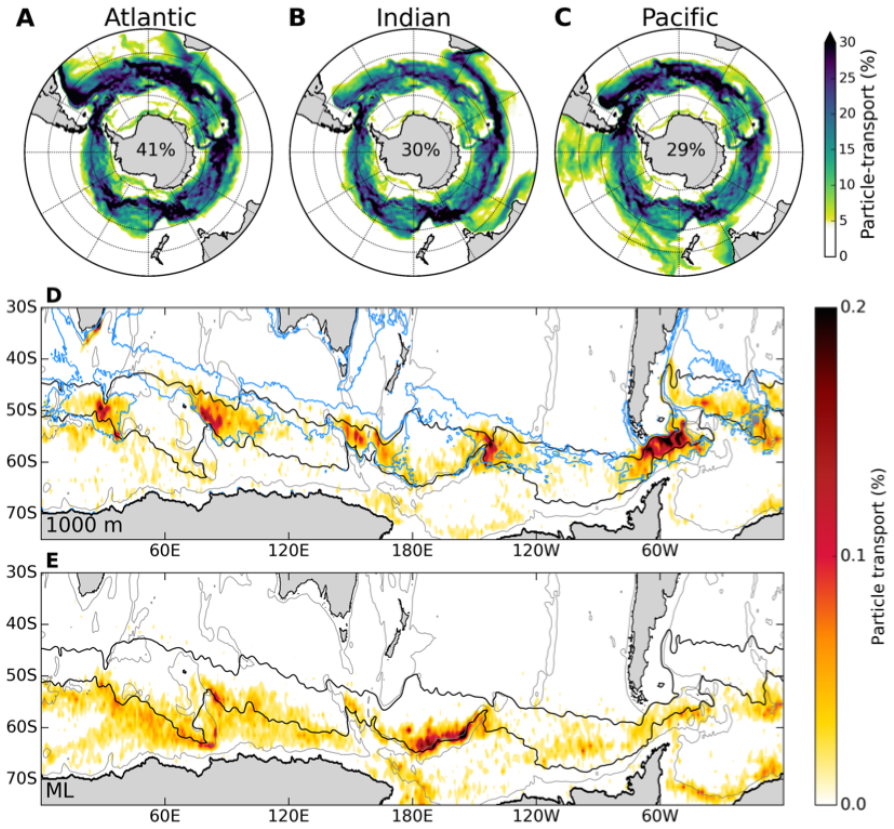

Figure 4.1: Maps of spatial patterns in Lagrangian upwelling in the Southern Ocean State Estimate, based on Tamsitt et al. (2017). Percent of particle-transport passing through each 1° longitude x 1° latitude grid cell at any time between 30°S and the mixed layer for particles originating in the a)Atlantic, b) Indian and c) Pacific; d) Percent of particle-transport crossing 1000 m in each 1° latitude x 1° longitude grid box between release at 30° S and the mixed layer in SOSE. Blue contours indicate regions where the mean surface EKE is greater than 100 cm^2s^{-2}; e) same as d) but for the ML crossing. Numbers on Antarctica in a)-c) show the percentage of the total upwelling particle-transport originating in the Atlantic, Indian or Pacific. Black lines on d) and e) indicate the Northern and Southern boundaries of the ACC, from the outermost sea surface height contours closed through Drake Passage. Grey contours on d) and e) show the 3000 m bathymetry contour, highlighting major topographic features along the ACC.

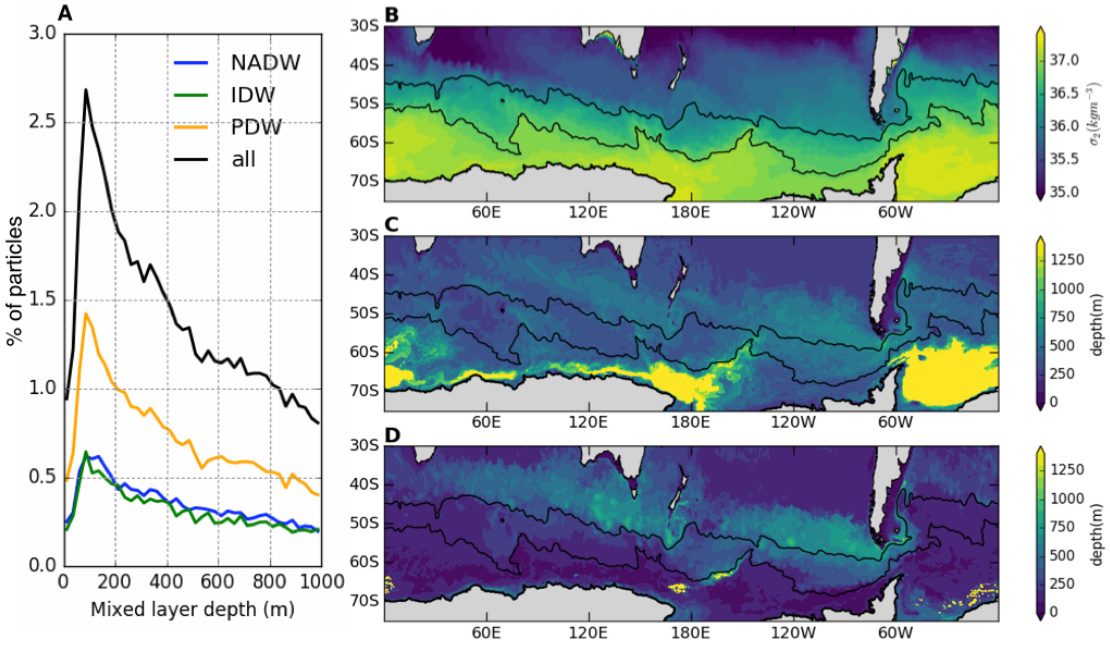

Figure 4.2: a) Distribution of depth of mixed layer at particle first crossings, b) σ_2 of the surface diabatic layer (SDL) at each grid point, c) mean depth of the SDL σ_2 at each grid point and d) depth of the mixed layer "bowl", which is the maximum mixed layer depth at each grid point for the 6-year period.

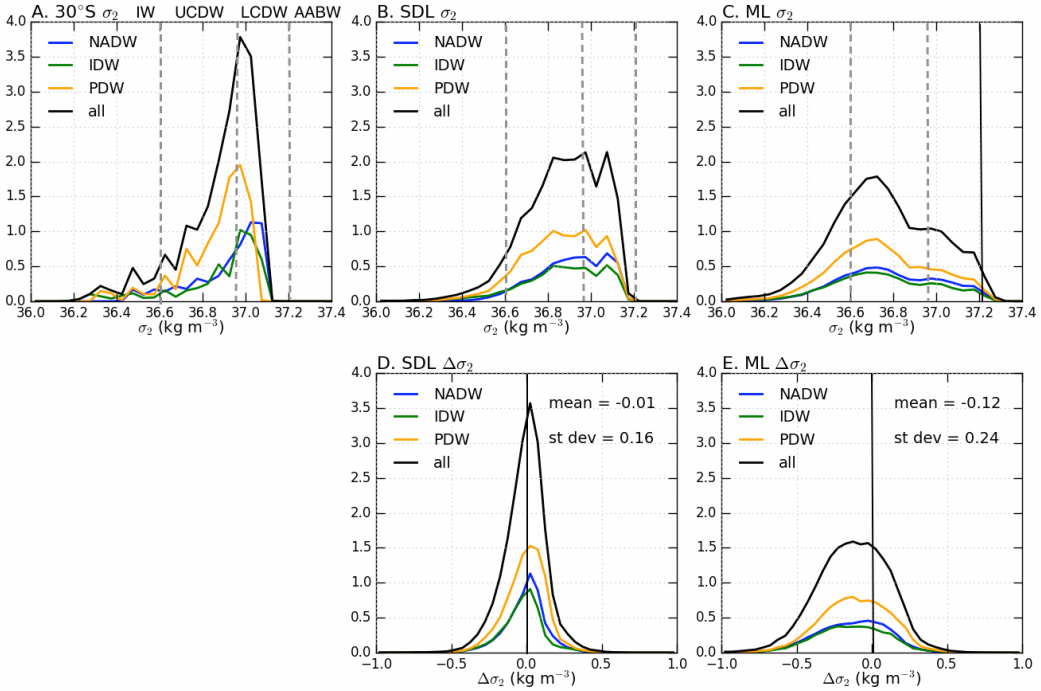

Figure 4.3: Probability density functions of all particles (black) and the contributions to the total PDF from the Atlantic, Indian and Pacific basins (colors) for a) σ_2 at release location at 30°S, b) σ_2 at first crossing of the SDL, c) σ_2 at first ML crossing, d) $\Delta\sigma_2$ at first crossing of the SDL, and e) $\Delta\sigma_2$ at first ML crossing. Dashed lines in a), b) and c) indicate the boundaries between different water masses listed in Table 4.1 and the solid vertical lines in d) and e) indicate 0 $\Delta\sigma_2$, or no density change. The mean and standard deviation of $\Delta\sigma_2$ are shown on panels d) and e).

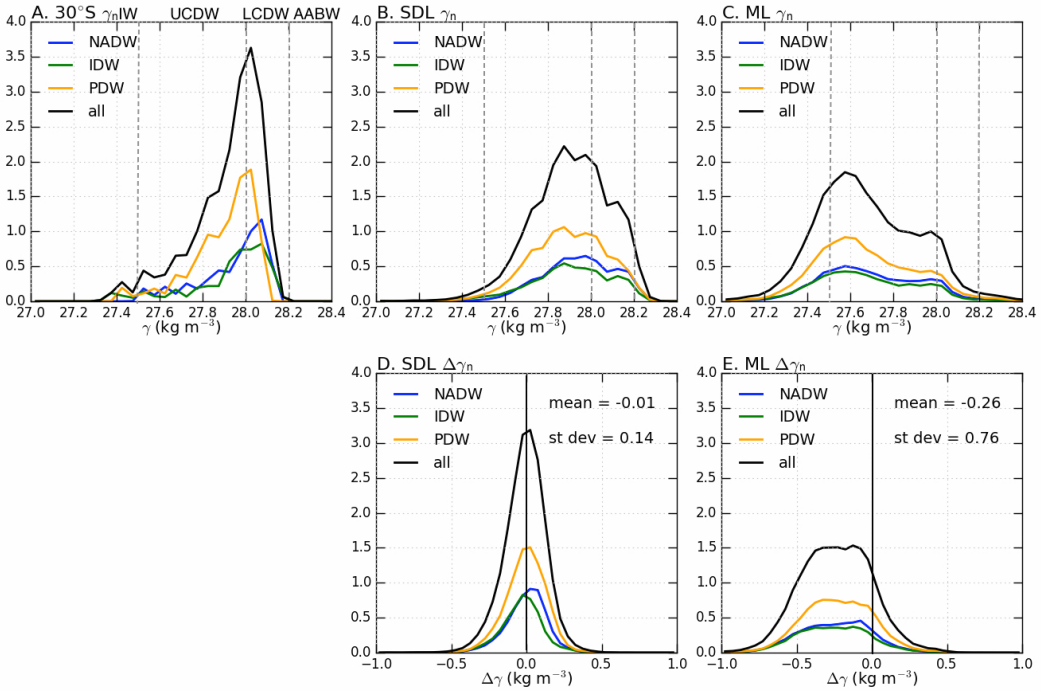

Figure 4.4: Probability density functions of all particles (black) and the contributions to the total PDF from the Atlantic, Indian and Pacific basins (colors) for a) γ_n at release location at 30°S, b) γ_n at first crossing of the SDL, c) γ_n at first ML crossing, d) $\Delta\gamma_n$ at first crossing of the SDL, and e) $\Delta\gamma_n$ at first ML crossing. Dashed lines in a), b) and c) indicate the boundaries between different water masses listed in Table 4.1 and the solid vertical lines in d) and e) indicate 0 $\Delta\gamma_n$, or no density change. The mean and standard deviation of $\Delta\gamma_n$ are shown on panels d) and e).

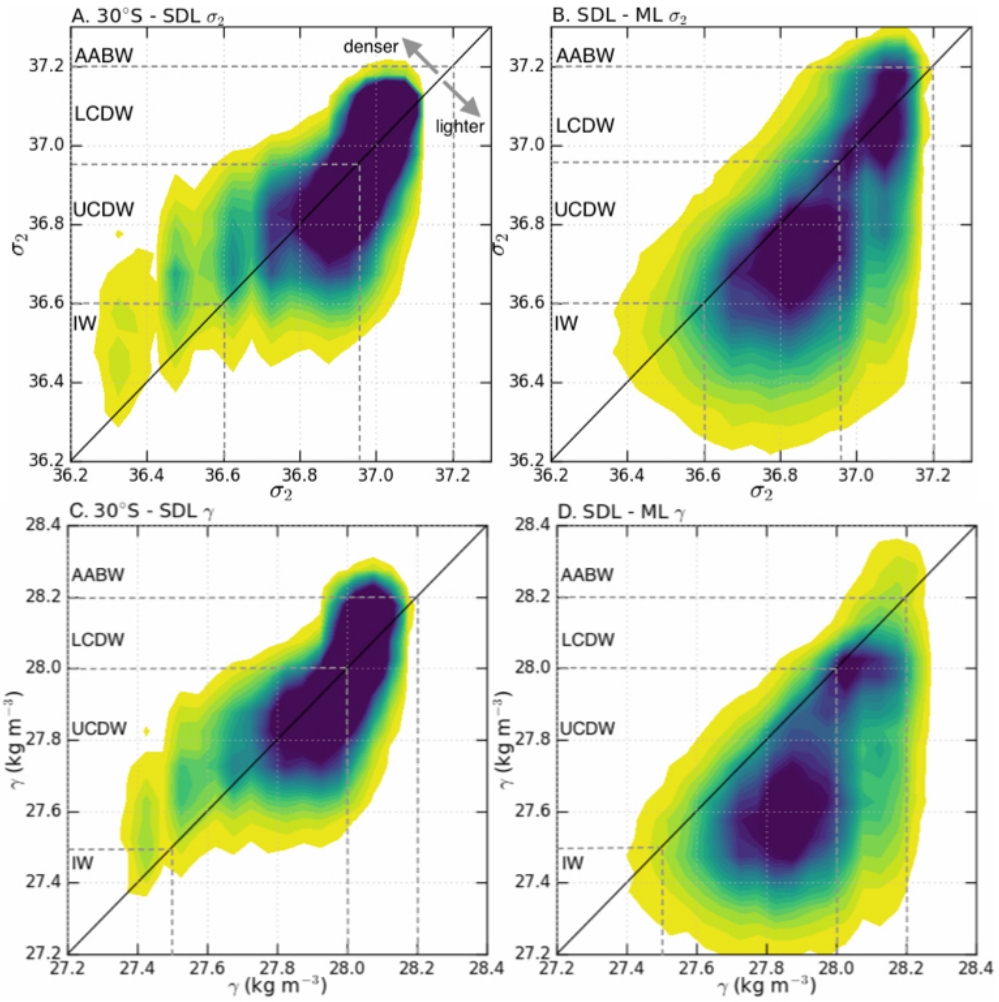

Figure 4.5: Joint probability density function of a) σ_2 at release location at 30°S compared to σ_2 at first crossing of the SDL, b) σ_2 at first crossing of the SDL compared to σ_2 at first crossing of the ML, c) same as a) for γ_n, and d) same as b) but for γ_n. The solid 1:1 line in each panel indicates no density difference, values above the line indicate a density increase, and below the line indicate a density decrease. Dashed lines indicate the boundaries between different water masses in σ_2 and γ_n listed in Table 4.1.

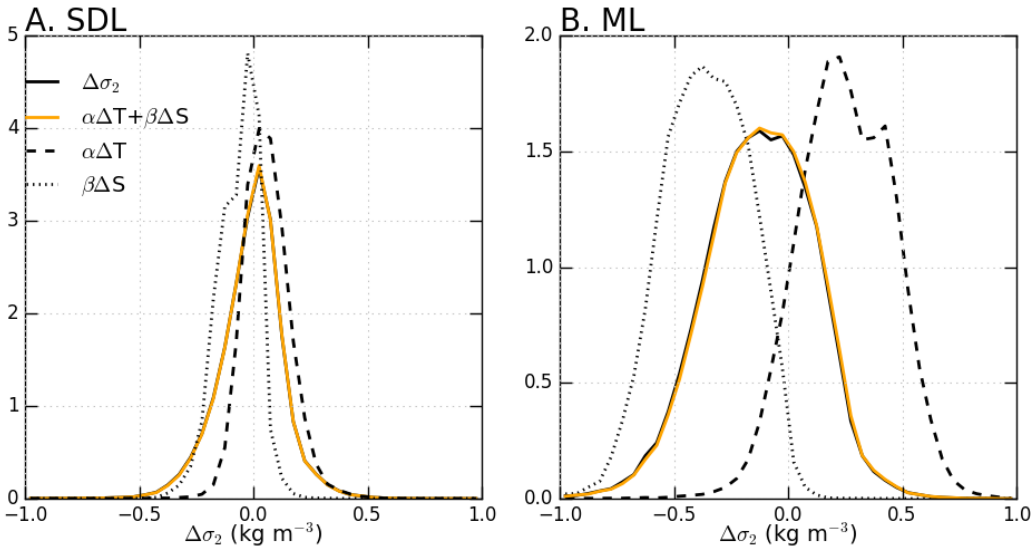

Figure 4.6: Probability distribution function of particle $\Delta\sigma_2$ and contributions from $\Delta\theta$ and ΔS at a) first crossing of the SDL and b) first crossing of the ML. Note that the y-axis limits differ in panels a) and b).

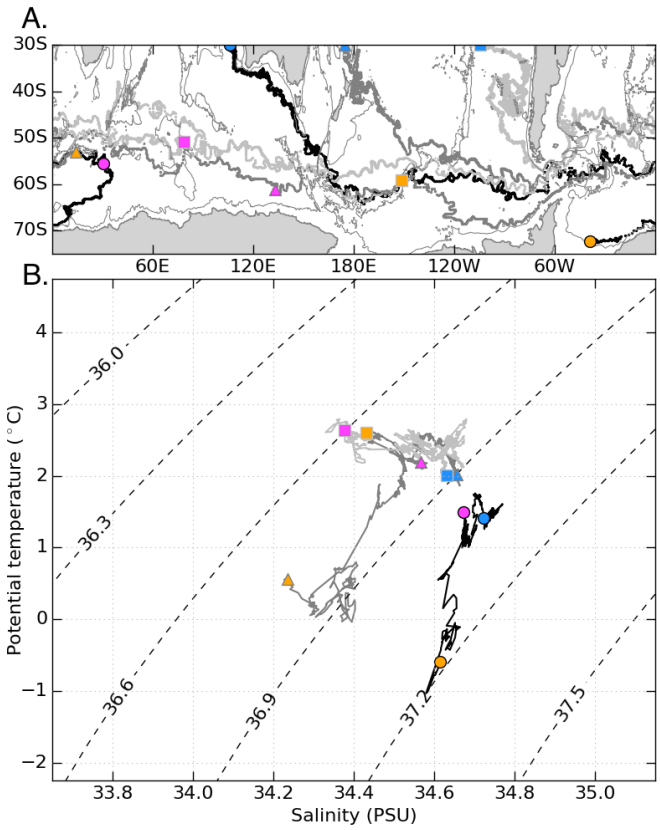

Figure 4.7: Lagrangian trajectories in θ-S space. a) Map showing positions for three particles (black, dark grey and light grey) with colored location at 30°S (blue), first crossing of the SDL (magenta) and first crossing of the ML (orange), and b) same trajectories as a) but in θ-S space. Dashed black contours show σ_2 levels in θ-S space.

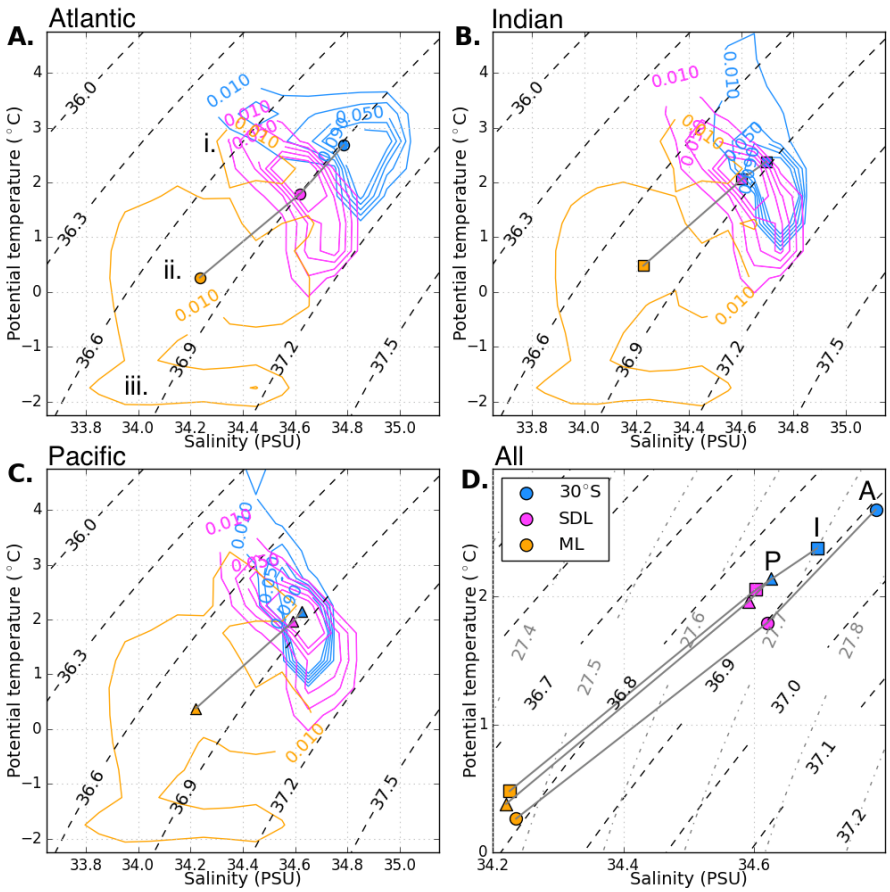

Figure 4.8: Joint probability distribution function of particle θ (°C) and salinity (PSU) at the release location (blue), SDL crossing (magenta) and ML crossing (orange) for a) particles originating in the Atlantic, b) Indian and c) Pacific. Dashed black contours show σ_2 levels in θ-S space. Blue, magenta and orange filled shapes on each panel connected by grey lines show the progression of the mean particle θ-S properties at release, SDL crossing and ML crossing, respectively. d) Zoomed in view of mean particle θ-S properties at release, SDL and ML for the Atlantic (A, circles), Indian (I, squares) and Pacific (P, triangles). Dashed black contours on each panel show σ_2 levels in θ-S space, and dash-dot grey contours on d) indicate σ_θ (potential density referenced to the sea surface) levels in θ-S space.

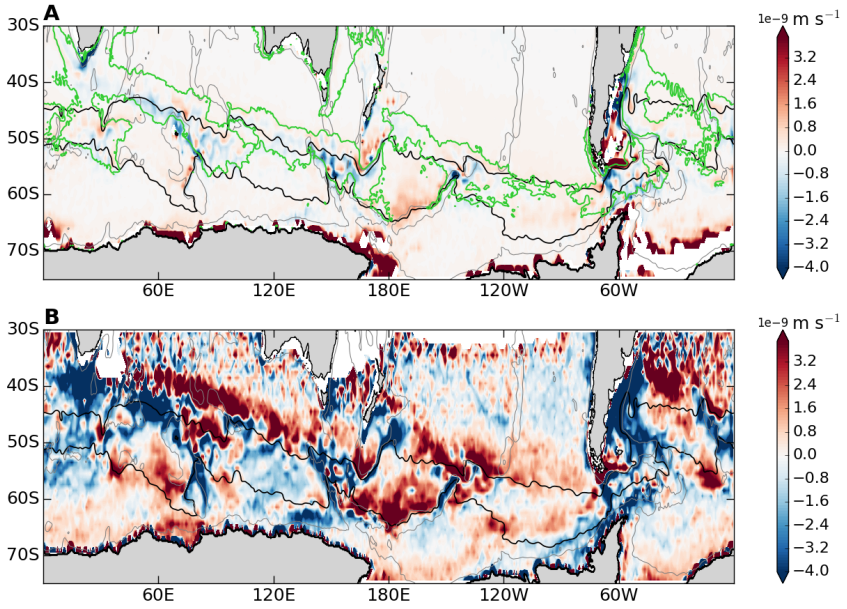

Figure 4.9: Ensemble averaged $d\sigma_2/dt$ in 1° longitude x 1° latitude bins along particle trajectories for a) below the SDL, b) above the SDL (see Fig. 4.2 for SDL density and depth). Only bins containing greater than 100 particle crossings are shown. Positive values (red) indicate increasing density. Green contours indicate regions where the mean EKE at 1000 m in SOSE is higher than 100 cm^2s^{-2}, as in Figure 4.1d.

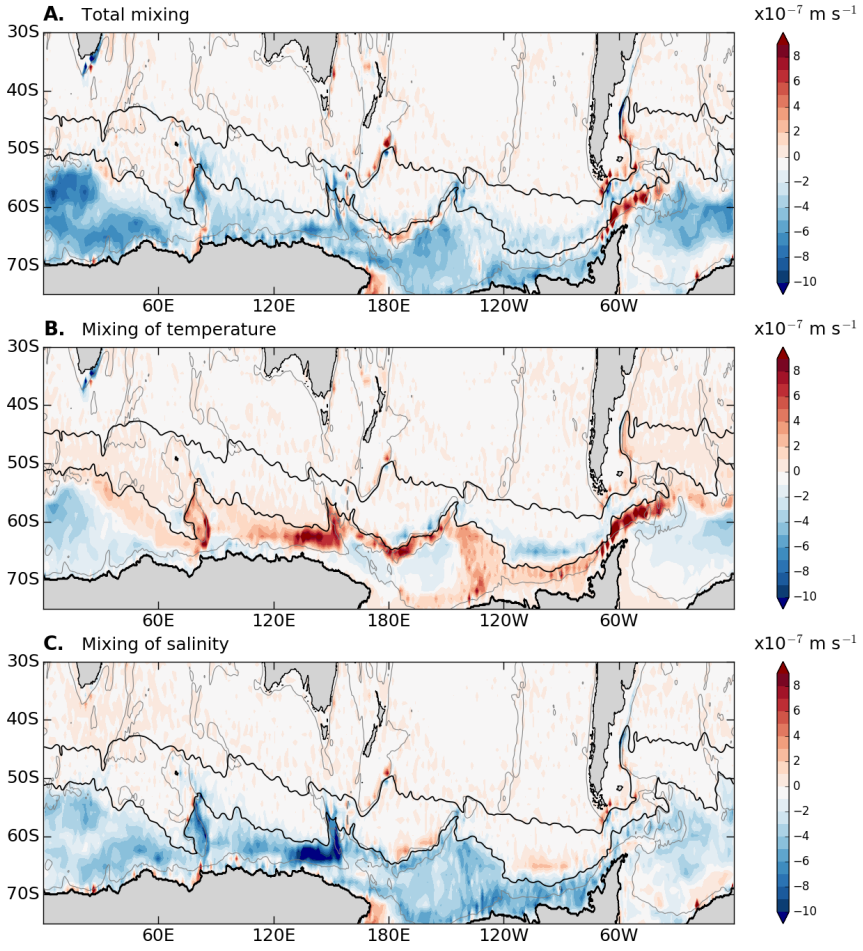

Figure 4.10: Mean water mass transformation (m s^{-1}) across 36.6 kg m^{-3} < σ_2 < 36.8 kg m^{-3} (light UCDW) due to a) total diapycnal mixing, b) diapycnal mixing of temperature and c) diapycnal mixing of salt. Grey contours on d) and e) show the 3000 m bathymetry contour.

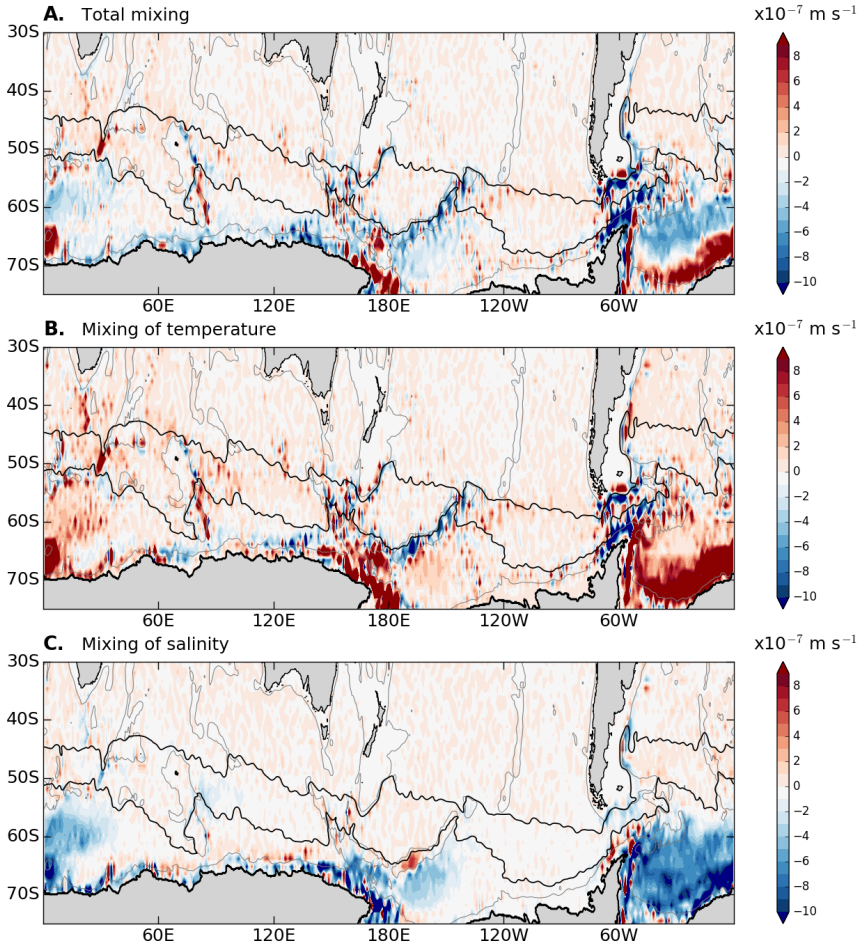

Figure 4.11: Water mass transformation (m s^{-1} averaged across the 37.0 kg m^{-3} < σ_2 < 37.15 kg m^{-3} (LCDW) layer due to a) total diapycnal mixing, b) diapycnal mixing of temperature and c) diapycnal mixing of salt. Grey contours on d) and e) show the 3000 m bathymetry contour.

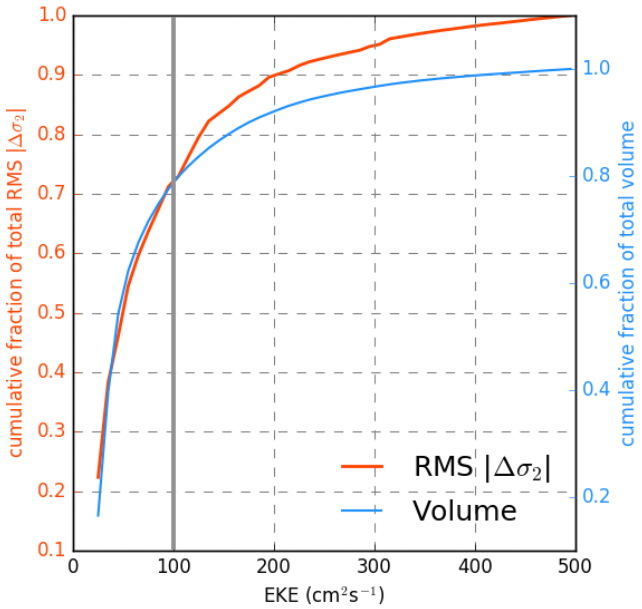

Figure 4.12: Cumulative fraction of total RMS of absolute density change (red), and cumulative fraction of total ocean volume (blue), as a function of EKE. Note that the limits of the two y-axes differ, with the density change y-axis (left) extending from 0 to 1 but the volume y-axis (right) extending above 1 in order to show clearly the alignment of the two curves at low EKE values (<100 cm^2 s^{-2}) and the separation at high EKE values (>100 cm^2 s^{-2}). The heavy grey line at EKE=100 cm^2 s^{-2} emphasizes the point at which the two lines begin to deviate.

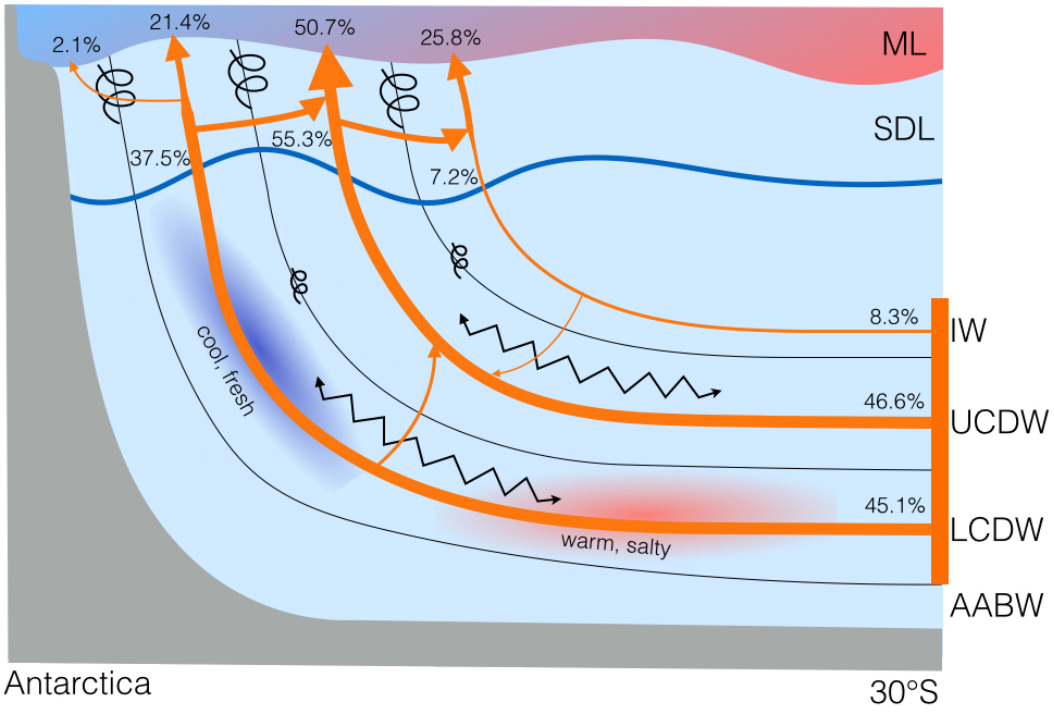

Figure 4.13: Schematic of the fate of upwelling deep water that travels from 30°S to the mixed layer. Grey indicates the seafloor. Black curves indicate the boundary between IW, UCDW, LCDW and AABW density layers. The blue line is the lower boundary of the SDL and shaded region above indicates the mixed layer, with the blue to red gradient indicating the buoyancy gradient in the mixed layer. The orange bar indicates the depth range over which particles were released at 30°S between 1000 m and 3500 m depth, with a total combined upwelling of particles represents 21.3 Sv of transport. Orange arrows indicate pathways of particles from 30°S to the ML in each density class, with wider arrows indicating a larger percentage of the total upwelling, with the corresponding percentage of total upwelling particles shown alongside the arrows at 30°S, the SDL crossing, and ML crossing (as listed in Table 4.1). Black zig-zag arrows indicate isopycnal mixing and black spirals indicate diapycnal mixing (weak in the interior below the SDL and stronger in the SDL). Red and blue shading on the LCDW layer indicate the along isopycnal gradient from relatively warm and salty to relatively cool and fresh.

Chapter 5

An Indian Deep Water boundary pathway south of Australia

keypoints

- Observations and a model confirm the existence of a deep poleward boundary current exiting the Indian Ocean along the southern coast of Australia.
- The pathway transports 14.2 Sv of high-carbon, low-oxygen Indian Deep Water between neutral density 27.7 kg m^{-3} and 28.1 kg m^{-3}, with 13 Sv reaching the ACC.
- The deep transport is highly variable and positively correlated with the overlying westward Flinders Current.

Abstract

Deep boundary currents are the dominant pathway by which deep waters are transported from low to high latitudes. In the Southern Hemisphere, in addition to the Deep Western Boundary Currents, pathways along the eastern boundaries of the southern Atlantic, Indian and Pacific transport deep water poleward into the Southern Ocean

where these waters upwell to the sea surface. These eastern boundary deep water pathways and their physical drivers are not well characterized, particularly those carrying carbon and nutrient-rich deep waters from the Indian and Pacific. Here we describe a poleward, eastern boundary pathway of Indian Deep Water (IDW) along the southern boundary of Australia to the Antarctic Circumpolar Current (ACC). Using a combination of hydrographic observations and Lagrangian experiments in an eddy-permitting ocean state estimate, we find strong evidence for a deep boundary current carrying the low-oxygen, carbon-rich signature of IDW extending between 1500 m and 3000 m along the Australian continental slope, from 30°S to the ACC southwest of Tasmania. From the Lagrangian particles it is estimated that this pathway transports 20 Sv southward at 30°S, with 17 Sv reaching the ACC. The transport of this pathway is highly variable and is closely correlated with the overlying westward Flinders Current. We discuss the role of both eddies and topography in the dynamics of this pathway.

5.1 Introduction

Recent Lagrangian experiments in three eddying ocean models have identified narrow boundary pathways along the western and eastern boundaries of the ocean basins and along major topographic ridges that are responsible for carrying the vast majority of upwelling deep waters from 30°S to the Antarctic Circumpolar Current (ACC) (Tamsitt et al., 2017). The western boundary pathways are, for the most part, well characterized deep western boundary currents (mainly the Brazil Current in the Atlantic and the Agulhas Return Current in the Indian). In the Indian and Pacific, deep water outflows also flow poleward along mid-ocean ridge systems. A third type of poleward flowing deep water pathway exists along the eastern boundary of each basin; however, the dynamics of these eastern boundary pathways are not well understood. There has been

recent progress in characterizing the structure and dynamics of both the eastern Atlantic (Van Sebille et al., 2012) and eastern Pacific pathways (Faure and Speer, 2012), but the eastern Indian pathway remains largely unexplored, due to both a lack of observations and a lack of recognition of this pathway.

The deep Indian Ocean has no northern sources for deep and bottom waters, and thus Indian Deep Water (IDW), characterized by low-oxygen, high nutrients and relatively high salinity, is formed diffusively from abyssal waters via diapycnal mixing in the interior (Talley, 2013a). Along with Pacific Deep Water, IDW is a key source of carbon and nutrient-rich deep water to the upper ocean via Southern Ocean upwelling. Although the volume transport of the outflow of deep water from the eastern Indian Ocean pathway is weaker than in the western Indian (Tamsitt et al., 2017), this route carries the most carbon-rich IDW from the Indian Ocean to the Southern Ocean (see figures in (Key et al., 2004; Talley, 2013b)).

The upper ocean circulation along the western and southern coast of Australia is unusual, but well described: on the continental shelf a seasonally varying, shallow, poleward eastern boundary current (the Leeuwin Current) connects to an eastward flow along Australia's southern shelf (the South Australian Current), before flowing southward west of Tasmania (the Zeehan Current). In the subsurface and somewhat further to the south along the continental slope, a positive wind stress curl drives the westward flowing Flinders Current along the southern Australian continental slope from Tasmania to Western Australia (Bye, 1972; Middleton and Cirano, 2002), connecting to the Leeuwin Undercurrent as it rounds the tip of western Australia and forming the connection of the Southern Hemisphere supergyre (Speich et al., 2002; Ridgway and Dunn, 2007) between the Pacific and Indian Oceans. The Flinders Current, however, is confined to the upper 1000 m, and the deep ocean circulation below this has been largely passed over in observational and modeling studies.

The possible pathways of deep and bottom water flows into and out of the eastern Indian Ocean are heavily constrained by numerous undersea ridges and basins (Mantyla and Reid, 1995). In the Perth Basin, a northward Deep Western Boundary current (DWBC) carrying deep and abyssal waters along the western flank of the Perth Basin at the Broken Plateau is overlaid by a southeastward deep water flow along the eastern side of the basin of the basin close to the Naturaliste Plateau (Toole and Warren, 1993; Robbins and Toole, 1997; Talley and Baringer, 1997; Sloyan, 2006). Integrated transports based on hydrographic sections at 32°S in 1987 and 1995 indicate southward flow in deep layers in the interior and eastern side of Perth Basin (Robbins and Toole, 1997; Talley and Baringer, 1997). In a more recent reoccupation of the same section, McDonagh et al. (2008) estimated 20 Sv of southward transport through the Perth Basin below 2000 m between 90°E and 100°E. Oxygen concentrations are lower in the eastern part of Perth basin between 2000 m - 4000 m, suggesting that southward movement of North Indian Deep Water through the Perth Basin is isolated from the higher salinity, lower oxygen deep waters that enter the Indian from NADW in the western side of the basin (Toole and Warren, 1993). Additionally, a moored current meter array across the Perth Basin below 3200 m shows the lower edge of this southward transport, with approximately 3 Sv of southward mean transport along the eastern boundary of the Perth Basin between 107°E and 110°E (Sloyan, 2006).

Hufford et al. (1997) identified a boundary-intensified deep eastward flow from hydrographic data along 115°E at the southwest tip of Australia, underlying the westward flowing Flinders Current (Bye, 1972; Middleton and Cirano, 2002) and were the first to suggest this may be connected to the upstream southeastward flow rounding the southwest corner of Australia. This finding is supported by ADCP data from the same hydrographic sections, which indicate the deep eastward flow below 2000 m extending 300 km southward from the Australian coast (McCartney and Donohue, 2007). Further

downstream in the Great Australian Bight, hydrographic sections show a deep oxygen minimum along the southern edge of the Australian continental shelf, consistent with the presence of deep water of Indian origin. However, inverse analysis of these data did not identify a significant eastward flow of deep water (Schodlok et al., 1997; Schodlok and Tomczak, 1997).

The scarcity of observations of deep ocean properties and velocities south of Australia has hindered investigation into the structure of this deep boundary current and its downstream connection to the ACC. However, recent evidence from eddying models shows the importance of this pathway for upwelling of deep waters from the Indian Ocean to the ACC (Tamsitt et al., 2017; Drake et al., 2018), indicating this is a previously unrecognized key route for delivering carbon-rich deep water to the surface of the Southern Ocean.

In this work we provide a detailed description of the IDW pathway structure, transport and variability along the southern coast of Australia, and investigate dynamics of this deep boundary current. In section 5.2, we describe the hydrographic data, model and Lagrangian analysis. In section 5.3.1 we describe the structure and properties of the pathway; in 5.3.2 we characterize the transport and variability of the deep pathway. Our results are summarized and discussed in section 5.4.

5.2 Data and Models

5.2.1 Observational data

We analyze high-quality, full depth hydrographic data from one zonal (32°S) and three meridional (115°E, 120°E and 132°E) sections that transect the IDW pathway between the southern Indian Ocean and the ACC (Fig. 5.1). The I05 section data used in this analysis wer collected in 2009, I09S in 2004, and S05 in 1994 (Schodlok

et al., 1997; Schodlok and Tomczak, 1997). Hydrographic data from the I05, I09S, and S05 cruises were obtained from the CCHDO (http://cchdo.ucsd.edu/). I05 and I09S were collected and made publicly available by the International Global Ship-based Hydrographic Investigations Program (GO-SHIP;http://www.go-ship.org/) and the national programs that contribute to it. Data from all sections include CTD and bottle salinity, oxygen, nitrate and silicate. The I05 and I09S sections also include dissolved inorganic carbon (DIC). Other parameters measured at these stations are not used in this analysis.

In addition to ship-based CTD data, we also make use of an APEX Deep Argo float deployed south of Australia as part of the Southeast Indian deep Argo pilot array (Fig. 5.1). The deep float was deployed in November 2016 at 34.5°S, 106.4°E and collected 81 full depth profiles between November 2016 and December 2017, drifting at a parking depth of 3000 db and profiling to the surface every 5 days. The float surfaced in emergency mode due to a leak in January 2018 but has not been recovered. The remaining eight deep floats in this region are in the deeper part of the South Australian Basin away from the Australian boundary and have a deeper parking depth in abyssal waters, and thus the trajectories are not relevant to this pathway.

5.2.2 Model and Lagrangian analysis

The Southern Ocean State Estimate (SOSE, sose.ucsd.edu) is an eddy-permitting ocean-ice model based on the MITgcm (Mazloff et al., 2010). SOSE spans 24.7°S to 78°S with an open northern boundary, with 1/6° horizontal resolution and 42 uneven vertical levels. SOSE assimilates the majority of available in situ observations using an adjoint method with software developed by the consortium for Estimating the Climate and Circulation of the Ocean (ECCO; http://www.ecco-group.org). Initial and northern open boundary conditions are determined using a 1° global state estimate (Forget, 2010). The atmospheric state is initialized using the ECMWF ERA-interim global reanalysis

(Dee et al., 2011). For this analysis we use SOSE iteration 100, which includes 6 years of daily model state for the years 2005 - 2010. The SOSE iteration 100 solution has been extensively validated against observations (Abernathey et al., 2016; Tamsitt et al., 2017).

Lagrangian particle tracking experiments were conducted with SOSE iteration 100 daily averaged velocity output using Octopus (github.com/jinbow/Octopus) as described in Tamsitt et al. (2017) and Tamsitt et al. (2018). Particles were re-released at 30°S between 1000 m and 3500 m depth every 30 days for 6 years, and tracked for 200 years by looping the SOSE velocity output. The particle position, temperature, salinity and neutral density are recorded along particle trajectories every 5 days. We only analyze particles with initial southward release velocities, and further subset the particles to focus on those that remain south of 30°S and upwell to the mixed layer within 200 years. The mixed layer is defined in SOSE at each location and time using the second derivative of density to find the inflection point at which $\partial\rho/\partial z$ switches sign.

5.3 Results

5.3.1 Deep pathway structure and properties

Figure 5.1 shows the pathway of upwelling deep water Lagrangian particles from the eastern Indian Ocean at 30°S to the ACC. Particles first travel southeastward from the Perth Basin through the gap between the Naturaliste and Broken Plateaus, before hugging the Australian continental slope, flowing eastward through the South Australian Basin and then southward west of Tasmania before reaching the northern boundary of the ACC. There is a secondary weaker 'short-circuit' pathway that splits off from the main pathway at 120°E and travels southward across the South Australian Basin, reaching the ACC close to the Australian-Antarctic Discordance. This path differs from the

main pathway as it is no longer associated with the continental boundary and overlying Flinders Current, although it appears it may be somewhat related to the topography along the western edge of the South Australian Basin, as can be seen from the 5000 m isobath in Figure 5.1. The median timescale for deep upwelling particles to travel from 30°S to the northern ACC boundary is 40 years, and 116 years to travel from 30°S to the mixed layer.

The initial southward particle-transport between 1000 m and 3500 m at 30°S is 19.9 Sv, 17 Sv of which reaches the northern ACC boundary (defined as the northernmost mean sea surface height contour that is closed through Drake Passage). Of the 19.9 Sv southward transport, 1.8 Sv upwells to the mixed layer within 200 years, 16.6 Sv travels north of 30°S within 200 years and the remaining 1.5 Sv remains in the Southern Ocean below the mixed layer at the end of the experiment. We apply an additional density criteria to the particles and find the initial southward particle-transport between neutral densities 27.7 kg m^{-3} and 28.1 kg m^{-3} is 14.2 Sv, with 13 Sv reaching the northern ACC boundary. A total of 8.5 Sv of this transport reaches the northern ACC boundary in the main pathway west of Tasmania, 2.4 Sv in the 'short-circuit' pathway between 120°E and 130°E and the remaining 2.1 Sv is spread throughout the remaining sections of the northern ACC boundary.

The APEX Deep float trajectory, which gives an approximate Lagrangian trajectory at a fixed pressure (3000 db), is consistent with the south-eastward Lagrangian pathway found in SOSE (Fig. 5.1). The float was relatively stationary while trapped in an eddy from November 2016 until July 2017, before traveling eastward for the reminder of 2017. We note that there is significant error associated with the float trajectory as a result of the float surfacing every 5 days, thus we have not attempted to estimate a velocity at 3000 db from the float displacements.

We look at the vertical structure of the pathway in SOSE at the four cross sec-

tions (one zonal and three meridional) that are co-located with historic ship-based hydrographic sections. The vertical extent of the Lagrangian pathway is similar at each section crossing (Fig. 5.2), spanning the range from approximately 1500 m to 3000 m depth, with the highest probability of particle crossings at 2000 m depth. The pathway at these depths corresponds to the neutral density range 27.7-28.1 kg m^{-3}, with a median of 27.9 kg m^{-3} and mode (peak) at 28.0 kg m^{-3}. Neutral density, temperature and salinity characteristics are mostly unchanged along particle trajectories between 30°S and the northern ACC boundary (not shown), indicating that there is weak water mass transformation along this deep pathway.

The time-mean SOSE velocity fields at I05 show a generally broad southward flow extending the full zonal width between the Broken and Naturaliste Plateaus, between 1200 m to 3000 m depth (corresponding to neutral densities 27.7 kg m^{-3} to 28.1 kg m^{-3}), with some intensification on the eastern edge of the section (Fig. 5.2a). This is consistent with eastern-intensified southward transport estimates from observations (Sloyan, 2006; Robbins and Toole, 1997; Talley and Baringer, 1997). Once the flow rounds the corner and heads east, it is more closely confined to the coast. There is a mean eastward flow along the Australian continental slope below 2000 m at I09S, with a strong westward mean Flinders Current above (Fig. 5.2b). There is also a second core of eastward flow further offshore extending to 38°S with a peak at 37°S extending over all depths, and aligning with the peak in Lagrangian particle crossings at 2000 m depth. The mean velocity structure is very similar at S05 120E (Fig. 5.2c), again with two cores of deep eastward flow. However, further downstream at 132E (Fig. 5.2d) the eastward flow is much narrower, confined to the region between 36°S and the continental slope; the westward Flinders Current no longer lies above the eastward deep flow but is instead located farther inshore in shallower water.

Observed deep water property distributions of oxygen and DIC (Fig. 5.3,5.4)

support that the pathway is supplied by southward flow of low-oxygen, carbon-rich subtropical IDW. At the I05 section, the oxygen minimum occurs around 1500 m depth, extending zonally between the Broken and Naturaliste Plateaus. At the three meridional sections (I09S, S05 120E and S05 132E) the oxygen minimum is strongest to the north at the Australian continental slope, with the lowest oxygen concentrations around 2000 m. The distribution of Lagrangian particle crossings at each section show a correspondence between the depth of the peak in particle crossings and the oxygen minimum, although at I05 and I09S the peak of particle crossings is slightly deeper than the core of the oxygen minimum. Distributions of nutrients (not shown) show a similar signal to oxygen, with high nutrient concentrations occurring at the same locations as oxygen minima.

Distributions of DIC (Fig. 5.4) are available at the I05 and I09S sections, and show the high DIC signature of IDW at 2000-4000 m, with a greater depth extent of high DIC occurring on the eastern edge of the I05 section, and high DIC concentrated close the continental slope coinciding with the zonal particle crossings at the I09S section.

Figure 5.5 shows the geographic structure of the mean wind forcing and ocean characteristics from SOSE in the region of the deep boundary pathway. Weak westerly winds along the southern Australian coast increase toward the south, leading to positive wind-stress curl throughout the region (Fig. 5.5a). This positive curl drives an equatorward Sverdrup transport, which due to PV conservation constraints leads to the westward flowing Flinders Current that lies above the deep flow described here (Middleton and Cirano, 2002). The mean velocity in the IDW layer (neutral density 27.7 kg m^{-3} to 28.1 kg m^{-3}) clearly shows the two cores of eastward flow in this density class, one closely following the Southern Australian coast and the second further offshore, with mean speeds of around 1.5 cm s^{-1} (Fig. 5.5b). There are several regions of elevated eddy kinetic energy (EKE) along the pathway, most notably along the southwest corner of Australia (Cresswell and Griffin, 2004; Middleton and Bye, 2007) and in the 'Tasman

leakage' region southwest of Tasmania (Speich et al., 2002) (Fig. 5.5c).

We calculate the mean potential vorticity (PV) in the IDW neutral density layer (27.7 - 28.1 kg m^{-3}, boundaries shown in Fig. 5.2) in SOSE as PV = $-\frac{1}{\rho}\frac{d\rho}{dz}(f+\zeta)$, where ρ is the mean density of the layer, f is planetary vorticity, ζ is relative vorticity $\frac{\partial v}{\partial x} - \frac{\partial u}{\partial y}$. PV is conserved along the flow in the deep ocean circulation away from sources and sinks of PV (Fig. 5.5d). The Lagrangian pathway follows PV contours for the most part, but crosses mean PV contours in some locations, notably west of Tasmania where the pathway is meridional. Because PV is not conserved, this indicates that diapycnal and/or isopycnal diffusion are important for the PV balance in this location, which also coincides with a region of high EKE as part of the East Australian Current (EAC) rounds the southern tip of Tasmania (Fig. 5.5c,d).

5.3.2 Transport and variability

We estimate the zonal transport above and below 1500 m at the I09S section in SOSE and compare these with the observational estimates of Hufford et al. (1997) (Table 5.1). The time-mean westward transport in SOSE in the Flinders Current at I09S in the upper 1500m and north of 37°S is 10 Sv westward, with a standard deviation of 5 Sv. This is weaker than the estimated 22 Sv westward in the same depth and latitude range estimated from a summer hydrographic section by Hufford et al. (1997), although the SOSE transport does occasionally exceed 20 Sv. Below 1500m, the eastward flow north of 37°S is 5 Sv (4 Sv standard deviation), in close agreement with the 5 Sv estimate of Hufford et al. (1997). We note that the 37°S boundary excludes some of the deep offshore eastward transport in SOSE (Fig. 5.2b). These transports also compare well with 4 Sv of eastward flow in this deep boundary current estimated from ADCP data along I09S (McCartney and Donohue, 2007). Averaging SOSE transport by season shows marginally stronger westward transport in the Flinders Current in Austral spring

(September, October, November) and stronger eastward transport in the deep pathway in winter, with a winter mean of 7.7 Sv (compared to 4.3, 4.7 and 4.3 in Spring, Summer and Autumn, respectively).

There is large temporal variability in the eastward flow, with intermittent southward/eastward velocities in the IDW density layer at the zonal/meridional sections (Fig. 5.6). Hovmöller plots of the velocity averaged in the IDW neutral density layer show that at the I05 section there is indication of westward propagation of velocity anomalies, and at I09S there is evidence of northward propagation (Fig. 5.6a,b). This is also somewhat visible at S05 132E.

There is a strong positive correlation between daily averaged zonal transport in the upper ocean (from the surface to γ=27.7 kg m^{-3}) and in the IDW layer (27.7 - 28.1 kg m^{-3}) at all three zonal sections close to the Australian continent (north of 37°S at I09S and north of 36°S at S05 120E and 132E, with correlation coefficients of 0.83, 0.77 and 0.73 for I09S, S05 120E and S05 132 E, respectively. There is no significant correlation between the upper ocean and IDW layer meridional transports at I05. There are not significant correlations between the local wind stress and wind stress curl and upper ocean and deep ocean transports at each section, indicating that the variability is not primarily driven by local wind variability.

To gain further insight into the IDW layer transport variability, we decompose the zonal IDW layer transport into a mean and eddy component at the I09S, S05 120°E and 132°E sections using the decomposition $\overline{u'h'} = \overline{uh} - \overline{u}\,\overline{h}$, where u is the zonal velocity in the IDW layer, the over bar denotes a time mean, and prime denotes a deviation from the time mean. The eastward transport is dominated by the mean component, with a weak westward eddy component opposing the mean transport. The section integrated (integrated north of 38°S to the continental slope) mean component ($\overline{u}\,\overline{h}$) of zonal transport is 3.27 Sv, 3.59 and 1.74 Sv at I09S, S05 120°E and S05 132°E, respectively. The

corresponding eddy components ($\overline{u'h'}$) are -0.02 Sv, -0.03 Sv and -0.04 Sv.

5.4 Discussion and Conclusions

Here we have presented the first detailed description of the structure and variability of a poleward deep ocean boundary current exiting the Southeast Indian Ocean at depths spanning 1200 m to 3000 m. Modeled Lagrangian trajectories in the Southern Ocean State Estimate show a pathway connecting Indian Deep Water to the Southern Ocean via the southern coast of Australia, which is consistent with ship-based hydrographic property distributions that show the pathway carries the low oxygen, high DIC signature of subtropical Indian Deep Water. A deep float trajectory also provides in situ evidence for this deep pathway. Our analysis of the Southern Ocean State Estimate shows that the structure of this pathway is somewhat complex, with a component of eastward flow along the Australian continental slope underlying the westward Flinders Current, and a second core of eastward flow offshore. There is large eddy variability in the transport in the deep boundary current that is correlated to the variability in the Flinders Current above.

With the current dearth of observations of the deep ocean in this region, it is challenging to further characterize the variability of this pathway on various timescales and to determine biases in model representation of the deep boundary flow. The SOSE results indicate there is substantial interannual variability in the circulation: however, the 6-year time series is insufficient to fully characterize this, so a longer model output would be useful for further investigating variability on longer timescales. Additionally, there is complex spatial structure in this deep water pathway that has not been fully explored. Most notable is the 'short-circuit' separating from the boundary pathway and traveling southeastward to the ACC between 120°E and 130°E (Fig. 5.1). While

our Lagrangian results indicate that this branch of the pathway transports a significant amount of deep water to the ACC (2.4 Sv) we have not looked further into the structure and variability of this path.

While we have presented a detailed description of the deep boundary current, there is further work needed to determine the dynamical explanations for its existence, as well as for deep poleward boundary flows at other eastern boundaries. Hufford et al. (1997) suggested that Stommel-Arons upwelling-driven abyssal circulation may explain the zonal deep boundary current along the Southern Australian coast, as the eastward flow is required to join together the interior southward deep water flows west of mainland Australia and west of Tasmania. However, this simple interior circulation budget constraint does not explain the intensification at the boundary.

There are potential dynamical analogies to the poleward flowing eastern boundary pathways that also exist in the South Atlantic and Pacific Ocean (Tamsitt et al., 2017). In the Southeast Atlantic, an analysis of the Potential Vorticity (PV) budget has suggested that the poleward pathway of North Atlantic Deep Water along the eastern boundary is driven by an eddy thickness flux from the overlying Agulhas rings eddy transport (Van Sebille et al., 2012). The Agulhas rings present a unique situation; however, a similar, albeit weaker, westward eddy track exists around the southwest corner of Australia (Cresswell and Griffin, 2004), which suggests that eddy PV fluxes could also play a role in the Indian pathway. Additionally, the lack of an IDW pathway along the southern coast of Australia in Lagrangian experiments using non eddy-resolving velocities from the GFDL model suite indicates that eddy dynamics are necessary for this pathway (Drake et al., 2018). In the southeast Pacific eastern boundary poleward pathway of Pacific Deep Water, there are regions where the PV balance is non-conservative. In these locations isopycnal PV stretching dominates over diapycnal diffusion of PV, suggesting the Stommel-Arons (diapycnal) balance is not the main PV regime (Faure

and Speer, 2012).

The PV distribution in the IDW layer indicates that PV is largely conserved along the pathway, apart from the southward flow west of Tasmania, where high EKE indicates that eddy PV fluxes may play a role in the PV budget in this location. A full analysis of the PV budget in this region would be valuable and is the subject of future work. In addition, there is an important northward outflow pathway of Antarctic Bottom Water that enters the South Australian Basin from the south before passing northward between the Broken and Naturaliste Plateaus (Sloyan, 2006). The interaction of this abyssal Antarctic Bottom Water pathway with the overlying deep water pathway should be explored in future work.

This work presents an important contribution to characterizing the deep ocean circulation in an under-observed region. Our results indicate that deep flows at eastern boundaries are more important for the deep ocean circulation and meridional exchange of carbon and nutrients than previously understood, but are not well characterized. Future growth of deep ocean observing systems and analysis of more sophisticated ocean models will continue to close this gap in understanding.

5.5 Acknowledgments

V.T. and L.D.T were supported by NSF OCE-1357072. M.R.M. is supported by NSF PLR-1425989. Argo data were collected and made freely available by the International Argo Program and the national programs that contribute to it. (`http://www.argo.ucsd.edu`, `http://argo.jcommops.org`). The Argo Program is part of the Global Ocean Observing System.

Chapter Five is currently being prepared for submission for publication of the material by Tamsitt, V., L. D. Talley and M. R. Mazloff (2018), An Indian Deep Water

Pathway South of Australia. The dissertation author was the primary investigator and author of this material.

Table 5.1: Comparison of transports between 37°S and the Australian continent at the I09S section from SOSE and other model and observational estimates.

Source	north of 37°S <1500 m	north of 37°S >1500 m	net
Hufford et al. 1997	-22	5	-17
Middleton and Cirano 2002	-	-	-16
SOSE 2005-2010 mean	10	-5	-5

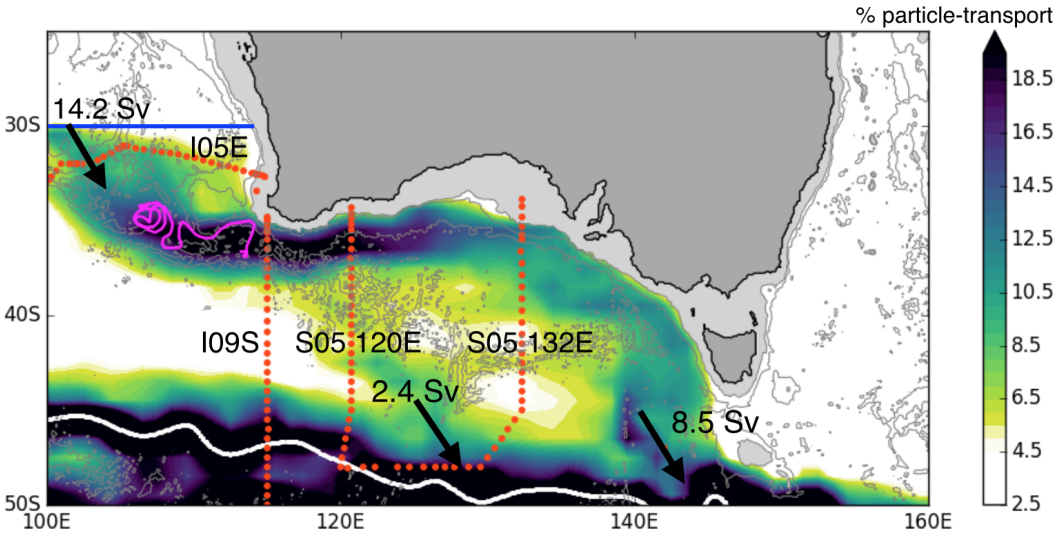

Figure 5.1: Map of the Indian Deep Water pathway from 30°S in the Indian Ocean to the ACC along the southern coast of Australia. The percent of total Indian upwelling particle-transport visiting each 1° latitude x 1° longitude grid column at some time during the 200 year experiment from release at 30°S and before reaching the surface mixed layer (note that high probabilities occur upstream in the ACC because particles perform loops of the ACC during upwelling). The blue line shows the location of particle release at 30°S, red dots indicate the location of hydrographic stations from four sections (I05, I09S, S05 120E and S05 132E) used in this analysis, the magenta line shows the trajectory of the deep Argo float, the white line indicates the northern boundary of the ACC (defined as the outermost sea surface height contour closed through Drake Passage), and black arrows and values indicate the total southward particle-transport at 30°S and reaching the northern boundary of the ACC via the two major pathways. Light grey shading indicates the 1500 m isobath and light grey contours show the 3000 m and 5000 m isobaths.

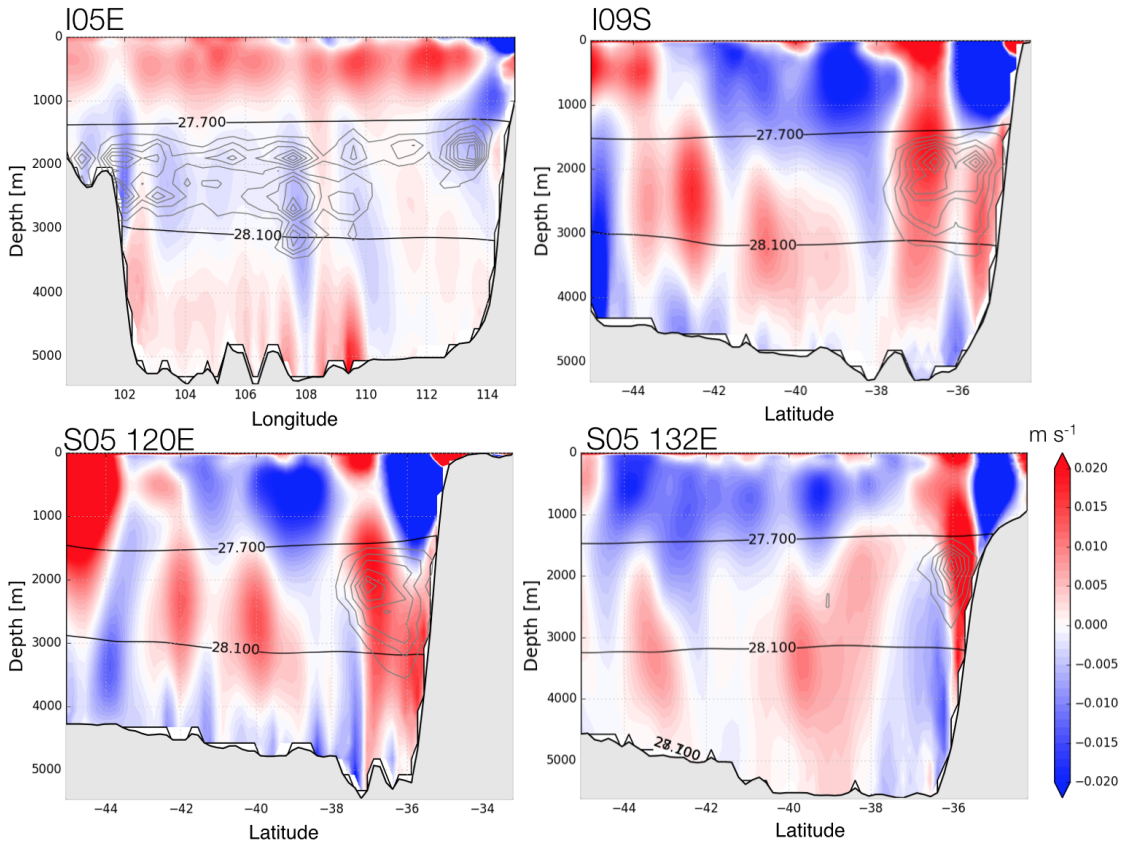

Figure 5.2: SOSE mean a) meridional velocity at I05 and zonal velocity at b) I09S, c) S05 120E, and d) S05 132E. Black lines approximate the neutral density boundaries of the IDW layer, which are used to calculate transport in the IDW density neutral density layer. Gray contours in each panel show the percent of Lagrangian particle-transport of the first time particles cross the section.

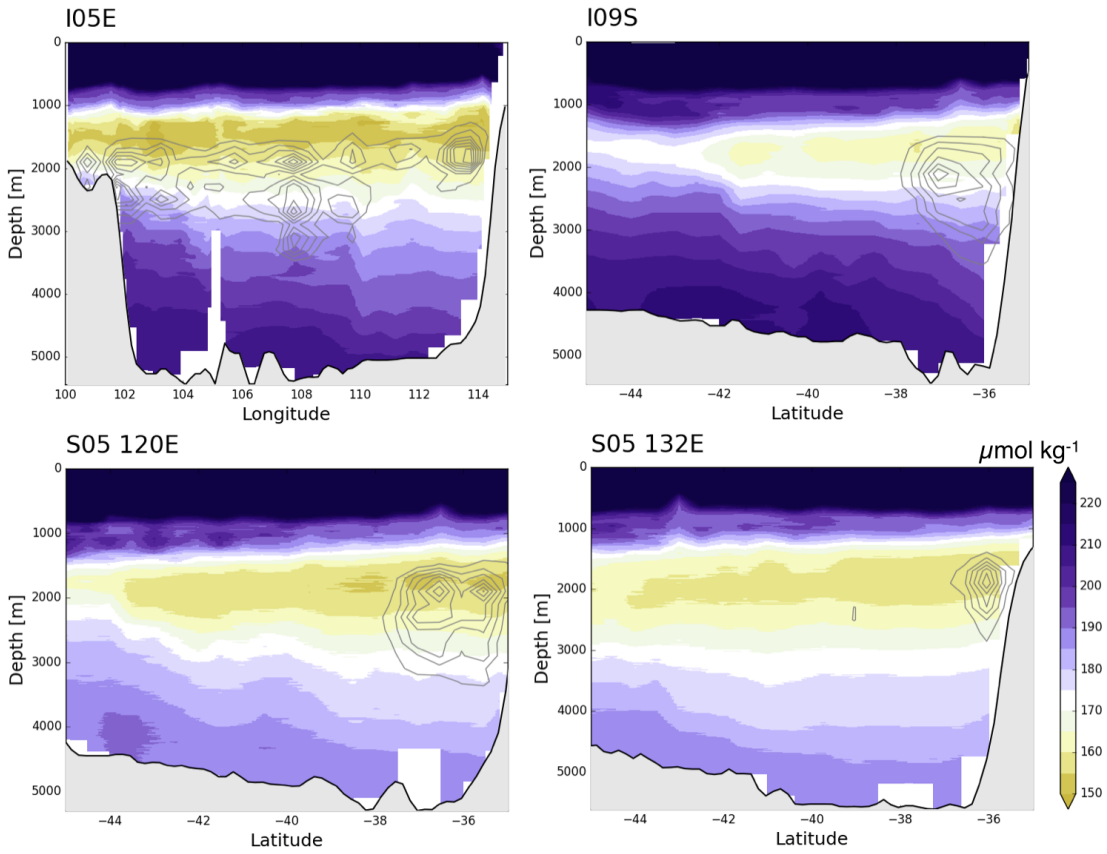

Figure 5.3: Hydrographic sections of dissolved oxygen concentration (μmol kg^{-1}) along the IDW pathway. Black lines approximate the neutral density boundaries of the IDW layer. Gray contours in each panel show the percent of Lagrangian particle-transport of the first time particles cross the section.

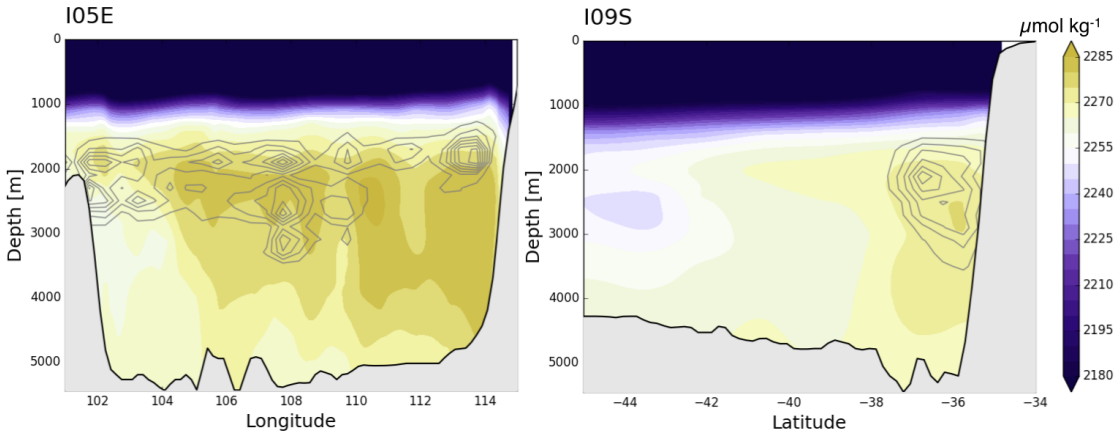

Figure 5.4: Hydrographic sections of total dissolved organic carbon (μmol kg^{-1}) along the IDW pathway. Black lines approximate the neutral density boundaries of the Indian Deep Water layer. Gray contours in each panel show the percent of Lagrangian particle-transport of the first time particles cross the section.

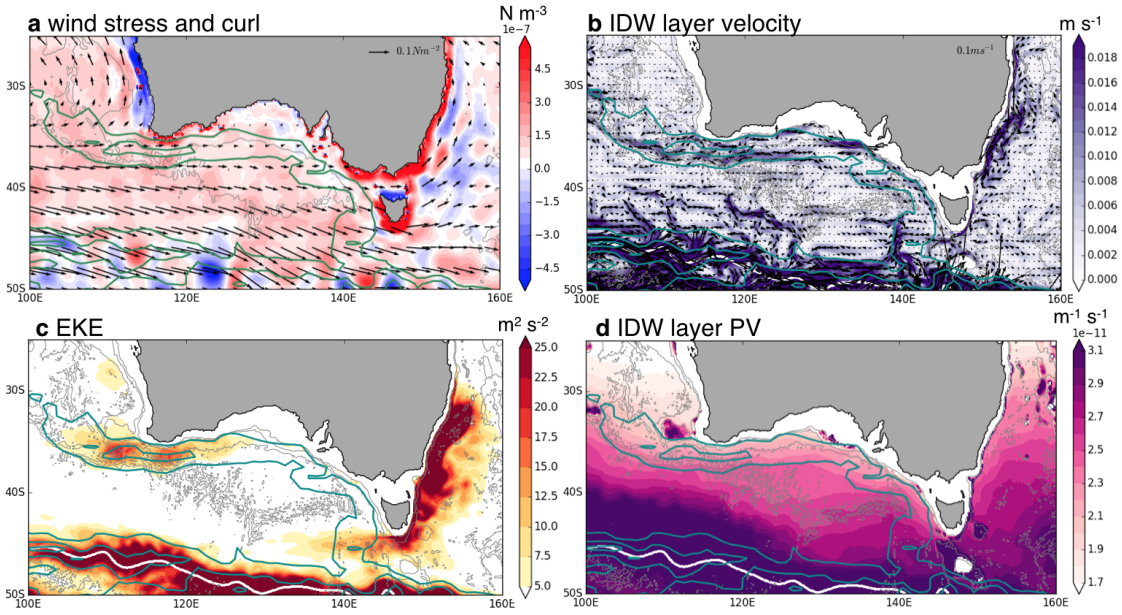

Figure 5.5: SOSE 6-year mean a) wind stress (arrows) and wind stress curl (color) , b) mean velocity vectors (arrows) and speed (color) in the IDW neutral density layer, c) surface eddy kinetic energy, and d) potential vorticity averaged in the IDW neutral density layer. Dark green contours on all four panels indicates the pathway of Lagrangian particles from 30°S by outlining the region where 5% of particle-transport passes through between 30°S and the mixed layer.

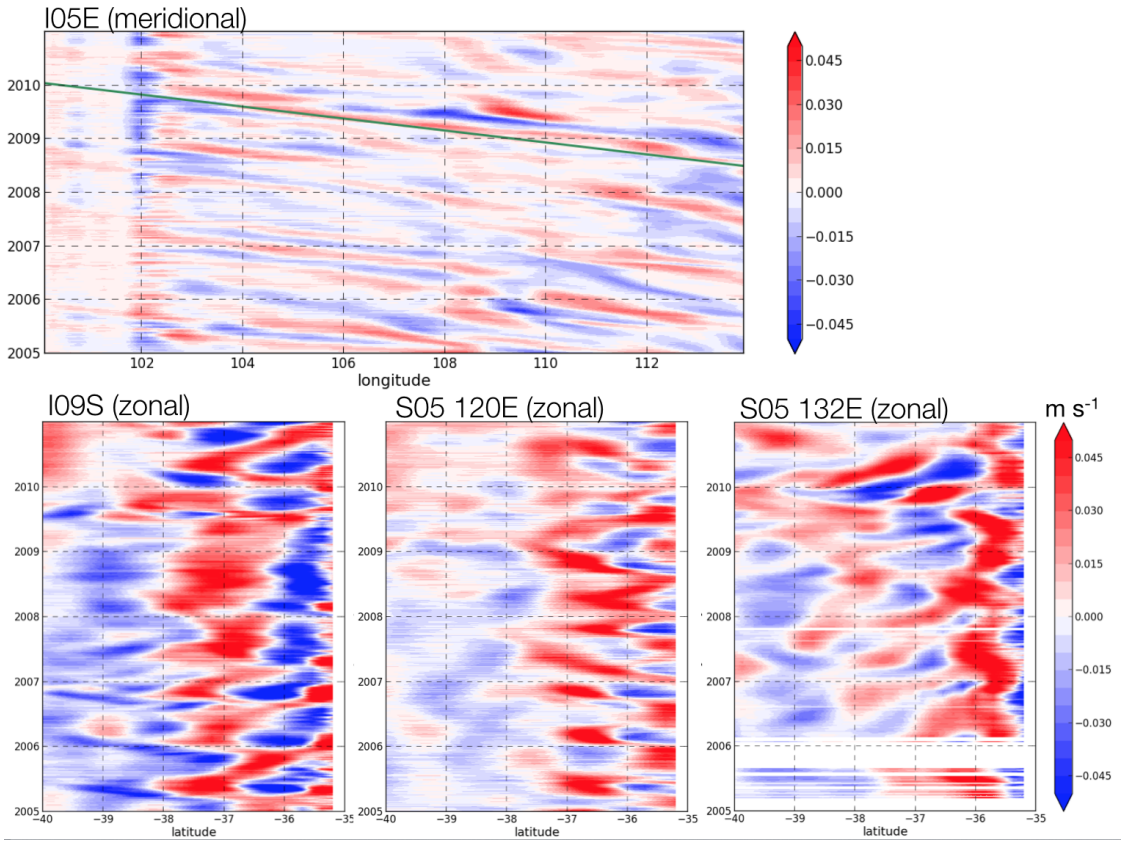

Figure 5.6: SOSE daily-mean a) meridional velocity averaged in the IDW layer as a function of longitude along the I05 section and zonal velocity averaged in the IDW layer as a function of latitude (with the Australian continent to the right) for b) I09S, c) S05 120E, and d) S05 132E. Positive values indicate northward flow in a) and eastward flow in b), c) and d). The teal line in a) shows a westward phase speed of 0.5 cm s^{-1}.

Chapter 6

Summary and Conclusions

This thesis investigated the three-dimensionality of multiple aspects of the Southern Ocean circulation using a data-assimilating ocean state estimate along with other eddying models and ocean observations. In particular, we characterized spatial variations in the upper ocean heat budget (Chapter 2), the three-dimensional upwelling pathways and water mass transformation along these pathways (Chapters 3,4 and 5) in the Southern Ocean. While this work has answered some important questions about the structure and dynamics of the Southern Ocean circulation, it has also generated many unanswered questions that can shape the direction of future research.

A common thread found in the results of each chapter is the key role of topography in setting the three-dimensional circulation, by causing both steering in the time-mean currents and hotspots of time-dependent eddies that are key for setting the structure of the Southern Ocean surface fluxes and circulation. The ability to look at this mesoscale component of the circulation in high resolution models has contributed greatly to the understanding of the importance of topographic features in driving hotspots of exchange and mixing (e.g. Dufour et al., 2015; Thompson and Sallee, 2012; Mashayek et al., 2017). However, there are significant limitations to the current class of ocean

models, and in this work we have relied on parameterizations for representing sub-grid scale turbulent processes. Future work should look to using models with more realistic representations of mixing and bottom boundary layer processes or modifying current models to include some of these processes to see how these processes impact upwelling pathways and associated water mass transformation.

Another novel finding is the result that deep water masses from the Indian, Atlantic and Pacific Oceans travel poleward toward the ACC predominantly at both western and eastern boundaries before upwelling to the surface of the Southern Ocean (Chapters 3 and 5). The importance of the eastern pathways has not been fully appreciated in the past, and as a result there are many aspects that are not well characterized. In several places these deep, poleward boundary pathways overlie known equatorward pathways of abyssal AABW (Van Sebille et al., 2013); thus it appears likely that there are important interactions between the two. Future research into the dynamics of these deep pathways and their interaction with both upper ocean boundary currents and abyssal circulation is warranted.

This thesis has focused on determining the structure and underlying mechanisms of the Southern Ocean circulation in its current state. However, we know that the Southern Ocean and the Antarctic continent are changing rapidly in response to anthropogenic climate change. The improved understanding of key processes in the overturning circulation found here can help form hypotheses of how the Southern ocean is responding to current and future changes in westerly winds, eddy kinetic energy, heat content, freshwater input etc. In future work, model experiments that test the sensitivity of the circulation to changes in forcing would help test these hypotheses. For example, experiments investigating how the upwelling transport at topographic hotspots is influenced by changes in wind and associated changes in eddy kinetic energy, or how water mass transformation during upwelling is influenced by changes in freshwater fluxes from Antarctic ice. Ad-

ditionally, upwelling deep waters in the Southern Ocean are a key driver of accelerating Antarctic ice shelf basal melt (Cook et al., 2016). Future work should characterize how three-dimensional upwelling pathways and different source water masses contribute to the source of offshore warm water that drives basal ice shelf melt. Finally, changes in the Southern Ocean overturning circulation have important implications for the oceanic uptake and storage of carbon and nutrients (Sarmiento et al., 2004; Frölicher et al., 2015). Thus, future work should focus on more directly tying the three-dimensional circulation, particularly upwelling pathways, to distributions and transports of carbon and nutrients between the deep ocean and the sea surface.

References

Abernathey, R. P., I. Cerovecki, P. R. Holland, E. Newsom, M. Mazloff, and L. D. Talley, 2016: Water-mass transformation by sea ice in the upper branch of the southern ocean overturning. *Nature Geoscience*, **9**, 596–601, doi:10.1038/ngeo2749.

Adcroft, A., C. Hill, and J. Marshall, 1997: Representation of topography by shaved cells in a height coordinate ocean model. *Monthly Weather Review*, **125**, 2293–2315.

Armour, K. C., J. Marshall, J. R. Scott, A. Donohoe, and E. R. Newsom, 2016: Southern Ocean warming delayed by circumpolar upwelling and equatorward transport. *in Preparation*, 1–7, doi:10.1038/ngeo2731.

Ballarotta, M., S. Drijfhout, T. Kuhlbrodt, and K. Döös, 2013: The residual circulation of the Southern Ocean: Which spatio-temporal scales are needed? *Ocean Modelling*, **64**, 46–55.

Bishop, S. P., P. R. Gent, F. O. Bryan, A. F. Thompson, M. C. Long, and R. Abernathey, 2016: Southern Ocean overturning compensation in an eddy-resolving climate simulation. *Journal of Physical Oceanography*, **46**, 1575–1592.

Blanke, B., M. Arhan, G. Madec, and S. Roche, 1999: Warm water paths in the equatorial Atlantic as diagnosed with a general circulation model. *Journal of Physical Oceanography*, **29**, 2753–2768.

Bourassa, M. A., S. T. Gille, C. Bitz, D. Carlson, I. Cerovecki, C. A. Clayson, M. F. Cronin, W. M. Drennan, C. W. Fairall, R. N. Hoffman, G. Magnusdottir, R. T. Pinker, I. A. Renfrew, M. Serreze, K. Speer, L. D. Talley, and G. A. Wick, 2013: High-Latitude Ocean and Sea Ice Surface Fluxes: Challenges for Climate Research. *Bulletin of the American Meteorological Society*, **94**, 403–423, doi:10.1175/BAMS-D-11-00244.1.

Brambilla, E., L. D. Talley, and P. E. Robbins, 2008: Subpolar Mode Water in the northeastern Atlantic: 2. Origin and transformation. *Journal of Geophysical Research: Oceans*, **113**.

Bryan, F. and S. Bachman, 2015: Isohaline salinity budget of the North Atlantic salinity maximum. *Journal of Physical Oceanography*, **45**, 724–736.

Bye, J. A., 1972: *Antarctic Oceanology I, The Australian-New Zealand Sector, Antarctic Res. Ser*, volume 19. AGU, Washington.

Cerovečki, I. and J. Marshall, 2008: Eddy modulation of air-sea interaction and convection. *J. Phys. Oceanogr.*, **38**, 65–93.

Cerovečki, I. and M. R. Mazloff, 2015: The spatiotemporal structure of diabatic processes governing the evolution of Subantarctic Mode Water in the Southern Ocean. *Journal of Physical Oceanography*, doi:10.1175/JPO-D-14-0243.1.

Cerovečki, I., M. R. Mazloff, and L. D. Talley, 2011: A Comparison of Southern Ocean Air-Sea Buoyancy Flux from an Ocean State Estimate with Five Other Products. *Journal of Climate*, **24**, 6283–6306, doi:10.1175/2011JCLI3858.1.

Cerovečki, I., L. D. Talley, M. R. Mazloff, and G. Maze, 2013: Subantarctic Mode Water Formation, Destruction, and Export in the Eddy-Permitting Southern Ocean State Estimate. *Journal of Physical Oceanography*, **43**, 1485–1511, doi:10.1175/JPO-D-12-0121.1.

Chelton, D. and R. Deszoeke, 1998: Geographical variability of the first baroclinic Rossby radius of deformation. *Journal of Physical Oceanography*, **28**, 433–460, doi:10.1175/1520-0485(1998)028<0433:GVOTFB>2.0.CO;2.

Chelton, D. B., M. G. Schlax, D. L. Witter, and J. G. Richman, 1990: Geosat Altimeter Observations of the Southern of the Surface Circulation. *Journal of Geophysical Research*, **95**, 17877–17903.

Cook, A., P. Holland, M. Meredith, T. Murray, A. Luckman, and D. Vaughan, 2016: Ocean forcing of glacier retreat in the western Antarctic Peninsula. *Science*, **353**, 283–286.

Cresswell, G. and D. Griffin, 2004: The Leeuwin Current, eddies and sub-Antarctic waters off south-western Australia. *Marine and Freshwater Research*, **55**, 267–276.

de Boyer Montégut, C., G. Madec, A. S. Fischer, A. Lazar, and D. Iudicone, 2004: Mixed layer depth over the global ocean: An examination of profile data and a profile-based climatology. *Journal of Geophysical Research: Oceans*, **109**, C12003.

Dee, D. P., S. M. Uppala, A. J. Simmons, P. Berrisford, P. Poli, S. Kobayashi, U. Andrae, M. A. Balmaseda, G. Balsamo, P. Bauer, P. Bechtold, A. C. M. Beljaars, L. van de Berg, J. Bidlot, N. Bormann, C. Delsol, R. Dragani, M. Fuentes, A. J. Geer, L. Haimberger, S. B. Healy, H. Hersbach, E. V. Hólm, L. Isaksen, P. Kå llberg, M. Köhler, M. Matricardi, A. P. Mcnally, B. M. Monge-Sanz, J. J. Morcrette, B. K. Park, C. Peubey, P. de Rosnay, C. Tavolato, J. N. Thépaut, and F. Vitart, 2011: The ERA-Interim reanalysis: Configuration and performance of the data assimilation system. *Quarterly Journal of the Royal Meteorological Society*, **137**, 553–597,

doi:10.1002/qj.828.

Dong, S., S. T. Gille, and J. Sprintall, 2007: An Assessment of the Southern Ocean Mixed Layer Heat Budget. *Journal of Climate*, **20**, 4425–4442, doi:10.1175/JCLI4259.1.

Dong, S. and K. a. Kelly, 2004: Heat Budget in the Gulf Stream Region: The Importance of Heat Storage and Advection. *Journal of Physical Oceanography*, **34**, 1214–1231, doi:10.1175/1520-0485(2004)034<1214:HBITGS>2.0.CO;2.

Döös, K., 1995: Interocean exchange of water masses. *Journal of Geophysical Research*, **100**, 13499, doi:10.1029/95JC00337.

Döös, K., J. Nilsson, J. Nycander, L. Brodeau, and M. Ballarotta, 2012: The world ocean thermohaline circulation. *Journal of Physical Oceanography*, **42**, 1445–1460.

Döös, K., J. Nycander, and A. C. Coward, 2008: Lagrangian decomposition of the Deacon Cell. *Journal of Geophysical Research: Oceans*, **113**, C07028, doi:10.1029/2007JC004351.

Downes, S. M., A. Gnanadesikan, S. M. Griffies, and J. L. Sarmiento, 2011: Water Mass Exchange in the Southern Ocean in Coupled Climate Models. *Journal of Physical Oceanography*, **41**, 1756–1771, doi:10.1175/2011JPO4586.1.

Drake, H., A. K. Morrison, S. M. Griffies, J. L. Sarmiento, W. Weijer, and A. R. Gray, 2018: Lagrangian Timescales of Southern Ocean upwelling in a hierarchy of model resolutions. *Geophys. Res. Lett.*, **45**, doi:https://doi.org/10.1002/2017GL076045.

Dufour, C. O., S. M. Griffies, G. F. de Souza, I. Frenger, A. K. Morrison, J. B. Palter, J. L. Sarmiento, E. D. Galbraith, J. P. Dunne, W. G. Anderson, and R. D. Slater, 2015: Role of mesoscale eddies in cross-frontal transport of heat and biogeochemical tracers in the Southern Ocean. *Journal of Physical Oceanography*, **45**, 3057–3081, doi:10.1175/JPO-D-14-0240.1.

Dufour, C. O., L. L. Sommer, J. D. Zika, M. Gehlen, J. C. Orr, P. Mathiot, and B. Barnier, 2012: Standing and transient eddies in the response of the Southern Ocean meridional overturning to the Southern annular mode. *Journal of Climate*, **25**, 6958–6974, doi:10.1175/JCLI-D-11-00309.1.

Faure, V., M. Arhan, S. Speich, and S. Gladyshev, 2011: Heat budget of the surface mixed layer south of Africa. *Ocean Dynamics*, **61**, 1441–1458, doi:10.1007/s10236-011-0444-1.

Faure, V. and K. Speer, 2012: Deep circulation in the eastern south pacific ocean. *Journal of Marine Research*, **70**, 748–778.

Fenty, I. and P. Heimbach, 2013: Coupled sea ice–ocean-state estimation in the labrador sea and baffin bay. *Journal of Physical Oceanography*, **43**, 884–904.

Ferrari, R., A. Mashayek, T. J. McDougall, M. Nikurashin, and J.-M. Campin, 2016: Turning ocean mixing upside down. *Journal of Physical Oceanography*, **46**, 2239–2261.

Forget, G., 2010: Mapping Ocean Observations in a Dynamical Framework: A 2004-06 Ocean Atlas. *Journal of Physical Oceanography*, **40**, 1201–1221, doi:10.1175/2009JPO4043.1.

Foster, T. D., 1972: An analysis of the cabbeling instability in sea water. *Journal of Physical Oceanography*, **2**, 294–301.

Frölicher, T. L., J. L. Sarmiento, D. J. Paynter, J. P. Dunne, J. P. Krasting, and M. Winton, 2015: Dominance of the Southern Ocean in Anthropogenic Carbon and Heat Uptake in CMIP5 Models. *Journal of Climate*, **28**, 862–886, doi:10.1175/JCLI-D-14-00117.1.

Ganachaud, A. and C. Wunsch, 2000: Improved estimates of global ocean circulation, heat transport and mixing from hydrographic data. *Nature*, **408**, 453.

Garzoli, S. L., S. Dong, R. Fine, C. S. Meinen, R. C. Perez, C. Schmid, E. Van Sebille, and Q. Yao, 2015: The fate of the Deep Western Boundary Current in the South Atlantic. *Deep-Sea Research Part I: Oceanographic Research Papers*, **103**, 125–136, doi:10.1016/j.dsr.2015.05.008.

Gille, S. and K. Kelly, 1996: Scales of spatial and temporal variability in the Southern Ocean. *Journal of geophysical research*, **101**, 8759–8773.

Griffies, S. M., M. Winton, W. G. Anderson, R. Benson, T. L. Delworth, C. O. Dufour, J. P. Dunne, P. Goddard, A. K. Morrison, A. Rosati, A. T. Wittenberg, J. Yin, and R. Zhang, 2015: Impacts on ocean heat from transient mesoscale eddies in a hierarchy of climate models. *Journal of Climate*, **28**, 952–977, doi:10.1175/JCLI-D-14-00353.1.

Groeskamp, S., R. P. Abernathey, and A. Klocker, 2016: Water mass transformation by cabbeling and thermobaricity. *Geophysical Research Letters*, **43**, doi:10.1002/2016GL070860.

Groeskamp, S., B. M. Sloyan, J. D. Zika, and T. J. McDougall, 2017: Mixing inferred from an ocean climatology and surface fluxes. *Journal of Physical Oceanography*, **47**, 667–687.

Groeskamp, S., J. D. Zika, B. M. Sloyan, T. J. McDougall, and P. C. McIntosh, 2014: A Thermohaline Inverse Method for Estimating Diathermohaline Circulation and

Mixing. *Journal of Physical Oceanography*, **44**, 2681–2697, doi:10.1175/JPO-D-14-0039.1.

Hallberg, R. and A. Gnanadesikan, 2006: The role of eddies in determining the structure and response of the wind-driven southern hemisphere overturning: Results from the Modeling Eddies in the Southern Ocean (MESO) project. *Journal of Physical Oceanography*, **36**, 2232–2252.

Hobbs, W. R. and M. N. Raphael, 2007: A representative time-series for the Southern Hemisphere zonal wave 1. *Geophysical Research Letters*, **34**, 1–6, doi:10.1029/2006GL028740.

— 2010: Characterizing the zonally asymmetric component of the SH circulation. *Climate Dynamics*, **35**, 859–873, doi:10.1007/s00382-009-0663-z.

Hogg, A. M., M. P. Meredith, D. P. Chambers, E. P. Abrahamsen, C. W. Hughes, and A. K. Morrison, 2015: Recent trends in the Southern Ocean eddy field. *Journal of Geophysical Research C: Oceans*, **120**, 257–267, doi:10.1002/2014JC010470.

Holte, J. and L. Talley, 2009: A new algorithm for finding mixed layer depths with applications to Argo data and subantarctic mode water formation. *Journal of Atmospheric and Oceanic Technology*, **26**, 1920–1939, doi:10.1175/2009JTECHO543.1.

Holzer, M. and F. W. Primeau, 2006: The diffusive ocean conveyor. *Geophysical research letters*, **33**.

Hufford, G. E., M. S. McCartney, and K. A. Donohue, 1997: Northern boundary currents and adjacent recirculations off southwestern Australia. *Geophysical Research Letters*, **24**, 2797–2800.

Ito, T., M. Woloszyn, and M. Mazloff, 2010: Anthropogenic carbon dioxide transport in the Southern Ocean driven by Ekman flow. *Nature*, **463**, 80–83, doi:10.1038/nature08687.

Iudicone, D., G. Madec, B. Blanke, and S. Speich, 2008a: The Role of Southern Ocean Surface Forcings and Mixing in the Global Conveyor. *Journal of Physical Oceanography*, **38**, 1377, doi:10.1175/2008JPO3519.1.

Iudicone, D., G. Madec, and T. J. McDougall, 2008b: Water-mass transformations in a neutral density framework and the key role of light penetration. *Journal of Physical Oceanography*, 1357–1376, doi:10.1175/2007JPO3464.1.

Iudicone, D., S. Speich, G. Madec, and B. Blanke, 2008c: The global conveyor belt from a Southern Ocean perspective. *Journal of Physical Oceanography*, **38**, 1401–1425, doi:10.1175/2007JPO3525.1.

Jackett, D. R. and T. J. Mcdougall, 1995: Minimal adjustment of hydrographic profiles to achieve static stability. *Journal of Atmospheric and Oceanic Technology*, **12**, 381–389.

Jerlov, N. G., 1968: *Optical Oceanography*. Elsevier, 199 pp.

Karsten, R. H. and J. Marshall, 2002: Constructing the Residual Circulation of the ACC from Observations. *Journal of Physical Oceanography*, **32**, 3315–3327, doi:10.1175/1520-0485(2002)032<3315:CTRCOT>2.0.CO;2.

Katsumata, K., B. Sloyan, and S. Masuda, 2013: Diapycnal and isopycnal transports in the Southern Ocean estimated by a box inverse model. *Journal of Physical Oceanography*, **43**, 2270–2287.

Key, R. M., A. Kozyr, C. L. Sabine, K. Lee, R. Wanninkhof, J. L. Bullister, R. A. Feely, F. J. Millero, C. Mordy, and T.-H. Peng, 2004: A global ocean carbon climatology: Results from Global Data Analysis Project (GLODAP). *Global Biogeochemical Cycles*, **18**.

Kinderman, A. and J. Monahan, 1977: Computer generation of random variables using the ratio of uniform deviates. *ACM Trans. Math. Softw.*, **3**, 257–260.

Klocker, A. and T. J. McDougall, 2010: Influence of the nonlinear equation of state on global estimates of dianeutral advection and diffusion. *Journal of Physical Oceanography*, **40**, 1690–1709.

Kunze, E., E. Firing, J. M. Hummon, T. K. Chereskin, and A. M. Thurnherr, 2006: Global abyssal mixing inferred from lowered adcp shear and ctd strain profiles. *Journal of Physical Oceanography*, **36**, 1553–1576.

Landschützer, P., N. Gruber, F. A. Haumann, C. Rödenbeck, D. C. E. Bakker, S. V. Heuven, M. Hoppema, N. Metzl, C. Sweeney, and T. Takahashi, 2015: The reinvigoration of the Southern Ocean carbon sink. *Science*, **349**, 1221–1224.

Large, W. G., J. C. McWilliams, and S. C. Doney, 1994: Oceanic vertical mixing: A review and a model with a nonlocal boundary layer parameterization. *Reviews of Geophysics*, **32**, 363–403.

Large, W. G. and S. G. Yeager, 2009: The global climatology of an interannually varying air-sea flux data set. *Climate Dynamics*, **33**, 341–364, doi:10.1007/s00382-008-0441-3.

Le Quéré, C., C. Rödenbeck, E. T. Buitenhuis, T. J. Conway, R. Langenfelds, A. Gomez, C. Labuschagne, M. Ramonet, T. Nakazawa, N. Metzl, et al., 2007: Saturation of the Southern Ocean CO_2 sink due to recent climate change. *Science*, **316**, 1735–1738.

Ledwell, J., E. Montgomery, and K. Polzin, 2000: Evidence for enhanced mixing over rough topography in the abyssal ocean. *Nature*, **74**, 13–16.

Lenn, Y.-D. and T. K. Chereskin, 2009: Observations of Ekman Currents in the Southern Ocean. *Journal of Physical Oceanography*, **39**, 768–779, doi:10.1175/2008JPO3943.1.

Lovenduski, N. S., N. Gruber, and S. C. Doney, 2008: Toward a mechanistic understanding of the decadal trends in the Southern Ocean carbon sink. *Global Biogeochemical Cycles*, **22**.

Lumpkin, R. and K. Speer, 2007: Global Ocean Meridional Overturning. *Journal of Physical Oceanography*, **37**, 2550–2562, doi:10.1175/JPO3130.1.

Mantyla, A. W. and J. L. Reid, 1995: On the origins of deep and bottom waters of the Indian Ocean. *Journal of Geophysical Research: Oceans*, **100**, 2417–2439.

Marshall, G., 2003: Trends in the Southern Annular Mode from Observations and Reanalyses. *Journal of Climate*, **16**, 4134–4143.

Marshall, J., A. Adcroft, C. Hill, L. Perelman, and C. Heisey, 1997: A finite-volume, incompressible Navier Stokes model for studies of the ocean on parallel computers. *Journal of Geophysical Research*, **102**, 5753–5766.

Marshall, J., D. Jamous, and J. Nilsson, 1999: Reconciling thermodynamic and dynamic methods of computation of water-mass transformation rates. *Deep Sea Research Part I: Oceanographic Research Papers*, **46**, 545–572.

Marshall, J. and T. Radko, 2003: Residual-Mean Solutions for the Antarctic Circumpolar Current and Its Associated Overturning Circulation. *Journal of Physical Oceanography*, **33**, 2341–2354, doi:10.1175/1520-0485(2003)033<2341:RSFTAC>2.0.CO;2.

Marshall, J. and K. Speer, 2012: Closure of the meridional overturning circulation through Southern Ocean upwelling. *Nature Geoscience*, **5**, 171–180, doi:10.1038/ngeo1391.

Mashayek, A., R. Ferrari, S. Merrifield, J. R. Ledwell, L. St Laurent, and A. N. Garabato, 2017: Topographic enhancement of vertical turbulent mixing in the southern ocean. *Nature Communications*, **8**, 14197, doi:10.1038/ncomms14197.

Mazloff, M. R., P. Heimbach, and C. Wunsch, 2010: An Eddy-Permitting Southern Ocean State Estimate. *Journal of Physical Oceanography*, **40**, 880–899, doi:10.1175/2009JPO4236.1.

McCartney, M. S. and K. A. Donohue, 2007: A deep cyclonic gyre in the Australian–Antarctic Basin. *Progress in Oceanography*, **75**, 675–750.

McDonagh, E. L., H. L. Bryden, B. A. King, and R. J. Sanders, 2008: The circulation of the Indian Ocean at 32 S. *Progress in Oceanography*, **79**, 20–36.

McDougall, T. J. and P. M. Barker, 2011: Getting started with TEOS-10 and the Gibbs Seawater (GSW) oceanographic toolbox. *SCOR/IAPSO WG*, **127**, 1–28.

McDougall, T. J. and D. R. Jackett, 2005: The material derivative of neutral density. *Journal of Marine Research*, **63**, 159–185.

Middleton, J. F. and J. a. T. Bye, 2007: A review of the shelf-slope circulation along Australia's southern shelves: Cape Leeuwin to Portland. *Progress in Oceanography*, **75**, 1–41, doi:10.1016/j.pocean.2007.07.001.

Middleton, J. F. and M. Cirano, 2002: A northern boundary current along Australia's southern shelves: The Flinders Current. *Journal of Geophysical Research: Oceans*, **107**.

Milliff, R. F., T. J. Hoar, H. van Loon, and M. Raphael, 1999: Quasi-stationary wave variability in NSCAT winds. *Journal of Geophysical Research*, **104**, 11425, doi:10.1029/1998JC900087.

Morrison, A. K., S. M. Griffies, M. Winton, W. G. Anderson, and J. L. Sarmiento, 2016: Mechanisms of Southern Ocean heat uptake and transport in a global eddying climate model. *Journal of Climate*, 160122143729005, doi:10.1175/JCLI-D-15-0579.1.

Morrison, A. K., A. M. Hogg, and M. L. Ward, 2011: Sensitivity of the Southern Ocean overturning circulation to surface buoyancy forcing. *Geophysical Research Letters*, **38**, 1–5, doi:10.1029/2011GL048031.

Morrison, A. K., O. A. Saenko, A. M. Hogg, and P. Spence, 2013: The role of vertical eddy flux in Southern Ocean heat uptake. *Geophysical Research Letters*, **40**, 5445–5450, doi:10.1002/2013GL057706.

Munk, W., 1966: Abyssal recipes. *Deep Sea Research and Oceanographic Abstracts*, **13**, 707–730.

Munk, W. and C. Wunsch, 1998: Abyssal recipes II: energetics of tidal and wind mixing. *Deep Sea Research Part I: Oceanographic Research Papers*, **45(12)**, 1977–2010.

Naveira Garabato, A. C., R. Ferrari, and K. L. Polzin, 2011: Eddy stirring in the Southern Ocean. *Journal of Geophysical Research*, **116**, C09019, doi:10.1029/2010JC006818.

Naveira Garabato, A. C., K. L. Polzin, R. Ferrari, J. D. Zika, and A. Forryan, 2016: A microscale view of mixing and overturning across the Antarctic Circumpolar Current. *Journal of Physical Oceanography*, **46**, 233–254.

Naveira Garabato, A. C., K. L. Polzin, B. A. King, K. J. Heywood, and M. Visbeck, 2004: Widespread intense turbulent mixing in the southern ocean. *Science*, **303**, 210–213.

Nihashi, S. and K. I. Ohshima, 2015: Circumpolar mapping of Antarctic coastal polynyas and landfast sea ice: Relationship and variability. *Journal of Climate*, **28**, 3650–3670, doi:10.1175/JCLI-D-14-00369.1.

Nikurashin, M. and R. Ferrari, 2013: Overturning circulation driven by breaking internal waves in the deep ocean. *Geophysical Research Letters*, **40**, 3133–3137.

Nikurashin, M. and G. Vallis, 2011: A theory of deep stratification and overturning circulation in the ocean. *Journal of Physical Oceanography*, **41**, 485–502.

Orsi, A. H. and T. Whitworth, 2005: *Hydrographic Atlas of the World Ocean Circulation Experiment (WOCE): Volume 1: Southern Ocean*. WOCE International Project Office.

Orsi, A. H., T. Whitworth, and W. D. Nowlin, 1995: On the meridional extent and fronts of the Antarctic Circumpolar Current. *Deep Sea Research Part I: Oceanographic Research Papers*, **42**, 641–673.

Paolo, F. S., H. A. Fricker, and L. Padman, 2015: Volume loss from Antarctic ice shelves is accelerating. *Science*, **348**, 327–332, doi:10.1126/science.aaa0940.

Paris, C. B., J. Helgers, E. van Sebille, and A. Srinivasan, 2013: Connectivity Modeling System: A probabilistic modeling tool for the multi-scale tracking of biotic and abiotic variability in the ocean. *Environmental Modelling and Software*, **42**, 47–54, doi:10.1016/j.envsoft.2012.12.006.

Patara, L., C. W. Böning, and A. Biastoch, 2016: Variability and trends in Southern Ocean eddy activity in 1/12° ocean model simulations. *Geophysical Research Letters*, **43**, 4517–4523.

Paulson, C. A. and J. J. Simpson, 1977: Irradiance Measurements in the Upper Ocean. *Journal of Physical Oceanography*, **7**, 952–956, doi:10.1175/1520-0485(1977)007<0952:IMITUO>2.0.CO;2.

Polzin, K. L., 1997: Spatial Variability of Turbulent Mixing in the Abyssal Ocean. *Science*, **276**, 93–96, doi:10.1126/science.276.5309.93.

Qin, X., E. van Sebille, and A. Sen Gupta, 2014: Quantification of errors induced by temporal resolution on Lagrangian particles in an eddy-resolving model. *Ocean Modelling*, **76**, 20–30, doi:10.1016/j.ocemod.2014.02.002.

Radko, T. and J. C. Marshall, 2006: The Antarctic Circumpolar Current in Three Di-

mensions. *Journal of Physical Oceanography*, **36**, 651–669, doi:10.1175/JPO2893.1.

Ramachandran, P. and G. Varoquaux, 2011: Mayavi: 3d visualization of scientific data. *Computing in Science & Engineering*, **13**, 40–51.

Reid, J. L., 1994: On the total geostrophic circulation of the North-Atlantic Ocean: Flow patterns, tracers, and transports. *Prog. Oceanogr.*, **33**, 1–92, doi:10.1016/0079-6611(89)90001-3.

— 1997: On the total geostrophic ciculation of the South Pacific Ocean: flow patterns, tracers and transports. *Prog. Oceanogr.*, **39**, 263–352, doi:10.1016/0079-6611(86)90036-4.

Rhein, M., D. Kieke, and R. Steinfeldt, 2015: Advection of North Atlantic Deep Water from the Labrador Sea to the southern hemisphere. *Journal of Geophysical Research: Oceans*, **120**, 2471–2487.

Ridgway, K. and J. Dunn, 2007: Observational evidence for a Southern Hemisphere oceanic supergyre. *Geophysical Research Letters*, **34**.

Rignot, E., S. Jacobs, J. Mouginot, and B. Scheuchl, 2013: Ice-Shelf Melting Around Antarctica. *Science*, **341**, 266–270, doi:10.1126/science.1235798.

Rintoul, S. R. and M. H. England, 2002: Ekman Transport Dominates Local Air-Sea Fluxes in Driving Variability of Subantarctic Mode Water. *Journal of Physical Oceanography*, **32**, 1308–1321.

Robbins, P. E. and J. M. Toole, 1997: The dissolved silica budget as a constraint on the meridional overturning circulation of the Indian Ocean. *Deep Sea Research Part I: Oceanographic Research Papers*, **44**, 879–906.

Rocha, C. B., T. K. Chereskin, S. T. Gille, and D. Menemenlis, 2015: Mesoscale to submesoscale wavenumber spectra in Drake Passage. *Journal of Physical Oceanography*, 1–17.

Roemmich, D. and J. Gilson, 2009: The 2004-2008 mean and annual cycle of temperature, salinity, and steric height in the global ocean from the Argo Program. *Progress in Oceanography*, **82**, 81–100, doi:10.1016/j.pocean.2009.03.004.

Roemmich, D., J. Gilson, J. Willis, P. Sutton, and K. Ridgway, 2005: Closing the time-varying mass and heat budgets for large ocean areas: The Tasman Box. *Journal of Climate*, **18**, 2330–2343, doi:10.1175/JCLI3409.1.

Ruan, X., A. F. Thompson, M. M. Flexas, and J. Sprintall, 2017: Contribution of topographically generated submesoscale turbulence to southern ocean overturning. *Nature Geoscience*, ngeo3053.

Sallée, J.-B., R. Morrow, and K. Speer, 2008: Eddy heat diffusion and Subantarctic Mode Water formation. *Geophysical Research Letters*, **35**, L05607, doi:10.1029/2007GL032827.

Sallée, J.-B., K. Speer, R. Morrow, and N. Wienders, 2006: Formation of subantarctic mode water in the southeastern Indian Ocean. *Ocean Dynamics*, **56**, 525–542, doi:10.1007/s10236-005-0054-x.

Sallée, J. B., K. G. Speer, and S. R. Rintoul, 2010: Zonally asymmetric response of the Southern Ocean mixed-layer depth to the Southern Annular Mode. *Nature Geoscience*, **3**, 273–279, doi:10.1038/ngeo812.

Sarmiento, J. L., N. Gruber, M. A. Brzezinski, and J. P. Dunne, 2004: High-latitude controls of thermocline nutrients and low latitude biological productivity. *Nature*, **427**, 56–60, doi:10.1038/nature10605.

Schodlok, M. P. and M. Tomczak, 1997: The circulation south of Australia derived from an inverse model. *Geophysical Research Letters*, **24**, 2781–2784.

Schodlok, M. P., M. Tomczak, and N. White, 1997: Deep sections through the South Australian Basin and across the Australian-Antarctic Discordance. *Geophysical Research Letters*, **24**, 2785–2788.

Sheen, K., A. N. Garabato, J. Brearley, M. Meredith, K. Polzin, D. Smeed, A. Forryan, B. King, J.-B. Sallée, L. S. Laurent, et al., 2014: Eddy-induced variability in Southern Ocean abyssal mixing on climatic timescales. *Nature Geoscience*, **7**, 577–582.

Sloyan, B. M., 2006: Antarctic bottom and lower circumpolar deep water circulation in the eastern Indian Ocean. *Journal of Geophysical Research: Oceans*, **111**.

Sloyan, B. M. and S. R. Rintoul, 2000: Estimates of area-averaged diapycnal fluxes from basin-scale budgets. *Journal of Physical Oceanography*, **30**, 2320–2341.

— 2001a: Circulation, renewal, and modification of Antarctic Mode and Intermediate Water. *Journal of Physical Oceanography*, **31**, 1005–1030.

— 2001b: The Southern Ocean limb of the global deep overturning circulation. *Journal of Physical Oceanography*, **31**, 143–173.

Small, R. J., J. Bacmeister, D. Bailey, A. Baker, S. Bishop, F. Bryan, J. Caron, J. Dennis, P. Gent, H.-m. Hsu, et al., 2014: A new synoptic scale resolving global climate simulation using the Community Earth System Model. *Journal of Advances in Modeling Earth Systems*, **6**, 1065–1094.

Smith, W. H. and D. T. Sandwell, 1997: Global sea floor topography from satellite altimetry and ship depth soundings. *Science*, **277**, 1956–1962.

Sokolov, S. and S. R. Rintoul, 2009: Circumpolar structure and distribution of the antarctic circumpolar current fronts: 2. Variability and relationship to sea surface height. *Journal of Geophysical Research: Oceans*, **114**, C11019, doi:10.1029/2008JC005248.

Speer, K., S. R. Rintoul, and B. Sloyan, 2000: The Diabatic Deacon Cell*. *Journal of Physical Oceanography*, **30**, 3212–3222, doi:10.1175/1520-0485(2000)030<3212:TDDC>2.0.CO;2.

Speich, S., B. Blanke, P. de Vries, K. Doos, S. Drijfhout, A. Ganachaud, and R. Marsh, 2002: Tasman leakage: a new route in the global ocean conveyor belt. *Geophysical Research Letters*, **29**, 1–4, doi:10.1029/2001GL014586.

Speich, S., B. Blanke, and G. Madec, 2001: Warm and cold water routes of an ogcm thermohaline conveyor belt. *Geophysical Research Letters*, **28**, 311–314.

St. Laurent, L., A. C. Naveira Garabato, J. R. Ledwell, A. M. Thurnherr, J. M. Toole, and A. J. Watson, 2012: Turbulence and diapycnal mixing in drake passage. *Journal of Physical Oceanography*, **42**, 2143–2152.

Stewart, K. D. and T. W. Haine, 2016: Thermobaricity in the transition zones between alpha and beta oceans. *Journal of Physical Oceanography*, **46**, 1805–1821.

Sun, C. and D. R. Watts, 2002: Heat flux carried by the Antarctic Circumpolar Current mean flow. *Journal of Geophysical Research*, **107**, 3119, doi:10.1029/2001JC001187.

Swart, N. C. and J. C. Fyfe, 2012: Observed and simulated changes in the Southern Hemisphere surface westerly wind-stress. *Geophysical Research Letters*, **39**, 6–11, doi:10.1029/2012GL052810.

Talley, L. D., 2008: Freshwater transport estimates and the global overturning circulation: Shallow, deep and throughflow components. *Progress in Oceanography*, **78**, 257–303, doi:10.1016/j.pocean.2008.05.001.

— 2013a: Closure of the global overturning circulation through the Indian, Pacific, and Southern Oceans: Schematics and transports. *Oceanography*, **26**, 80–97, doi:10.5670/oceanog.2011.65.

— 2013b: Hydrographic Atlas of the World Ocean Circulation Experiment (WOCE). Vol. 4: Indian Ocean (eds M. Sparrow, P. Chapman and J. Gould) . *International WOCE Project Office, Southampton, UK, ISBN 0904175588.*.

Talley, L. D. and M. O. Baringer, 1997: Preliminary results from WOCE hydrographic sections at 80 E and 32 S in the central Indian Ocean. *Geophysical Research Letters*, **24**, 2789–2792.

Tamsitt, V., R. P. Abernathey, M. R. Mazloff, J. Wang, and L. D. Talley, 2018: Transformation of deep water masses along Lagrangian upwelling pathways in the Southern Ocean. *Journal of Geophysical Research: Oceans*, **in press**.

Tamsitt, V., H. Drake, A. Morrison, L. D. Talley, C. Dufour, A. Gray, S. Griffies, M. Mazloff, J. Sarmiento, J. Wang, and W. Weijer, 2017: Spiraling up: pathways of global deep water from the deep ocean to the surface of the southern ocean. *Nature Communications*, **8**, 172.

Tamsitt, V., L. D. Talley, M. R. Mazloff, and I. Cerovečki, 2016: Zonal variations in the Southern Ocean heat budget. *Journal of Climate*, **29**, 6563–6579.

Thomas, M. D., A. M. Tréguier, B. Blanke, J. Deshayes, and A. Voldoire, 2015: A Lagrangian method to isolate the impacts of mixed layer subduction on the meridional overturning circulation in a numerical model. *Journal of Climate*, **28**, 7503–7517, doi:10.1175/JCLI-D-14-00631.1.

Thompson, A. F. and A. C. Naveira Garabato, 2014: Equilibration of the Antarctic Circumpolar Current by Standing Meanders. *Journal of Physical Oceanography*, **44**, 1811–1828, doi:10.1175/JPO-D-13-0163.1.

Thompson, A. F. and J.-B. Sallee, 2012: Jets and topography: jet transitions and the impact on transport in the Antarctic Circumpolar Current. *Journal of Physical Oceanography*, **42**, 956–973, doi:10.1175/JPO-D-11-0135.1.

Thompson, A. F., A. L. Stewart, and T. Bischoff, 2016: A multibasin residual-mean model for the global overturning circulation. *Journal of Physical Oceanography*, **46**, 2583–2604.

Toggweiler, J. and B. Samuels, 1998: On the ocean's large-scale circulation near the limit of no vertical mixing. *Journal of Physical Oceanography*, 1832–1852.

Toggweiler, J. R. and B. Samuels, 1995: Effect of Drake Passage on the global thermohaline circulation. *Deep-Sea Research Part I*, **42**, 477–500, doi:10.1016/0967-0637(95)00012-U.

Toole, J. M. and B. A. Warren, 1993: A hydrographic section across the subtropical South Indian Ocean. *Deep Sea Research Part I: Oceanographic Research Papers*, **40**, 1973–2019.

van Loon, H. and R. L. Jenne, 1972: The zonal harmonic standing waves in the southern hemisphere. *Journal of Geophysical Research*, **77**, 992, doi:10.1029/JC077i006p00992.

Van Sebille, E., W. E. Johns, and L. M. Beal, 2012: Does the vorticity flux from Agulhas rings control the zonal pathway of NADW across the South Atlantic? *Journal of*

Geophysical Research: Oceans, **117**.

Van Sebille, E., P. Spence, M. R. Mazloff, M. H. England, S. R. Rintoul, and O. a. Saenko, 2013: Abyssal connections of Antarctic Bottom Water in a Southern Ocean State Estimate. *Geophysical Research Letters*, **40**, 2177–2182, doi:10.1002/grl.50483.

Van Sebille, E., J. Sprintall, F. U. Schwarzkopf, A. Sen Gupta, A. Santoso, M. H. England, A. Biastoch, and C. W. Böning, 2014: Pacific-to-Indian Ocean connectivity: Tasman leakage, Indonesian Throughflow, and the role of ENSO. *Journal of Geophysical Research: Oceans*, **119**, 1365–1382.

Viglione, G. A. and A. F. Thompson, 2016: Lagrangian pathways of upwelling in the Southern Ocean. *Journal of Geophysical Research: Oceans*, **121**, 6295–6309.

Vivier, F., D. Iudicone, F. Busdraghi, and Y.-H. Park, 2009: Dynamics of sea-surface temperature anomalies in the Southern Ocean diagnosed from a 2D mixed-layer model. *Climate Dynamics*, **34**, 153–184, doi:10.1007/s00382-009-0724-3.

Vivier, F., K. A. Kelly, and L. A. Thompson, 2002: Heat Budget in the Kuroshio Extension Region: 1993âĂŞ99. *Journal of Physical Oceanography*, **32**, 3436–3454, doi:10.1175/1520-0485(2002)032<3436:HBITKE>2.0.CO;2.

Wå hlin, A. K., X. Yuan, G. Björk, and C. Nohr, 2010: Inflow of Warm Circumpolar Deep Water in the Central Amundsen Shelf*. *Journal of Physical Oceanography*, **40**, 1427–1434, doi:10.1175/2010JPO4431.1.

WAIS Divide Project Members, 2015: Precise interpolar phasing of abrupt climate change during the last ice age. *Nature*, **520**, 661–665.

Walin, G., 1982: On the relation between sea-surface heat flow and thermal circulation in the ocean. *Tellus*, **34**, 187–195.

Wang, J., M. R. Mazloff, and S. T. Gille, 2014: Pathways of the Agulhas waters poleward of 29S. *Journal of Geophysical Research : Oceans*, **119**, 4234–4250, doi:10.1002/jgrc.20224.

Waterhouse, A. F., J. A. MacKinnon, J. D. Nash, M. H. Alford, E. Kunze, H. L. Simmons, K. L. Polzin, L. C. St. Laurent, O. M. Sun, R. Pinkel, et al., 2014: Global patterns of diapycnal mixing from measurements of the turbulent dissipation rate. *Journal of Physical Oceanography*, **44**, 1854–1872.

Watson, A. J., J. R. Ledwell, M.-J. Messias, B. a. King, N. Mackay, M. P. Meredith, B. Mills, and A. C. Naveira Garabato, 2013: Rapid cross-density ocean mixing at mid-depths in the Drake Passage measured by tracer release. *Nature*, **501**, 408–11, doi:10.1038/nature12432.

Whalen, C. B., L. D. Talley, and J. A. MacKinnon, 2012: Spatial and temporal variability of global ocean mixing inferred from Argo profiles. *Geophysical Research Letters*, **39**, n/a–n/a, doi:10.1029/2012GL053196.

Witter, D. L. and D. B. Chelton, 1998: Eddy-mean flow interaction in zonal oceanic jet flow along zonal ridge topography. *J. Phys. Oceanogr.*, **28**, 2019–2039.

Wolfe, C. L. and P. Cessi, 2011: The adiabatic pole-to-pole overturning circulation. *Journal of Physical Oceanography*, **41**, 1795–1810.

Wolfe, C. L., P. Cessi, J. L. McClean, and M. E. Maltrud, 2008: Vertical heat transport in eddying ocean models. *Geophysical Research Letters*, **35**, 1–5, doi:10.1029/2008GL036138.

Wunsch, C. and P. Heimbach, 2013: Dynamically and kinematically consistent global ocean circulation and ice state estimates. *International Geophysics*, **103**, 553–579, doi:10.1016/B978-0-12-391851-2.00021-0.

Young, W. R., 2012: An exact thickness-weighted average formulation of the Boussinesq equations. *J. Phys. Oceanogr.*, **42**, 692–707.

Yu, L. and R. A. Weller, 2007: Objectively analyzed air-sea heat fluxes for the global ice- free oceans (1981-2005). *Bulletin of the American Meteorological Society*, **88**, 527–539, doi:10.1175/BAMS-88-4-527.

Zika, J. D., M. H. England, and W. P. Sijp, 2012: The ocean circulation in thermohaline coordinates. *Journal of Physical Oceanography*, **42**, 708–724.

Zika, J. D., T. J. McDougall, and B. M. Sloyan, 2010: A tracer-contour inverse method for estimating ocean circulation and mixing. *Journal of Physical Oceanography*, **40**, 26–47.